Dissertation submitted to the

Combined Faculties for the Natural Sciences and Mathematics
of the Ruperto-Carola University of Heidelberg, Germany

for the degree of

Doctor of Natural Sciences

presented by

Olivia Tsang, MSci Physics
born in Hong Kong

Oral examination: 25 July 2007

Multi-frequency Synchrotron Self-Compton Models

for the Brightness Temperature Problem

in Compact Extra-galactic Radio Sources

Abstract

Flux variations in quasars and BL Lac objects over a time scale of a day or less suggest an extremely high brightness temperature in these sources, which cannot be explained by conventional synchrotron theory. This work addresses the issue of extreme brightness temperature by applying synchrotron theory to unconventional electron distributions.

We consider a scenario in which relativistic electrons are continuously injected into the emission region. In the first approximation, we assume the electrons are monoenergetic for simplicity. This approximation is insufficient when modelling the spectrum of S5 0716+714, we therefore modified the electron injection spectrum to one which is a double power law in energy. This retains the low radio frequency spectral characteristics of monoenergetic electrons, which extends to higher frequencies as a power law. To complete the study of the intrinsic properties of synchrotron emission from monoenergetic electrons, we also examine their circular polarisation.

We find that (1) electron distribution with low energy cut-off is able to generate high brightness temperature, and (2) the flat synchrotron spectrum produced by such distribution is in good agreement with that of the observed, and (3) in contrast to a power-law distribution, circular polarisation of synchrotron emission from monoenergetic electrons does not change sign.

Zusammenfassung

Die Beobachtung von Helligkeitsveränderungen in Quasaren und BL Lac Objekten auf einer Zeitskala von Tagen oder weniger, legt eine extrem hohe Helligkeitstemperatur in diesen Quellen nahe, die sich nicht ohne weiteres aus den bisherigen Standard-Synchrotrontheorie-Ansätzenerklären lässt. Diese Arbeit untersucht daher das Problem extremer Helligkeitstemperaturen im Zusammenhang der Synchrotrontheorie für unkonventionelle Elektronverteilungen.

Wir betrachten dazu ein Modell, bei dem relativistische Elektronen kontinuierlich in das Emissionsgebiet injiziert werden. In einer ersten Näherung nehmen wir der Einfachheit halber an, dass die Elektronen mononenergetisch sind. Diese Näherung reicht allerdings noch nicht aus, um z.B. das Spektrum des BL Lac Objektes S5 0716+714 zu modellieren. Wir führen daher eine modifizierte Elektronverteilung ein, welche einem doppeltem Potenzgesetz in der Energie folgt. Diese ist so gewählt, dass sie die Niederfrequenz-Radio-Spektralcharakteristik monoenegetischer Elektronen erhält und zu höheren Frequenzen hin einem Potenzgesetz folgt. Zur vollständigen Analyse der intrinsischen Synchrotronemission monoenergetischer Elektronen untersuchen wir außerdem die zirkularen Polarisationseigenschaften.

Unsere Arbeit zeigt, dass entprechende Elektronverteilungen mit einer Niederenergie-Grenze durchaus in der Lage sind, (1) das Problem der hohen Helligkeitstemperaturen zu lösen und (2) den beobachteten, flachen Spektralverlauf erfolgreich zu erklären, und dass (3) die zirkulare Polarisation der Synchrotronstrahlung monoenegetischer Elektronen, im Gegensatz zu Potenzgesetz-Verteilungen, das Vorzeichen nicht wechselt.

To *Nick, my parents and Wicket*

Acknowledgements

I would like to take this opportunity to thank...

...*John Kirk*, my PhD advisor, for his patient guidance and for never complaining about the number of drafts I have asked him to read.

...*Stefan Wagner* for agreeing to be the second reader of my thesis and suggestions given to my work.

...*Klaus Meisenheimer* and *Werner Hoffman* for agreeing to be the examiners of my viva voce.

...*Nick*, my husband, for his support and entertainment over the years.

...*My parents* for telling me not to be so lazy for the past twenty years.

...*My parents in law* for their support.

...*Andrea Ma* and *Mario Kallis* for their distractions, a sign of true friendship.

...*Richard Tuffs* for proof reading parts of my thesis.

...*Frank Rieger* for "help" with the German abstract.

...*Jerome Petri* for help with Mathematica.

...*Dimitrios Emmanoulopoulos* for being another PhD-student-who-cannot-speak-German-very-well.

...*Luisa Ostorero* for information and advices.

...*Dmitry Khangulyan* for telling me that thesis is not so important.

...*Andrew Taylor* for agreeing to proof read my introduction but never got back to me.

...*The Astrophysics group* at the MPIK for frequently asking when I will finish my PhD.

...*Wicket the cat* for being a constant amusement.

and finally all the people that I should thank but have not been included here due to space restriction. THANK YOU!

Contents

Chapter

Appendix

Figures

Figure

Tables

Table

Chapter 1

Introduction

Variations in flux density of active galactic nuclei (AGN) are frequently observed at frequencies ranging from the radio band to gamma-ray energies. Studies of variability are important since the time scale constrains the size of the emission region in which radiation of a particular frequency band is produced. Causality arguments constrain the size of a source of emission varying over a time scale of Δt_{obs} to $R < R_{\mathrm{var}} = c\Delta t_{\mathrm{obs}}$. If the size of the emission region is bigger than R_{var}, the different parts of the source cannot be in causal contact, and therefore will not be varying in phase with each other. The size constraint as well as the light curve − the temporal profile of the flux variation − of the source are important factors in identifying the radiation mechanisms within the source, and how this radiation propagates from the source to ultimately be observed at Earth.

1.1   Historical overview

At radio frequencies, the time scales of the variations range from weeks to years. In general, shorter variations, from weeks to months, are observed at higher frequencies from $40 - 100$ GHz, whereas longer variations, from months to years, are observed at lower frequencies from $1 - 10$ GHz [Bre90]. Hoyle et al (1966) [HBS66] showed that the photon energy density in a radio source that varies over a time scale of months is much higher than the magnetic field energy density. This implies that the photon energy density of the Compton-scattered synchrotron photons, scattered by the energetic electrons that emitted them, must be higher than the photon energy density of the synchrotron photons, and that each successive scattering will produce photons

with an energy density that exceeds the previous generation. Rees (1966) [Ree66] suggested that relativistic bulk motion of the source in the direction of the observer close to the line of sight may be responsible for the apparently high flux variations at radio frequencies. He proposed that the bulk relativistic motion of the source would boost the observed flux roughly by the bulk Lorentz factor of the source, and he applied this scenario to explain the observed variability of 3C 273. Doppler boosting as a result of a fast moving source therefore appears to alleviate the problem of diverging energy densities in the scattered photons.

The brightness (or specific intensity, I_ν) of a source at a certain frequency ν is commonly characterised by the temperature of a blackbody that has the same brightness at that frequency, the *brightness temperature*, T_B, of the source [e.g. RL79].

$$T_B = \frac{c^2}{2k_B \nu^2} I_\nu = \frac{c^2}{2k_B \nu^2} \frac{F_\nu}{\theta_D^2} \tag{1.1}$$

where k_B is the Boltzman constant, F_ν is the specific flux density and θ_D is the angular diameter of the source. Kellermann and Pauliny-Toth (1969) [KP69] formulated the condition to avoid diverging photon energy densities into a limiting brightness temperature of $T_B < 10^{12}$ K. This limit will be discussed in more detail in the next chapter.

Rapid variations over the time scale of days or less, referred to as *intraday variability* (IDV), was first observed at optical frequencies in 1967 in 3C 279 [Oke67] and in the radio band in 1971 in OJ 287 [see e.g. EFK+72, WW95, and references given therein] in sources classified as BL Lac objects, optically violently variable (OVV) quasars or highly polarised quasars (HPQ). Due to the many similarities amongst these objects − (1) smooth continuum emission from the infrared to ultraviolet band; (2) high optical polarisation ($\gtrsim 3\%$); (3) rapid optical variability on a time scale of 1 day; (4) a strong and variable radio continuum − they are collectively known as *blazars*, following the suggestion by Spiegel (1978) at the Pittsburgh Conference on BL Lac objects. Since then, strong radio fluxes together with rapid flux variations at GHz frequencies have been observed in many flat spectrum radio sources [e.g. KJW+01, LJB+03, have observed 22 and 85 IDV sources, respectively].

The problems associated with the observations of IDV quickly became apparent on the realisation that the brightness temperatures inferred from variability are much

higher than 10^{12} K. For a source at redshift z, the size of the emission region is constrained by $R < c\Delta t_{\mathrm{obs}}/(1+z)$ (and the angular diameter is constrained by $\theta_{\mathrm{D}} = R/D$, D being the distance from the source to the observer). Using the IDV time scale as the upper limit of the linear size of the source, the brightness temperature of the source is

$$T_{\mathrm{B}} \geq T_{\mathrm{var}} = 4.63 \times 10^{13} \left(\frac{F_{\nu,\mathrm{Jy}}}{\nu_{\mathrm{GHz}}^2} \right) \left(\frac{D_{\mathrm{Mpc}}}{(1+z)\Delta t_{\mathrm{obs,day}}} \right)^2 \mathrm{K} \qquad (1.2)$$

where $\Delta t_{\mathrm{obs,day}} = \Delta t_{\mathrm{obs}}/(1day)$, $F_{\nu,\mathrm{Jy}}$ is the specific flux density, ν_{GHz} is the observing frequency and D_{Mpc} is the distance from the source, in unit of Jansky, GHz and Mpc, respectively. Such high brightness temperatures contradict with the scenario in which an avalanche in photon energy density is created as the synchrotron photons are repeatedly scattered to higher energy, resulting in the reduction of brightness temperature due to the rapid energy loss experienced by the scattering electrons. The high level of X-ray emissions which would result from inverse Compton scattering of synchrotron photons have not been observed in compact radio sources [FMC$^+$98, SCU00, TMG$^+$02, PCG$^+$04, GSS$^+$06], indicating the non-existence of such divergence in photon energy density.

This work addresses the high brightness temperatures inferred from observations of IDV in the radio continuum. The power-law continuum spectra in the radio to infrared/optical domain together with the high degree of polarisation at radio frequency, leads to the conclusion that the rapidly varying radio emission has a synchrotron origin. Continuum emission at X- to γ-ray energies can be produced by inverse Compton scattering of the synchrotron photons by the synchrotron-emitting electrons, a process termed *synchrotron self-Compton* (SSC) emission [see e.g. Gou79]. Therefore, in order to understand the nature of compact radio sources, it is necessary to study the radiation mechanisms inside the source, and how this radiation is transported from within the source to the surface. In the following sections, we discuss briefly the concepts behind synchrotron radiation and synchrotron self-Compton scattering and summarise important results which will be used in later chapters.

1.2   Synchrotron radiation

Synchrotron radiation is emitted by relativistic electrons gyrating in a magnetic field. It is classed as a "non-thermal" radiation process since synchrotron spectra do not resemble those of black-body radiation or thermal bremsstrahlung. The power emitted by the relativistic electrons in the form of synchrotron radiation is

$$\frac{\mathrm{d}E}{\mathrm{d}t} = \frac{4}{3}\sigma_{\mathrm{T}}c\gamma^2 U_B \tag{1.3}$$

where σ_{T} is the Thomson scattering cross-section, γ is the electron Lorentz factor and $U_B = B^2/(8\pi)$ is the energy density of the magnetic field. Synchrotron emission is widely accepted as the mechanism responsible for the radio emission from radio galaxies and radio quasars and up to optical frequencies in some radio galaxies [CCC02]. It is also proposed that X$-$ray continuum emission of blazar is of synchrotron origin ([Kra04] gives a review on observations and theoretical interpretations for TeV blazars). In depth discussion on the synchrotron formulae summarised below can be found, for example, in [Lon92] and [RL79].

A relativistic electron with Lorentz factor $\gamma \gg 1$ in a magnetic field, $\mathbf{B}$, moves in a helix with its axis parallel to the direction of $\mathbf{B}$, with a gyration frequency $\nu_{\mathrm{g}} = eB/(2\pi\gamma mc) = \nu_{\mathrm{L}}/\gamma$, where ν_{L} is the Larmor frequency. The emissivity for a single electron, at frequency ν, is,

$$j_\nu = \frac{\sqrt{3}}{4\pi}\alpha_{\mathrm{f}}\, h\nu_{\mathrm{L}}\, \sin\theta\, F(x) \tag{1.4}$$

where θ is the angle between the magnetic field and the direction of the emitted radiation, α_{f} is the fine structure constant, $x = \nu/\nu_{\mathrm{s}}$ and ν_{s} is the characteristic frequency of synchrotron radiation from an electron of Lorentz factor γ, defined as

$$\begin{aligned} \nu_{\mathrm{s}} &= \frac{3\nu_{\mathrm{L}}\sin\theta\gamma^2}{2} \\ &= \nu_0\gamma^2 \end{aligned} \tag{1.5}$$

and the function

$$F(x) = x\int_x^\infty \mathrm{d}z K_{5/3}(z) \tag{1.6}$$

where $K_{5/3}(z)$ is the modified Bessel function of order 5/3.

For a distribution of electrons with energy between $\gamma_1 mc^2$ and $\gamma_2 mc^2$, the number density of electrons in the interval γ to $\gamma + d\gamma$ is $n_e(\gamma)d\gamma$. The synchrotron emissivity per unit volume is then,

$$J_\nu = \int_{\gamma_1}^{\gamma_2} j_\nu n_e(\gamma) d\gamma \tag{1.7}$$

The electron spectrum in phase space is often assumed to be the power law distribution, since observed radio spectra from optically thin emission often show a featureless continuum $I_\nu \propto \nu^{-\alpha}$, and these are naturally produced by an electron spectrum of the form $n_e(\gamma)d\gamma \propto \gamma^{-(2\alpha+1)}d\gamma$. For an electron distribution $n_e(\gamma)d\gamma = n_0\gamma^{-s}d\gamma$, Eq. (1.7) becomes,

$$J_\nu = a(s)\,\alpha_f\,n_0\,h\nu_L \sin\theta \left(\frac{\nu}{\nu_L \sin\theta}\right)^{-\frac{(s-1)}{2}} \tag{1.8}$$

$$a(s) = \frac{3^{s/2}}{4\pi(s+1)}\Gamma\left(\frac{3s+19}{12}\right)\Gamma\left(\frac{3s-1}{12}\right) \tag{1.9}$$

Synchrotron photons are emitted by relativistic particles. In the rest frame of the particle, emission is isotropic, but in the rest frame of the observer, emission is concentrated in the forward direction within a small angle of $(1/\gamma)$. The radiation is said to be *relativistically beamed*. This implies that the observed radiation is amplified, and can only be observed when the line of sight falls within this small angle of $(1/\gamma)$ of the trajectory of an electron.

Synchrotron emission is expected to have a high degree of linear polarisation (LP) if the magnetic field is uniform. As the relativistic particle spirals around the magnetic field line, the circular polarisation of its synchrotron emission on either side of the field line has opposite sign and approximately equal in magnitude, so that the left and right handed circular polarisation almost cancel each other out. If the magnetic field direction is random, it does not favour any direction in which the electrons travel. Therefore, the net polarisation over the region vanishes. In a uniform magnetic field, synchrotron emission from the electron distribution $n_e(\gamma) \propto \gamma^{-s}$, the degree of LP is

$$r_L = \frac{s+1}{s+\frac{7}{3}} \tag{1.10}$$

For a typical value of the electron power-law index of $s = 2.5$, LP can be as high as 72%.

The degree of circular polarisation (CP) from synchrotron emission is expected to be negligible, as explained above, since the two modes of circular polarisation are almost cancelled out if the electron distribution is isotropic and they are embedded in an uniform magnetic field. In reality, there is a small fraction of CP of emission proportional to γ^{-1} from each relativistic electron that is not cancelled, and the angular distribution of the electrons may not be completely isotropic. Therefore, there is always a small degree of CP, and to order of magnitude, it is approximately

$$r_C \sim mc^2/(k_B T_B) \tag{1.11}$$

(detail calculations can be found in e.g. [LW68] and [Mel80]). For a source with a brightness temperature of 10^{12} K, $r_C \sim 0.6\%$.

The synchrotron emission in the form of Eq. (1.8) will only be observed if there is no absorption by the source of emission, or any intervening matter. This work consider only intrinsic properties of the source, therefore, only synchrotron self-absorption. The absorption coefficient of the synchrotron-emitting electrons for unpolarised radiation is

$$
\begin{aligned}
\alpha_\nu &= -\frac{c^2}{8\pi\nu^2} \int_0^\infty j_\nu E^2 \frac{\mathrm{d}}{\mathrm{d}E}\left(\frac{n_e(E)}{E^2}\right)\mathrm{d}E \\
&= -\frac{c^2}{8\pi\nu^2} \int_0^\infty \frac{j_\nu}{mc^2}\gamma^2 \frac{\mathrm{d}}{\mathrm{d}\gamma}\left(\frac{n_e(\gamma)}{\gamma^2}\right)\mathrm{d}\gamma
\end{aligned} \tag{1.12}
$$

For the same power-law electron distribution used in Eq. (1.8) in which electrons emit according to Eq. (1.4), the absorption coefficient is

$$\alpha_\nu = b(s)\frac{\sigma_T}{\alpha_f}\frac{n_0 mc^2}{h\nu_L \sin\theta}\left(\frac{\nu}{\nu_L \sin\theta}\right)^{-\frac{(s+4)}{2}} \tag{1.13}$$

$$b(s) = \frac{3^{(s+3)/2}}{64\pi(s+2)^2}\Gamma\left(\frac{3s+22}{12}\right)\Gamma\left(\frac{3s+2}{12}\right) \tag{1.14}$$

The final synchrotron spectrum, I_ν, which we observe as a result of spontaneous emission and self-absorption is found by solving the transfer equation for unpolarised radiation,

$$\frac{\mathrm{d}I_\nu}{\mathrm{d}z} = -\alpha_\nu I_\nu + J_\nu \tag{1.15}$$

where z is the distance along the ray path within the source. The solution to Eq. (1.15), for J_ν and α_ν independent of z, is

$$I_\nu = \frac{J_\nu}{\alpha_\nu}\left(1 - e^{-\alpha_\nu R}\right) \tag{1.16}$$

The term J_ν/α_ν is often referred to as the *source function*, S_ν, and $\alpha_\nu R$ is the synchrotron optical depth τ_s, where R is the linear size of the source. The source is *optically thin* if $\tau_\mathrm{s} < 1$ and is *optically thick* if $\tau_\mathrm{s} > 1$. In the optically thin limit for $\tau_\mathrm{s} \ll 1$, $I_\nu \propto J_\nu \propto \nu^{-(s-1)/2}$, whereas in the optically thick limit for $\tau_\mathrm{s} \gg 1$, $I_\nu \propto S_\nu \propto \nu^{5/2}$.

1.2.1 Synchrotron self-Compton emission

In a compact synchrotron source, synchrotron photons can be scattered by the synchrotron-emitting electrons that produce them in the first place, and in doing so, the energy of the photons is increased by a factor of $\sim \gamma^2$, where γ is the Lorentz factor of the electrons. These self-scattered photons can then be scattered again to even higher energies. The scattering continue until the photon energy in the rest frame of the electron exceeds the rest mass energy of the electron, whereupon Klein-Nishina effects reduce the scattering cross-section between the photon and the electron such that further scattering is very limited.

The power of inverse Compton scattering is proportional to the energy density of the radiation field U_rad,

$$\frac{\mathrm{d}E}{\mathrm{d}t} = \frac{4}{3}\sigma_\mathrm{T} c \gamma^2 U_\mathrm{rad} \tag{1.17}$$

In the case of synchrotron self-Compton scattering, the power of the first generation scattering is proportional to the synchrotron photon density. The ratio of the luminosity of the synchrotron photons to the consecutive self-scattered photons can be characterised by a dimensionless Comptonisation parameter, proportional to the square of the energy of the electrons (this will be explained in more details in later chapters). If this ratio exceeds unity, the luminosity of the first generation of scattered photons becomes higher than that of the synchrotron, the luminosity of the second generation of scattered photons exceeds that of the first, and so on. In this case, the electrons lose their energy very rapidly to the photons, therefore suppressing synchrotron emission.

1.3 Aim of this work

We have seen a brief history of the studies of variability in AGN in this chapter, and the contradictions between observations and theories. Clearly, the current picture

of the theory behind IDV is still incomplete. The following two chapters are dedicated
to the discussion of the limits on the brightness temperature of a synchrotron source,
and the theoretical work that has developed so far.

In Chapter 2, we discuss the processes that can take place within the source
as the energy density of the synchrotron photons increases. These processes act to
limit the brightness temperature of the synchrotron source. We focus our discussion
on the *Compton catastrophe*, which gives the famous upper limit of 10^{12} K. When
the synchrotron photon energy density reaches the Compton catastrophe threshold, it
triggers a series of inverse Compton scattering between the energetic electrons and the
soft synchrotron photons and thus the electrons are rapidly cooled. The equipartition
of the magnetic field and particle energy density may also put a limit on the source
brightness temperature. The minimum energy content required by a synchrotron source
of a certain luminosity is approximately equal to the equipartition energy. Therefore,
this is an assumption that is incorporated in many synchrotron based models, and
is responsible for a slightly lower upper limit of 10^{11} K. Induced Compton scattering
between a low energy electron and a high energy synchrotron photon results in the
photon losing part of its energy to the electron. This process becomes significant as
the brightness temperature exceeds $\sim 5 \times 10^{9}$ K when low energy electrons are present,
causing a decrease in photon energy and therefore reduces the brightness temperature.

Despite all the limits arise from the various processes, as we have outlined above
and in more details in the next chapter, many flat spectrum radio sources have displayed
IDV. According to Eq. (1.2), the brightness temperature of these IDV sources would be
much higher, often by many orders of magnitude, than any of the limits listed. Extrinsic
mechanisms may account for the short time scale of flux variations in some sources but
not all. Interstellar scintillation can reproduce the rapid "flickering" in some sources.
This mechanism is frequency dependent, and can account for variations in the radio
band. However, interstellar scintillation cannot explain the large amplitudes of some
of the observed flux variations. Gravitational microlensing predicts a flux amplifica-
tion, but it is achromatic, therefore cannot explain the frequency dependent variations.
Intrinsic explanations of IDV and the associated high brightness temperature must,
therefore, be explored. Many theories have been developed surrounding the theme of

producing and sustaining a high brightness temperature in a compact emission region. These theories range from the more intuitive approach of injecting ultra-relativistic electrons in a short burst, to more exotic ones such as proton synchrotron radiation and coherent emission mechanisms in the form of maser. In Chapter 3, we review the main theoretical work over the years which explores mechanisms intrinsic or extrinsic to the source, in order to explain the apparently rapid flux variations or the extremely high brightness temperature inferred from variability.

This work aims to explain the occurrence of high brightness temperature in flat spectrum radio sources, inferred by observations of IDV, through the construction of a theoretical framework based on a modification to the intrinsic radiation mechanisms involved. The model can then be applied to sources which show intrinsic variability or sources which show high brightness temperature that cannot be accounted for by external effects alone. Realising that synchrotron power is strongly affected by the energy of the radiating particles, and that the reabsorption of synchrotron photon is dominated by low energy particles, we build our model base on electron synchrotron theory, and apply it to a non-conventional electron distribution − one which has a deficit of electrons at low energies.

We first approximate an electron distribution which has a low energy cut-off by monoenergetic electrons. The maximum brightness temperature that can be produced by this model and its parameter dependence is discussed in Chapter 4. We then examine the spectral properties of synchrotron emission from monoenergetic electrons in Chapter 5. Applying this model to an example of an IDV source S5 0716+714, it becomes clear that the simple monoenergetic assumption is insufficient, which then leads us to modified the model to a double power-law electron distribution that captures the characteristics of having a low energy cut-off by having a hard spectrum below a certain energy. The circular polarisation properties of synchrotron emission is examined in Chapter 6, where we study the transfer of radiation inside a source of monoenergetic electrons, taking into account the polarised absorptions as well as the Faraday effects. In Chapter 7, we recapitulate the important findings of this work, discuss the issues surrounding this model and the key difference of it from other models. Our concluding remark will be presented in Chapter 8.

Chapter 2

Maximum Brightness Temperature

In this chapter, we discuss three main processes that can limit the brightness temperature of a synchrotron source. Compton catastrophe acts to cool the synchrotron emitting energetic particles, hence reducing the emitted power. Induced Compton scattering acts to decrease the energy of synchrotron photons that are emitted at the frequency at the peak of the synchrotron spectrum, and in doing so the intensity at the peak of the spectrum is decreased. Copious electron-positron pair production by photon-photon interaction when the photon energy density is high confines the synchrotron photons in the source. The equipartition of energy density between the magnetic field and the particles in itself does not impose a limit on brightness temperature. It is however a common assumption since equipartition minimises the total energy content of a synchrotron source, and this assumption puts a restriction on the energy possessed by the particles. Equipartition is, therefore, included in this discussion as one of the brightness temperature limiting factor.

2.1   Compton catastrophe

In a compact source which contains highly energetic particles, the cooling effects of inverse Compton scattering cannot be ignored. The ratio of the inverse Compton scattering power to the synchrotron power is the ratio of the energy density of the photon field to the energy density of the magnetic field, U_{rad}/U_B, as shown by Eqs. (1.3) and (1.17). If the source has a low magnetic field B, such that synchrotron luminosity is low, or it is moving with a high bulk Lorentz factor Γ, such that the source sees a photon energy density of the cosmic microwave background (CMB) enhanced

by Γ, the cooling of the energetic particles by scattering off CMB photons becomes important. The energy density of the CMB photons is found by integrating over the Planck spectrum,

$$
\begin{aligned}
U_{\mathrm{CMB}} &= \frac{4\pi}{c} \int_0^\infty \frac{2h\nu^3}{c^2} \frac{1}{\exp(h\nu/k_{\mathrm{B}}T) - 1} \\
&= \frac{\pi^2 (k_{\mathrm{B}}T)^4}{15(\hbar c)^3}
\end{aligned}
\tag{2.1}
$$

For the CMB temperature of $T \approx 3$ K, U_{CMB}, as seen by the source, is $\sim \Gamma \times 10^{-12}\,\mathrm{ergs\,cm^{-3}}$. This becomes comparable to the synchrotron photon energy density if the magnetic field strength in the source is $< 5\Gamma\,\mu$G. In Chapter 4, we see that the magnetic field strength predicted by the model is many order of magnitude above this level, therefore, inverse Compton scattering of CMB photons is neglected.

Consider a homogeneous source which size is characterised by a single spatial scale R, radiating at a total luminosity, $L_{\mathrm{total}} = L_{\mathrm{s}} + L_{\mathrm{IC}}$, where L_{s} and L_{IC} are the luminosity of synchrotron radiation and of inverse Compton scattering, respectively. The power emitted by inverse Compton scattering is proportional to the total photon energy density, $U_{\mathrm{rad}} = L_{\mathrm{total}}/(cR^2)$. Therefore, the ratio

$$
\frac{L_{\mathrm{IC}}}{L_{\mathrm{s}}} = \frac{U_{\mathrm{rad}}}{U_B} = \frac{L_{\mathrm{total}}/(cR^2)}{U_B}
\tag{2.2}
$$

Rearrangement of Eq. (2.2) shows that the total luminosity of the source is

$$
L_{\mathrm{total}} = \frac{L_{\mathrm{s}}}{1 - \left(\frac{L_{\mathrm{s}}/(cR^2)}{U_B} \right)}
\tag{2.3}
$$

and $L_{\mathrm{s}}/(cR^2) = U_{\mathrm{s}}$ is the energy density of the synchrotron photons. We see from Eq. (2.3) that when the bracketed term on the right hand side of the equation approaches unity, the total luminosity of the source increases dramatically, causing it to cool catastrophically. The rapid rise in total luminosity implied by Eq. (2.3) when U_{s} approaches U_{B} is called the *Compton catastrophe*.

To examine the condition of catastrophic cooling of energetic electrons more closely, we assume an emission region of linear size R, with a homogeneous electron distribution which has a power-law form $n_{\mathrm{e}} \propto \gamma^{-s}$, embedded in a uniform magnetic field B. The synchrotron spectrum peaks at the frequency $\nu = \nu_{\mathrm{abs}}$, where the optical depth to synchrotron self-absorption is of the order of unity. Above this frequency

the intensity falls off as $I_\nu \propto \nu^{-(s-1)/2}$. Because more electrons become effective at absorbing the radiation as the frequency decreases, the optically thick part of the spectrum is not of the Rayleigh-Jeans type, $I_\nu \propto \nu^2$, but has instead $I_\nu \propto \nu^{5/2}$, independent of the power-law index of the underlying distribution, as described in Chapter 1. Correspondingly, the brightness temperature, defined in Eq. (1.1), peaks at $\nu \approx \nu_{\mathrm{abs}}$, falling off as $\nu^{1/2}$ to lower and as $\nu^{-(s+3)/2}$ to higher frequencies.

Consider optically thick synchrotron emission at the peak frequency ν_{abs}, $I_{\nu_{\mathrm{abs}}} = K\nu_{\mathrm{abs}}^{5/2}$, where K is a constant that depends on n_{e}, B and the range of electron energy, for our discussion we assume that these quantities remain constant. Rearranging Eq. (1.1), the synchrotron specific intensity at ν_{abs} can also be written as

$$I_{\nu_{\mathrm{abs}}} = K\nu_{\mathrm{abs}}^{5/2} = \frac{2\,\nu_{\mathrm{abs}}^2}{c^2}\,k_{\mathrm{B}}T_{\mathrm{B,max}}$$

$$\Rightarrow K = \frac{2\,\nu_{\mathrm{abs}}^{-1/2}}{c^2}\,k_{\mathrm{B}}T_{\mathrm{B,max}} \tag{2.4}$$

$T_{\mathrm{B,max}}$, the brightness temperature at ν_{abs}, is the maximum brightness temperature of the source. The photon energy density from an emission with specific intensity I_ν is

$$U_{\mathrm{ph}} = \frac{4\pi}{c}\int_\nu I_{\nu'}\mathrm{d}\nu' \tag{2.5}$$

For optically thick synchrotron emission from some minimum frequency $\nu_{\mathrm{min}} \ll \nu_{\mathrm{abs}}$ to ν_{abs}, the photon energy density U_{s} is

$$\begin{aligned} U_{\mathrm{s}} &= \frac{4\pi}{c}\int_{\nu_{\mathrm{min}}}^{\nu_{\mathrm{abs}}} K\nu'^{5/2}\mathrm{d}\nu' \\ &\approx \frac{16\pi}{7c^3}\nu_{\mathrm{abs}}^3 k_{\mathrm{B}}T_{\mathrm{B,max}} \end{aligned} \tag{2.6}$$

Since an electron at a particular energy $\gamma = k_{\mathrm{B}}T_{\mathrm{e}}/(mc^2)$, where $T_{\mathrm{e}} \sim \gamma mc^2/k_{\mathrm{B}}$ is the kinetic temperature of the electron, radiates most of its energy at a characteristic frequency $\nu_{\mathrm{s}} = \nu_0(k_{\mathrm{B}}T_{\mathrm{e}}/mc^2)$. When the source is optically thick, the brightness temperature approaches the kinetic temperature, and we can characterise the emission at ν_{abs} by associating it with the brightness temperature measured at this frequency as $\nu_{\mathrm{abs}} = \nu_0(k_{\mathrm{B}}T_{\mathrm{B,max}}/mc^2)$. This can be incorporated into the expression of U_{s} in Eq. (2.6), such that

$$U_{\mathrm{s}} = \frac{16\pi}{7c^3}\left[\frac{3eB}{4\pi mc}\left(\frac{k_{\mathrm{B}}T_{\mathrm{B,max}}}{mc^2}\right)^2\right]^3 k_{\mathrm{B}}T_{\mathrm{B,max}} \tag{2.7}$$

The condition to avoid Compton catastrophe, $U_\mathrm{s}/U_B < 1$, is [c.f. KP69]

$$\frac{U_\mathrm{s}}{U_B} = 2.5 \times \left(\frac{B}{1G}\right)\left(\frac{T_\mathrm{B,max}}{10^{12}\mathrm{K}}\right)^7 < 1 \tag{2.8}$$

alternatively,

$$\frac{U_\mathrm{s}}{U_B} = 0.1 \times \left(\frac{\nu_\mathrm{abs}}{5\mathrm{GHz}}\right)\left(\frac{T_\mathrm{B,max}}{10^{12}\mathrm{K}}\right)^5 < 1 \tag{2.9}$$

The inequality given in Eq. (2.8) is very sensitive to the brightness temperature of the source − if $T_\mathrm{B,max}$ is increased by even a factor 2, the ratio U_s/U_B increases by a factor of 128. We can rewrite the inequality in Eq. (2.9) into the ratio of the total luminosity L_total to luminosity of the synchrotron photons L_s by a Taylor expansion of the denominator of Eq. (2.3),

$$L_\mathrm{total} = L_\mathrm{s}\left[1 + \left(\frac{T_\mathrm{B}}{T_\mathrm{thresh}}\right)^5\right] \tag{2.10}$$

where T_B is the intrinsic brightness temperature at ν_abs (we drop the subscript "max" in $T_\mathrm{B,max}$ from now on) and $T_\mathrm{thresh} \approx 10^{12}\,\mathrm{K}$ at $\nu = \nu_\mathrm{abs} = 5GHz$, depending somewhat on the parameter s (which determines the energy in the electrons) and the magnetic field strength of the source, corresponding to spectral turn-over at frequency ν_abs at which the source becomes optically thin to synchrotron radiation [c.f. Rea94], as shown above.

2.2 Equipartition of energy

We begin our discussion on the reason behind the common assumption of equipartition of energy density between the magnetic field and the particles by computing the minimum energy content required by a synchrotron source to radiate at a certain luminosity. The total energy content of a source of volume V is the sum of the magnetic field energy and the energy in the particles, assuming an electron distribution of $n_\mathrm{e}(\gamma) = n_0\gamma^{-s} = n_0\gamma^{-(2\alpha+1)}$,

$$\begin{aligned} W_\mathrm{total} &= V\left(U_B + U_\mathrm{par}\right) \\ &= V\left(\frac{B^2}{8\pi} + a\int_{\gamma_\mathrm{min}}^{\gamma_\mathrm{max}} \gamma mc^2 n_\mathrm{e}(\gamma)\mathrm{d}\gamma\right) \end{aligned} \tag{2.11}$$

Other particles such as protons or positrons may also be present in the plasma, which would contribute to the total energy in the particles. This is accounted for by a factor of a. The inclusion of the factor a is sufficient, and the exact value of a is insignificant, as we will see later, since the calculation of Eq. (2.11) involves other approximations, so that the final result is only meant to be an estimate rather than an accurate evaluation, and the dependence on a in the final expression is small.

The energy radiated by an electron distribution through synchrotron emission is given in Eq. (1.3). The total synchrotron luminosity L_s of the electron distribution $n_e(\gamma)$ in a source of volume V is predominantly from the optically thin emission, since radiation energy is $\propto \nu I_\nu$. Therefore, the synchrotron luminosity is

$$
\begin{aligned}
L_s &= V \int_{\gamma_{\min}}^{\gamma_{\max}} n_e(\gamma) \frac{4}{3} \sigma_T c \gamma^2 U_B \mathrm{d}\gamma \\
&= \frac{4}{3} V \sigma_T c n_0 U_B \frac{\left(\gamma_{\max}^{2-2\alpha} - \gamma_{\min}^{2-2\alpha}\right)}{2 - 2\alpha}
\end{aligned}
\tag{2.12}
$$

Evaluating the integral on the right hand side of Eq. (2.11), the energy in the electrons is

$$
U_e = n_0 mc^2 \frac{\left(\gamma_{\max}^{1-2\alpha} - \gamma_{\min}^{1-2\alpha}\right)}{1 - 2\alpha}
\tag{2.13}
$$

As explained previously, an electron with a Lorentz factor γ radiates most of its energy at $\nu_0 \gamma^2$, we can substitute $\gamma_{\min}$ and $\gamma_{\max}$ in Eqs. (2.12) and (2.13) in favour of $\nu_{\min}$ and $\nu_{\max}$. The total electron energy can be expressed as a function of the total synchrotron luminosity,

$$
\begin{aligned}
VU_e &= \frac{3}{4}\left(\frac{2-2\alpha}{1-2\alpha}\right) \frac{mc^2}{\sigma_T c U_B} \nu_0^{1/2} \left(\frac{\nu_{\max}^{(1-2\alpha)/2} - \nu_{\min}^{(1-2\alpha)/2}}{\nu_{\max}^{(2-2\alpha)/2} - \nu_{\min}^{(2-2\alpha)/2}}\right) L_s \\
VU_{\mathrm{par}} &= VaU_e = aA(\alpha)L_s B^{-3/2}
\end{aligned}
\tag{2.14}
$$

The total energy content, following from Eq. (2.11), is therefore,

$$
W_{\mathrm{total}} = V \frac{B^2}{8\pi} + \frac{aA(\alpha)L_s}{B^{3/2}}
\tag{2.15}
$$

If we regard Eq. (2.15) as a function of B, we can determine the magnetic field that minimises the energy requirement of a synchrotron source by differentiating Eq. (2.15) with respect to B,

$$
B_{\min} = \left(\frac{6\pi aA(\alpha)L_s}{V}\right)^{2/7}
\tag{2.16}
$$

Replacing B in Eq. (2.15) in favour of $B_{\min}$, the minimum energy requirement is

$$W_{\min} = 0.49 V^{3/7} \left(a A(\alpha) L_{\mathrm{s}} \right)^{4/7} \tag{2.17}$$

The equipartition magnetic field is deduced by equating the two terms on the right hand side of Eq. (2.15),

$$B_{\mathrm{eq}} = \left(\frac{8\pi a A(\alpha) L_{\mathrm{s}}}{V} \right)^{2/7} \tag{2.18}$$

and the equipartition total energy content of the source can be found by replacing B in Eq. (2.15) by B_{eq} in Eq. (2.18),

$$W_{\mathrm{eq}} = 0.50 V^{3/7} \left(a A(\alpha) L_{\mathrm{s}} \right)^{4/7} = 1.02 W_{\min} \tag{2.19}$$

As shown by Eq. (2.19) and Fig. 2.1, the minimum energy content required by a synchrotron source of a certain luminosity L_{s} is very close to the equipartition value. There are no physical justification for the magnetic field and the particles in a source to be in equipartition of energy, it is however customary to use the equipartition magnetic field as a mean to estimate the energy content of a radio source.

In an analysis of high brightness temperature radio sources in which Doppler beaming is thought to be absent, Readhead (1994) [Rea94] measured a brightness distribution that cuts off at 10^{11} K; one order of magnitude lower than the inverse Compton limit. This appears consistent with observations of a sample of 48 sources showing superluminal motion [CRH$^+$03], in which it was found that the intrinsic brightness temperatures cluster around 2×10^{10} K. Readhead [Rea94] argued that an apparent maximum brightness temperature significantly lower than 10^{12} K could not be caused by catastrophic Compton cooling. Instead, he suggested that sources are driven towards equipartition between their magnetic and particle energy contents. Assuming, in addition, that observations are taken at the peak of the synchrotron spectrum, and that the electron distribution is a power-law, he showed that the equipartition brightness temperature (by assuming the magnetic field strength of the source equals the equipartition magnetic field) at an observing frequency $\nu_{\mathrm{obs}} = \nu_{\mathrm{abs}}$, in the rest frame of the observer, is

$$T_{\mathrm{eq}} = 5 \times 10^{10} \, \nu_{\mathrm{obs}}^{-0.03} \, S_{\mathrm{obs}}^{0.06} \, \mathcal{D}^{0.85} \ \mathrm{K} \tag{2.20}$$
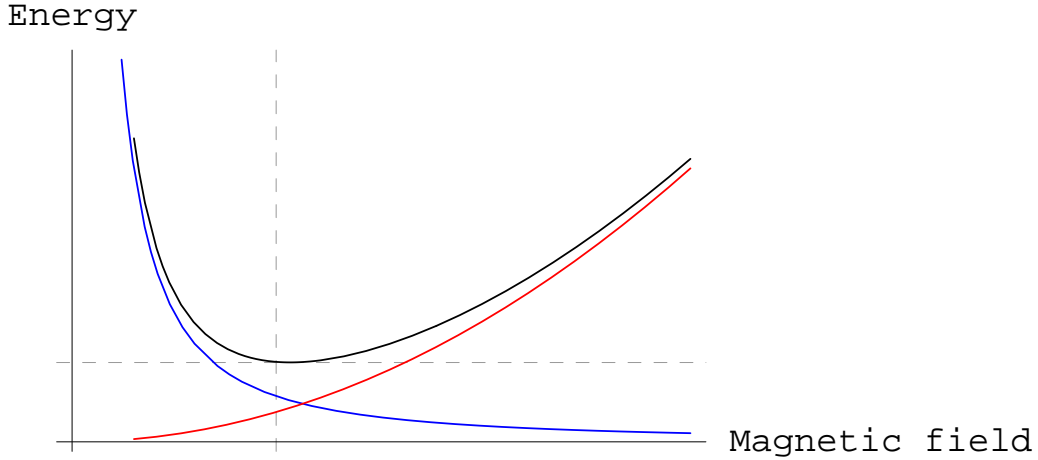
Figure 2.1: Schematic illustration of the total energy content of a source of synchrotron radiation in black, the total energy in the radiating particles in blue and the energy in the magnetic field in red.

where he has taken the synchrotron spectral index $\alpha = 0.75$, S_{obs} is the flux observed at ν_{obs} in janskys and $\mathcal{D}$ is the Doppler boosting factor (Here the Doppler factor $\mathcal{D} = \sqrt{1 - \beta^2}/(1 - \beta \cos \alpha)$ with βc the source velocity and α the angle between this velocity and the line of sight.). The equipartition brightness temperature is insensitive to either the observing frequency or the measured flux, and only mildly sensitive to the Doppler factor. However, Eq. (2.20) is valid only under the condition $\nu_{\text{obs}} = \nu_{\text{abs}}$.

2.3   Other processes

Two processes that act to reduce the number of synchrotron photons are discussed briefly below. Since these processes are not included in our model, we only summarise the ideas behind them.

2.3.1   Induced Compton scattering

Induced Compton scattering occurs as low energy electrons couple with high frequency photons. At frequencies below the synchrotron peak, where the optically thick

spectrum is independent of the power law index s of the electron energy distribution, the photon occupation number $n_\mathrm{p}(\nu) \propto I_\nu/\nu^3 \propto \nu^{-1/2}$. The transition rate of a photon from an initial state with occupation number $n_\mathrm{p}(\nu_1)$ into a final state with occupation number $n_\mathrm{p}(\nu_2)$ is $\propto [n_\mathrm{p}(\nu_2)+1]n_\mathrm{p}(\nu_1)$. Therefore, as the photon occupation number increases at the synchrotron peak due to a rise in intensity, the rate of photons departing this state and entering a state at lower frequency increases accordingly. This implies that in the presence of low energy electrons, the number of photons at the synchrotron peak, at which the brightness temperature is at its maximum, will be reduced when the synchrotron intensity reaches a certain threshold. Induced Compton scattering becomes an important process for reducing photon energy at a given frequency when the brightness temperature at that frequency approaches $T_\mathrm{B} > mc^2/(k_\mathrm{B}\tau_\mathrm{T}) = 5 \times 10^9$ K, assuming $\tau_\mathrm{T} \sim 1$, where k_B is the Boltzman constant [Syu71].

Sincell and Krolik (1994) [SK94] demonstrated by numerical simulations that relativistic induced Compton scattering limits the brightness temperature of a self-absorbed synchrotron source to $T_\mathrm{B} < 2 \times 10^{11} \nu_\mathrm{GHz}^{-1/(s+3)} \gamma_\mathrm{min}^{(s+2)/(s+5)}$ K, where ν_GHz is the observing frequency in unit of GHz, γ_min is the low energy cut-off in the electron spectrum which is $\propto \gamma^{-s}$. For a conventional power-law electron spectrum spanning down to $\gamma_\mathrm{min} = 1$, this gives a limit of $T_\mathrm{B} < 2 \times 10^{11}$ K at 1GHz.

2.3.2   Pair production

When soft photons are emitted by energetic electrons through synchrotron radiation, these synchrotron photons can then be repeatedly scattered by the energetic electrons that produced them, as described in Chapter 1. The γ-ray photons produced by the scattering of synchrotron photons may then have sufficient energy to produce electron-positron pairs when interacting with the synchrotron photons. The condition under which the production of pairs becomes significant can be measured in terms of the *compactness parameter*, ℓ, where [see, for example MK95]

$$\ell = \frac{L_\gamma}{cR^2}\frac{\sigma_\mathrm{T}R}{h\nu} \tag{2.21}$$

L_γ is the luminosity of the γ-ray photons in a region of radius R. The combination $L_\gamma/(cR^2h\nu)$ gives the number density of the γ-ray photons. The compactness parame-

ter, therefore, gives an approximate measure of the number of photons inside a cylinder of size $\sigma_{\mathrm{T}}R$, i.e. for $\ell > 1$, a γ-ray photon is expected to interact with another photon over a distance of R. In this case, the γ-ray photon may encounter and couple with a synchrotron photon before leaving the source, therefore reducing the number of photons that would otherwise contribute to the brightness temperature at synchrotron frequencies.

Chapter 3

Extrinsic and Intrinsic Variability

Sources that display IDV in their radio emission have an implied brightness temperature ranging from a few 10^{12} K to as high as $\sim 10^{21}$ K in the most extreme case (see Eq. (1.2) and [e.g., KKW$^+$03]). The observed variability may be intrinsic, which would require a very compact emission region with extreme conditions that enable the production of such high brightness temperatures. Alternatively, the variation can be introduced or modified by external factors such as interstellar scintillation or gravitational microlensing.

3.1   External effects

Relative motion between the source of IDV and the interstellar medium or the stars in the intervening galaxies or in our own galaxy may result in refraction, diffraction or gravitation microlensing (by stars) of the flux emitting by the original source. Whereas refraction and diffraction by the interstellar medium is frequency dependent and causes small amplitude fluctuations in the flux at low radio frequencies, microlensing is independent of frequency and focuses the flux such that the source appears brighter and more compact to the observer.

3.1.1   Interstellar scintillation (ISS)

Gradients in the particle density or turbulence in the interstellar medium result in variations in the refractive index along the line of sight, similar to the twinkling effect of the stars seen through the Earth's atmosphere. Since the amount of phase deviation of a wave propagating through a refractive medium is frequency dependent,

ISS is frequency dependent and is most effective at low radio frequencies. A review on the theoretical work on interstellar scintillation can be found in Rickett (1990) [Ric90] [see also Mel94], and extensive observation of variability induced by scintillating effects can be found in [e.g. LJB$^+$03, RLG06].

Interstellar scintillation can either be diffractive or refractive, depending on the size of the density inhomogeneities in relation to the size and distance of the source. In particular, for a source at a distance D emitting at frequency ν, if the length scale r of the density inhomogeneities is less than the Fresnel scale $r_{\rm F} \propto D/\nu$, diffractive scintillation can be observed, whereas refractive scintillation occurs on a scale $r \gtrsim r_{\rm F}$.

Another important factor that needs to be considered when interpreting IDV as a result of ISS, besides the size of the plasma inhomogeneity, is the distance of the screen of plasma. If the IDV is caused by refractive ISS, the size r of the screen must be able to cover the source of angular size $\theta = R/D$ (where R is the linear size of the source). That is, the screen would have to be placed at a distance l, such that $r > l\theta$. If variations on a time scale of Δt are due to a screen moving at a transverse speed v relative to the source, the scale of the inhomogeneities is approximately $r = v\Delta t$. Therefore, the distance of the screen cannot be further than $l < v\Delta t/\theta = (v\Delta t/R)D$, which typically puts the screen at a distance in our own galaxy. Since ISS is effective only at radio frequencies, any observed correlation between radio and optical variability would exclude the possibility of ISS as the cause of the variations.

Whereas in some cases, it is difficult to determine the cause of the rapid variability, for example, due to the episodic behaviour of the source variability, there are two types of behaviour which can conclusively demonstrate the presence of ISS. If the speed of the interstellar medium (ISM) is comparable to the speed of the Earth orbiting the Sun, then, for part of the year, the Earth is moving in the same direction as the ISM. During this period, the relative speed between the ISM and the Earth is low, and a longer variability time scale is observed. Six months later, the direction of the Earth is reverse, and it moves in the opposite direction to the ISM. The relative speed between the Earth and the ISM is increased and correspondingly, the variation time scale of the source appears shorter. This type of an annual cycle has been observed for several IDV sources such as in PKS 1519−273 by Jauncey et al (2003) [JJB$^+$03], as shown in

the upper panel of Fig. 3.1 in which both the unpolarised and polarised fluxes show a yearly periodic behaviour which coincide with that of the annual fluctuations of the relative ISM speed. The second conclusive feature is a time lag between the detection of the flux variability pattern between two widely separated telescopes. This technique can only be applied to sources with very short variability time scale (i.e., large fluctuation in a short period of time) so that a variability pattern can be measured to a precision of tens of seconds. Observations of pattern delay can be done in conjunction with the source annual cycle, during the period when the variations are most rapid. Such pattern delay was observed, for example, in PKS 1257−326 by Bignall et al (2006) [BMJ+06], between the Australia Telescope Array (ATCA) and the Very Large Array (VLA) in New Mexico. The result is shown in the lower panel of Fig. 3.1, in which the VLA measurements lag behind the ATCA measurements by several minutes.

3.1.2   Gravitational microlensing

Chang and Refsdal (1979) [CR79] drew attention to the significance of gravitational microlensing by an individual star in the lensing galaxy if the star crosses the line of sight to the observer. Although the deflection of the light ray coming from the distant source by the star is negligible compared to that caused by the lensing galaxy, they showed that the observed flux rises abruptly as the star approaches the light path, followed by a rapid decline as the star recedes.

The effect of gravitational microlensing was put forward as a scheme for a unified model of flat spectrum radio quasars (FSRQ) and BL Lac objects [see e.g. OV90, UP95]. As we have outlined briefly in Chapter 1, there are many similarities amongst the objects in the class of blazars. Whereas OVV and HPQ show strong emission lines, BL Lac objects lack these features but instead have strong featureless continuum emission. It was therefore suggested that continuum emission from a background quasar may be gravitationally focused and amplified by a star in an intervening galaxy. Line emission, on the other hand, originating from a more extended region, is not significantly affected by gravitational microlensing.

Gravitational microlensing affects all frequencies equally. The relative motion between the non-varying background quasar and the star, which causes the sudden rise
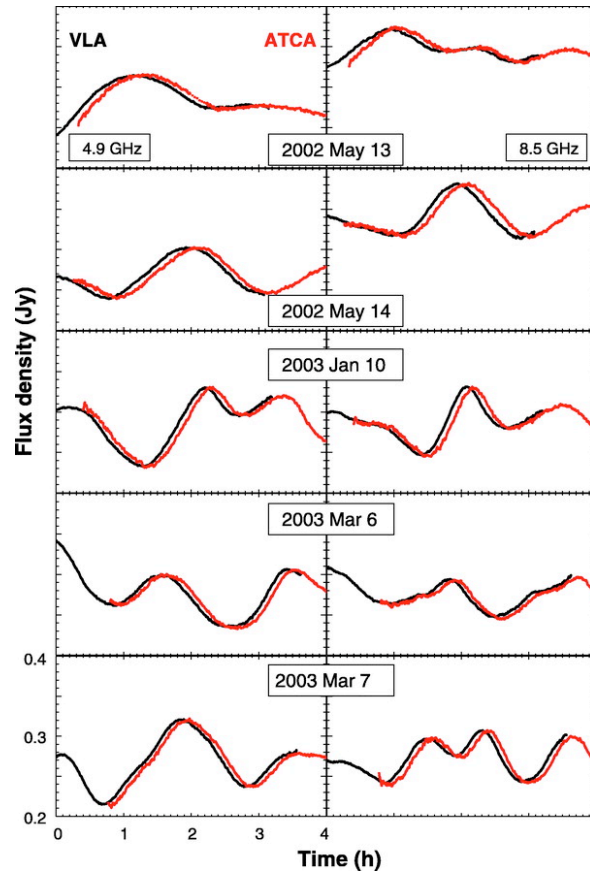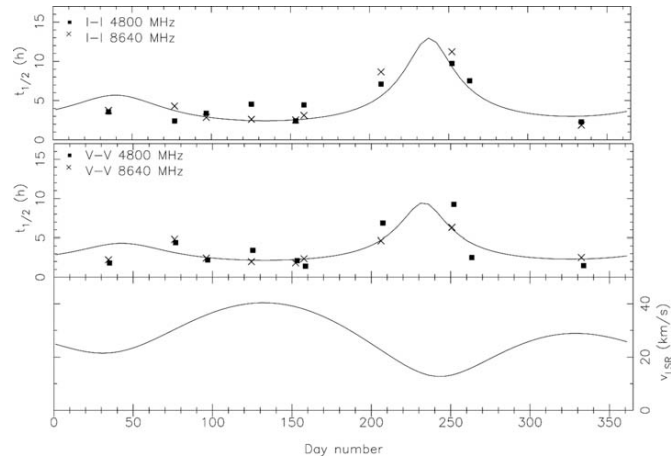
Figure 3.1: Upper panel [JJB[+]03]: Variation time scale measured at 4.8 and 8.6 GHz of PKS 1519−273 plotted against the day of the year. First box shows the total flux density, the second box shows the circularly polarised flux density and the third box shows the relative ISM speed. Lower panel [BMJ[+]06]: Simultaneous observations of PKS 1257−326 at 4.9 and 8.5 GHz at the VLA (black) and ATCA (red) on five days.

and decline in the flux of the continuum emission, can be the reason behind the observed intraday variations. Although the candidates for microlensing often show intraday variations, this effect is not the ideal explanation for a large number of IDV sources. Several reasons include (1) the fact that BL Lac objects are observed to be at the centers of their host galaxies, whereas it is possible for a microlensed quasar to be at other parts of the lensing galaxy. (2) The observed time scale of the variation Δt is related to the transverse speed v_{tr} and mass M of the lensing object by $\Delta t = v_{tr}^{-1}(M/M_\odot)^{0.5} 5 \times 10^{16}$cm (where $M_\odot$ is the solar mass). If Δt is of the order of 1 day, the relative transverse speed between the source and the lensing object becomes relativistic, and so the observed variations in some IDV sources are too fast to be caused by a star moving across our line of sight, (3) frequency dependent time lags have been observed in the variations in some of the sources, whereas microlensing is achromatic.

3.2 Intrinsic mechanisms

External effects have not been observed in all high brightness temperature sources, for example, the correlation observed between radio and optical variability in S5 0716+714, shown in Fig. 3.2, argues against interstellar scintillation. The variation time scale of S5 0716+714 is of the order of a few days. As explained above, this would suggest a transverse velocity between the source and the lensing star of relativistic speed. This can only be achieved by a relativistically moving source, in which case, intrinsic variation would play a much more significant role than gravitational microlensing.

Even though in some sources, the variations are caused by external effects, the implied brightness temperature are still greatly exceed 10^{12} K [e.g. KJW$^+$97, Md05]. Currently, the most extreme example is the source PKS 0405-385. This source displays diffractive scintillation [KJW$^+$97], which places an upper limit on its angular size that corresponds to a brightness temperature of 2×10^{14} K.

3.2.1 Doppler boosting

These sources are generally assumed to be relativistically beamed, i.e., to be in relativistic motion towards the observer [e.g., Ree66, JB73, SG85]. In this case the intrinsic temperature is lower than that deduced for a stationary source. Recall from
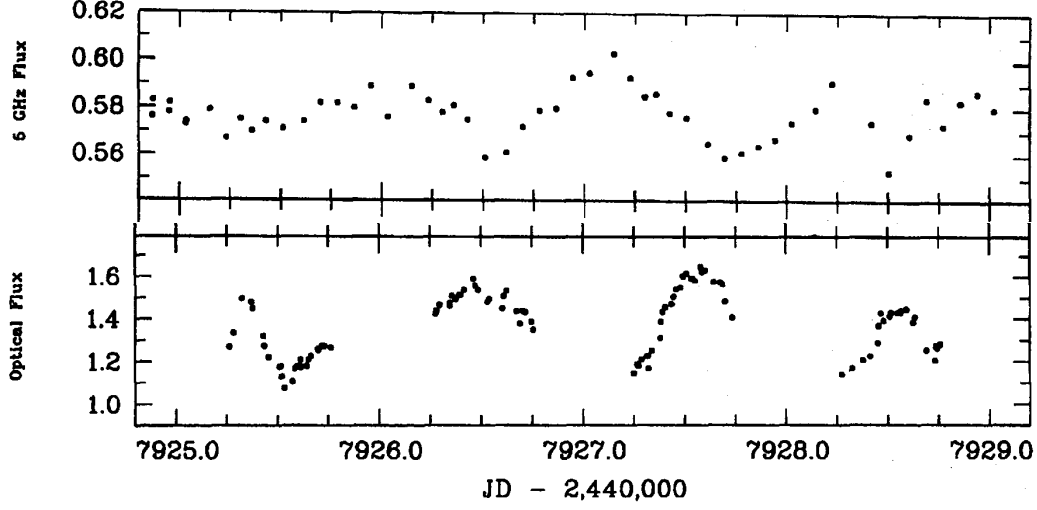
Figure 3.2: Upper panel shows the variations at 5 GHz in normalised intensities. Lower panel shows the variations at optical wavelenght (650 nm). The maxima of the radio flux appear to coincide with the minima of the optical flux. [WWH$^+$96]

Eq. (1.1) that

$$T_{\mathrm{B}} = \frac{c^2}{2k_{\mathrm{B}}} \frac{F_\nu}{\nu^2 \theta_{\mathrm{D}}^2} \tag{3.1}$$

For simplicity, we assume here that $z = 0$. In a scintillating source, its angular size, θ_{D}, can be deduced from the size and distance of the screen. Since I_ν/ν^3 is Lorentz invariant,

$$T_{\mathrm{B}} = \frac{c^2}{2k_{\mathrm{B}}\theta_{\mathrm{D}}^2} \frac{F'_\nu}{\nu'^2} \left(\frac{\nu}{\nu'}\right) = \frac{c^2}{2k_{\mathrm{B}}\theta_{\mathrm{D}}^2} \frac{F'_\nu}{\nu'^2} \mathcal{D} \tag{3.2}$$

The brightness temperature of a resolved source is therefore boosted by a factor of $\mathcal{D}$. For an unresolved source at a distance D that displays intrinsic variability, $\theta_{\mathrm{D}} = R/D = c\Delta t/D$ can only be estimated using the variation time Δt, which, in the comoving frame of the source, is increased by a factor of $\mathcal{D}$ such that $\Delta t' = \mathcal{D}\Delta t$. Therefore,

$$T_{\mathrm{B}} = \frac{D^2}{2k_{\mathrm{B}}} \frac{F'_\nu}{\nu'^2 \Delta t'^2} \mathcal{D}^3 \tag{3.3}$$

The brightness temperature is boosted by a factor of $\mathcal{D}^3$ if the variability is intrinsic.

Doppler factors estimated from observations of superluminal motion [CRH$^+$03] suggest $\mathcal{D} \sim 10 - 30$. The observed brightness temperatures in most sources, whether they show intrinsic variations or scintillation induced variations, are still too high to

be accounted for by Doppler boosting. Clearly, the intrinsic properties, dynamics and the underlying radiation mechanisms inside the source must be reconsidered in order to explain the inferred brightness temperature from the observations of IDV.

3.2.2 Proton-synchrotron radiation

Kardashev (2000) [Kar00] suggested that, since $T_{\mathrm{B}} \propto m^{9/7}$, the maximum brightness temperature can be up to $\sim 10^{16}$ K if the synchrotron emitting electrons are replaced by protons. Inspection of Eq. (2.6) shows that, if the dependence on m remains in the expression of U_{s}, Eq. (2.8) then reads,

$$\frac{U_{\mathrm{s}}}{U_B} = 0.1 \times \left(\frac{m}{m_{\mathrm{p}}}\right)^{-9} \left(\frac{B}{1G}\right) \left(\frac{T_{\mathrm{B,max}}}{10^{16}\mathrm{K}}\right)^7 < 1 \qquad (3.4)$$

where m_{p} is the mass of a proton. Due to the strong dependence on the mass of the particle, replacing electrons with protons as the synchrotron radiating particles allows the brightness temperature of the source to reach 10^{16} K without the onset of catastrophic Compton cooling of the energetic protons.

Recall that particles at a certain energy $k_{\mathrm{B}}T_{\mathrm{B}}/(mc^2)$ radiates synchrotron photons at the characteristic frequency

$$\nu_{\mathrm{s}} = \frac{3}{4\pi} \frac{eB}{mc} \left(\frac{k_{\mathrm{B}}T_{\mathrm{B}}}{mc^2}\right)^2$$

For electrons, the maximum brightness temperature of 10^{12} K is observed at GHz frequencies when the magnetic field is approximately 10 mG,

$$\nu_{\mathrm{s}} = 1.2\mathrm{GHz} \times \left(\frac{B}{10\mathrm{mG}}\right) \left(\frac{T_{\mathrm{B}}}{10^{12}\mathrm{K}}\right)^2 \left(\frac{m}{m_{\mathrm{e}}}\right)^{-3} \qquad (3.5)$$

However, in order to observe proton synchrotron radiation at GHz frequencies, a much stronger magnetic field is required,

$$\nu_{\mathrm{s}} = 1.9\mathrm{GHz} \times \left(\frac{B}{1G}\right) \left(\frac{T_{\mathrm{B}}}{10^{16}\mathrm{K}}\right)^2 \left(\frac{m}{m_{\mathrm{p}}}\right)^{-3} \qquad (3.6)$$

Another interpretation of the above results is that, in a source with a magnetic field of 1G in which both electrons and protons are present, if the proton synchrotron spectrum peaks at ≈ 1 GHz, the electron synchrotron spectrum peaks at ≈ 100 GHz. This implies that the majority of the proton synchrotron emission would be re-absorbed

by the electrons and would not be observed. Proton synchrotron emission can only be observed in regions with large magnetic field where energetic electrons are not accelerated as efficiently or lose their energy much more rapidly than protons as a result of synchrotron emission ($\mathrm{d}E/\mathrm{d}t \propto \sigma_\mathrm{T} \propto m^{-2}$).

3.2.3   Electron injection or re-acceleration

Slysh (1992) [Sly92] (also see [Kar00]) argued that in a source where radiative losses are compensated by either injections of relativistic electrons, or by constant re-acceleration of the electrons within the source, it is possible for a synchrotron source to sustain a brightness temperature of $\sim 10^{15}$ K in the period of ~ 1 day, provided that second order and higher scattering is suppressed by the Klein-Nishina effect.

Assuming that synchrotron losses is negligible compare to inverse Compton losses, by integrating Eq. (1.17) for single scattering, i.e., $U_\mathrm{rad} = U_\mathrm{s}$, where U_s is shown in Eq. (2.6), Slysh found that, as a function of time t, the electron energy

$$\gamma = \frac{\gamma_0}{\left(1 + \frac{4\pi\sigma_\mathrm{T}\nu_\mathrm{abs}^3 t}{c^2}\gamma_0^2\right)^{-1/2}} \tag{3.7}$$

Note that the second term in the denominator on the right hand side of Eq. (3.7) differs slightly from integrating Eq. (1.17) with U_rad given by Eq. (2.6) since there are small differences between our approximations when evaluating U_s and Slysh's approximations, but the difference is only of the order of unity. Provided that the initial energy of the electrons being injected into the emission region is large enough, such that the following inequality is satisfied

$$\gamma_0 \gg \frac{c}{\left(4\pi\sigma_\mathrm{T}\nu_\mathrm{abs}^3 t\right)^{-1/2}} \tag{3.8}$$

the resulting electron Lorentz factor can be approximated as

$$\gamma = \frac{c}{\left(4\pi\sigma_\mathrm{T}\nu_\mathrm{abs}^3 t\right)^{-1/2}} \tag{3.9}$$

At $\nu_\mathrm{abs} \sim 1$ GHz, Eq. (3.8) reads $\gamma_0 \gg 10^6 (t/\mathrm{days})^{-1/2}$. Eq. (3.9) implies an electron Lorentz factor of $\gamma \gtrsim 10^6$ within a period of 1 day if the inequality is satisfied. Therefore, at $\nu = \nu_\mathrm{abs}$ at which the kinetic temperature of the electrons equals the radiation (brightness) temperature, $T_\mathrm{B} \approx \gamma m c^2 / k_\mathrm{B} = 5 \times 10^{15}$ K.

Alternatively, instead of an initial injection of highly relativistic electrons, the electrons can be constantly accelerated inside the source. Assuming a first order Fermi acceleration process at the shock front of a strong shock, Slysh computed the electron energy as a function of time again by integrating Eq. (1.17) with $U_{\rm rad}$ given by Eq. (2.6), with the additional term a which gives the energy gain due to the acceleration by a strong shock with a shock front velocity V, such that

$$\frac{{\rm d}E}{{\rm d}t} = a - \left(\frac{{\rm d}E}{{\rm d}t}\right)_{\rm IC} \tag{3.10}$$

where $({\rm d}E/{\rm d}t)_{\rm IC}$ is given by Eqs. (1.17) and (2.6). The energy gain term a is related to the electron Larmour frequency $\nu_{\rm L}$ and the kinetic energy of the shock front by

$$a = \frac{3\pi}{10}\nu_{\rm L}m_{\rm e}V^2 \tag{3.11}$$

Eventually, the energy losses due to inverse Compton scattering is balanced by the energy gain due to acceleration, and the resulting electron energy is

$$\gamma = \left(\frac{V^2}{10\sigma_{\rm T}\nu_{\rm abs}^2}\right)^{1/5} \tag{3.12}$$

For a strong shock with a shock velocity $V \sim 0.1c$, the resulting electron Lorentz factor $\gamma = 6 \times 10^4$, and the brightness temperature $T_{\rm B} = 3 \times 10^{14}$ K.

At first sight, the two scenarios described above appear to be able to explain very high brightness temperature. However, Slysh's model neglected second and subsequent inverse Compton scattering. At such high photon energy density, one would expect inverse Compton scattering to be very effective, and with the presence of such high energy electrons, higher order scattering is also expected. In this case, this model fails to account for the possibility of Compton catastrophe. Another problem associated with this model arises from electron-positron pair production as the luminosity of the inverse Compton scattered photons increases. This will be discussed in more details in Chapter 4.

3.2.4 Source geometry

Geometric effects has been considered as a possible explanation to the observed high brightness temperature. Protheroe (2003) [Pro03] suggested that, if an elongated

source is observed end on, the resulting flux density would appear to be many orders of magnitude higher than if a source of the same radius is spherically symmetric.

In his model, Protheroe assumed a cylindrical source of length ℓ' (prime denote quantity measured in the comoving frame of the source) and radius $r = \theta_{\mathrm{D}} D$, where θ_{D} is the angular diameter and D is the distance from the source, containing a monoenergetic distribution of electrons. He further assumed there is equipartition of energy between the magnetic field and the particles. Estimating the electron Lorentz factor at the source by the flux F_{abs} measured at ν_{abs}, assuming that the observing frequency $\nu = \nu_{\mathrm{abs}}$ (see Eq. (1.1))

$$\gamma' = \frac{\gamma}{\mathcal{D}} = \frac{2}{3} \frac{F_{\mathrm{abs}}}{\mathcal{D} m \nu_{\mathrm{abs}}^2 \theta_{\mathrm{D}}^2} \tag{3.13}$$

At the self-absorption frequency ν_{abs}, the synchrotron optical depth $\tau_{\mathrm{s}} = 1$. Assuming the source is viewed along the axis of the cylinder, $\tau_{\mathrm{s}} = \alpha_\nu \ell'$, and

$$\tau_{\mathrm{s}} \propto \ell' \gamma^{-5/3} \tag{3.14}$$

(c.f. Eq. (A.11) in Appendix A in the limit $x \ll 1$) implying that the electron energy has a dependency of $\gamma \propto (\ell'/r)^{-3/5}$. Therefore, when observing at ν_{abs}, if the source is elongated, the electron energy required to produce a certain level of flux is reduced, hence the intrinsic brightness temperature $T_{\mathrm{B}} \propto \gamma$ can be lowered significantly if $(\ell'/r) \gg 1$.

However, since the dependence on (ℓ'/r) is relatively weak, this model requires an increase of (ℓ'/r) by approximately 2 orders of magnitude in order to reduce the Doppler boosting factor by 1 order of magnitude to account for the same brightness temperature. This model is also not able to explain fast variations in the observed flux since causality arguments would still limit the variability time scale of a cylindrical source to $t_{\mathrm{var}} \propto \ell'$. Also, as mentioned before in Chapter 1, IDV is observed frequently in many flat spectrum radio sources. Geometric effects which is only significant within a very small viewing angle is, therefore, not statistically favoured.

3.2.5   Coherent emission

Coherent emission mechanism in which relativistic electrons radiate collectively can naturally produce very high brightness temperature, depending on the size of the

coherent volume [e.g. LP92, BL98, BER05].

Eqs. (2.6) and (3.4) can be used to estimate the effect of coherent emission. Consider synchrotron emission by a collection of N electrons, the mass m and the charge e in Eqs. (2.6) and (3.4) are then replaced by Nm and Ne. The limiting brightness temperature becomes $T_{\mathrm{B}} \propto (Nm)^{9/7}(Ne)^{-3/7}B^{1/7}$, or, for electrons,

$$T_{\mathrm{B}} < 10^{12}\,\mathrm{K} \times \left(\frac{B}{1\mathrm{G}}\right)^{1/7} N^{6/7} \tag{3.15}$$

and the synchrotron characteristic frequency, after substituting T_{B} with Eq. (3.15) is

$$\nu_{\mathrm{s}} = 1.2\mathrm{GHz} \times \left(\frac{B}{10\mathrm{mG}}\right)^{5/7} N^{-2/7} \tag{3.16}$$

Therefore, to increase the brightness temperature at GHz frequenceis by increasing the number of coherently emitting electrons would require a large magnetic field.

This example only illustrates the possibility of coherent emission qualitatively, there are as yet no comprehensive model of coherent emission mechanisms suitable for application in blazars. Some of the central argument against coherent emission is that the observed emission shows features that resemble synchrotron radiation such as broad continuum emission, rather than any known form of coherent emission (see [Mel02] for discussion on arguments against coherent emission), and that induced Compton scattering would prevent the escape of the GHz photons produced this way and, therefore, the emission would not be observed.

Chapter 4

Synchrotron Emission from Monoenergetic Electron

In this chapter, we re-examine the limit of inverse Compton catastrophe and the assumption of equipartition of energy between magnetic field and particle energy density in a synchrotron source. The source is assumed to contain a monoenergetic electron distribution instead of the conventional power-law. Although this assumption appears at first sight highly restrictive, the form of the synchrotron emissivity means that under some circumstances such a distribution provides a good approximation to several more commonly encountered cases, including that of a conventional power-law distribution that is truncated to lower energy at a Lorentz factor $\gamma_{\min}$. Synchrotron emission from monoenergetic electrons was considered by Crusius-Waetzel (1991) [Cru91] and found to be able to reproduce brightness temperatures which exceed 10^{12} K. This model, however, is restricted by requirement of observing at the synchrotron self-absorption frequency ν_{abs}.

Monoenergetic distributions have been proposed in connection with radio sources for a variety of reasons: the absence of low energy electrons can account for the lack of Faraday depolarisation in parsec-scale emission regions [War77, JO77] and has recently been discussed in connection with statistical trends in the observed distribution of superluminal velocities as a function of observing frequency and redshift [GBW04]. Also, [BFC+06] recently examined the radio and x-ray emission from the lobe regions of a giant radio galaxies 6C 0905+3955, and deduced a low energy cutoff of the relativistic particles in the hotspots of $\gamma_{\min} \sim 10^4$.

In Sect. 4.1 we use standard theory to discuss the general properties of the synchrotron spectra emitted by a homogeneous source. A set of spatially averaged equa-

tions describing the evolution of the electron Lorentz factor and both the synchrotron and the associated inverse Compton scattered emission is presented in Sect. 4.2. Having identified in these equations the threshold for the inverse Compton catastrophe, we discuss the parameter space available to stationary solutions in Sect. 4.3. We report the results that temperatures considerably in excess of 10^{12} K are permitted, and show that in the case of resolved sources, the onset of catastrophic cooling occurs over a wide range of temperatures, consistent with the observed temperature range, which we previously reported in [KT06, TK07]. Finally, we address in Sect. 4.4 the suggestions by [Sly92] that extremely high brightness temperatures can be achieved in nonstationary sources either by injecting electrons at high energy, or by balancing their cooling against a powerful acceleration mechanism.

4.1   Synchrotron spectra

We consider a homogeneous source region characterised by a single spatial scale R, that contains monoenergetic electrons and possibly positrons of Lorentz factor γ and number density N_e immersed in a magnetic field B. Expressions for the synchrotron emissivity and absorption coefficients can be found in many excellent texts (e.g., Rybicki and Lightman [RL79, Chapter 6], and Longair [Lon92, chapter 18]).

For any given source there exists a frequency $\nu_{\rm abs}$ below which absorption is important, this will be explained in Section 4.3 when we discuss the model parameters. Since B and γ also define a characteristic synchrotron frequency $\nu_{\rm s}$ (see Eq. A.3), the sources we consider can be divided into two categories: those with **weak absorption** in which $\nu_{\rm abs} < \nu_{\rm s}$ and those with **strong absorption** $\nu_{\rm abs} > \nu_{\rm s}$. Note that this division is independent of the observing frequency, since it relates only to intrinsic source properties. The synchrotron spectra that emerge in these two cases are quite different, and are illustrated in Fig. 4.1. A feature they have in common is that the low energy spectrum has the Rayleigh-Jeans form $I_\nu \propto \nu^2$, where I_ν is the specific intensity at frequency ν. This property contrasts with the $\nu^{5/2}$ dependence of I_ν at low frequencies of a source containing a power-law distribution of electrons. The reason is that a power-law distribution contains cold (low energy) electrons that contribute to the absorption at low frequencies.

The brightness temperature, $T_\mathrm{B} = c^2 I_\nu / (2\nu^2 k_\mathrm{B})$, where k_B is Boltzmann's constant, is a function of frequency and is also illustrated in Fig. 4.1. At low frequency, it attains its maximum value roughly in "equilibrium" with the electrons: $T_\mathrm{B,max} = 3\gamma mc^2 / 4k_\mathrm{B}$, then decreases monotonically to higher frequencies. In the case of weak absorption, $T_\mathrm{B,max} \propto \nu^{-5/3}$ for $\nu_\mathrm{abs} < \nu < \nu_\mathrm{s}$, and then cuts off exponentially as $\nu^{-3/2} \exp(-\nu/\nu_\mathrm{s})$ once ν_s is exceeded. In strongly absorbed sources, the brightness temperature remains almost constant until the frequency exceeds ν_s upon which it falls off as ν^{-1} until the source becomes optically thin, after which the exponential cut-off $T \propto \nu^{-3/2} \exp(-\nu/\nu_\mathrm{s})$ takes over.

Although four parameters (γ, N_e, B and R) are needed to define a source model, the division between strong and weak absorption is simple. It occurs at a critical Lorentz factor γ_c given by (see Eq. A.10 in Appendix A)

$$\gamma_\mathrm{c} \;=\; 324 \times \left(\frac{N_\mathrm{e}}{1\,\mathrm{cm}^{-3}}\right)^{1/5} \left(\frac{R}{1\,\mathrm{kpc}}\right)^{1/5} \left(\frac{B}{1\,\mathrm{mG}}\right)^{-1/5} \tag{4.1}$$

or, equivalently,

$$\gamma_\mathrm{c} \;=\; 4451 \times \tau_\mathrm{T}^{1/5} \left(\frac{B}{1\,\mathrm{mG}}\right)^{-1/5} \tag{4.2}$$

where $\tau_\mathrm{T} = N_\mathrm{e} R \sigma_\mathrm{T}$ is the Thomson optical depth of the source. Strong absorption occurs for low Lorentz factors $\hat{\gamma} = \gamma/\gamma_\mathrm{c} < 1$ and weak absorption for high Lorentz factors $\hat{\gamma} > 1$. If the Lorentz factor γ is held constant, the strong absorption regime may be reached from the weak by increasing τ_T at constant B, or by **decreasing** B at constant τ_T.

In his model of high-brightness temperature sources, Slysh [Sly92] considered the strong absorption case. The most important property of the assumed distribution in this case is the lack of high energy electrons: the addition of a population of cold electrons, which would correspond to a power-law distribution truncated to higher Lorentz factors, would reduce the brightness temperature of the source at $x < 1$ (in Fig. 4.1) but would not significantly influence this quantity, for $x > 1$.

On the other hand, Crusius-Waetzel [Cru91] and Protheroe [Pro03] considered weak absorption, where the key property of the model distribution is the absence of low energy electrons. In this case, the monoenergetic model is a good approximation to a power-law distribution truncated to lower electron energies at $\gamma = \gamma_\mathrm{min}$. The addition

of a high-energy power-law tail affects the spectrum at $x > 1$, but does not change the maximum brightness temperature achieved at $x \lesssim 1$. Furthermore, the truncation need not be sharp: provided the opacity at low frequencies is dominated by the contribution of electrons with $\gamma \approx \gamma_{\min}$, the monoenergetic approximation is good. This is the case if, for $\gamma < \gamma_{\min}$, the spectrum is sufficiently hard: $dN/d\gamma \propto \gamma^{-q}$ with $q \leq 1/3$. In particular, the low energy tail of a relativistic Maxwellian distribution ($q = -2$) falls into this category.

In contrast to the pure power-law distribution, where the self-absorption turnover is strongly peaked, the emission of a weakly absorbed source — shown in red in the upper panel of Fig. 4.1 — is flat over nearly two decades in frequency. It therefore provides a natural explanation of compact flat-spectrum sources, eliminating the need to appeal to a "cosmic conspiracy" behind the superposition of peaked spectra from different parts of an inhomogeneous source [Mar80].

For the treatment of inverse Compton scattering, it is necessary to evaluate the the energy density $U_{\rm s}$ in synchrotron photons in a given source. To do this, I_ν must be integrated over angles and over frequency. The result depends on the geometry and optical depth as well as the position within the source. An average value can be estimated by introducing a geometry dependent factor, ζ, defined according to:

$$U_{\rm s} \;\; \approx \;\; \frac{4\pi\zeta}{c} \int_0^\infty d\nu \, \langle I_\nu \rangle \tag{4.3}$$

where $\langle I_\nu \rangle$ is conveniently taken to be the specific intensity along a ray path that is within the source for a distance R and is perpendicular to the local magnetic field. [Pro02] has evaluated ζ for several interesting special cases. For a roughly spherical source, it is of the order of unity. We show in the following section that the choice $\zeta = 2/3$ is consistent with our spatially averaged treatment of the kinetic equations. The dominant contribution to the integral over the spectrum arises from photons of frequency close to $\nu_{\rm s}$ in the case of weak absorption, and close to $\nu_{\rm abs}$ in the case of strong absorption. Using this approximation, for weak absorption ($\hat{\gamma} > 1$):

$$U_{\rm s} \;\; \approx \;\; 4.1 \times 10^{-6} \gamma^2 \zeta \left(\frac{B^2}{8\pi} \right) \left(\frac{N_{\rm e}}{1\,{\rm cm}^{-3}} \right) \left(\frac{R}{1\,{\rm kpc}} \right) \tag{4.4}$$

or, equivalently,

$$U_{\rm s} \;\; \approx \;\; 2\gamma^2 \tau_{\rm T} \zeta \left(\frac{B^2}{8\pi} \right) \tag{4.5}$$
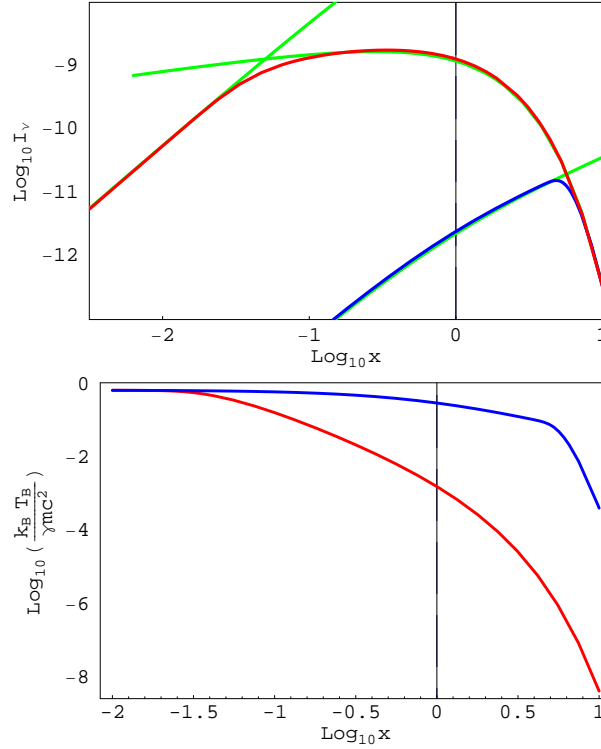
Figure 4.1: The synchrotron spectra (upper panel) and brightness temperatures (lower panel) of sources with monoenergetic electrons in the case of strong (blue) and weak (red) absorption. The green curves show the optically thick ($I_\nu = S_\nu$) and optically thin ($I_\nu = \tau_s S_\nu$) approximation. In the upper panel, I_ν is in arbitrary units, and in the lower, the brightness temperature is normalised to the energy of the electron. x is the ratio of the frequency to the characteristic synchrotron frequency of the electrons ν_s. The blue (red) curves correspond to a source which has an optical depth of unity to synchrotron self-absorption at $x \approx 5$ ($x \approx 0.05$). For ease of display, the upper panel compares sources with equal flux at high frequency, whereas the lower compares sources with equal flux at low frequency.

and for strong absorption ($\hat{\gamma} < 1$):

$$U_s \quad \approx \quad 8.9 \times 10^{-18} \gamma_c^7 \zeta \left(\frac{B^2}{8\pi} \right) \left(\frac{B}{1\,\mathrm{mG}} \right) (\ln \hat{\gamma})^2 \qquad (4.6)$$

An approximation that is accurate for all values of the optical depth is given in Eq. (A.23) of Appendix A.

4.2   Spatially averaged equations

An approximate, spatially averaged set of equations governing the energy balance of particles and synchrotron radiation in a source can be found following the approach

of Lightman and Zdziarski [LZ87] and Mastichiadis and Kirk [MK95]. In terms of the time-dependent synchrotron radiation energy density $U_0(t)$ one can write:

$$\frac{dU_0}{dt} + c\langle\alpha_\nu\rangle U_0 + \frac{c}{R}U_0 \quad = \quad \langle j_\nu\rangle \tag{4.7}$$

The second and third terms on the left-hand side of this equation represent the rate of energy loss by the radiation field due to synchrotron self-absorption and escape through the source boundaries; the right-hand side is the power put into radiation by the particles. The angle brackets indicate a frequency and angle average, but, within this spatially-averaged treatment, an exact calculation of the frequency average is unnecessary; it suffices to replace the absorption coefficient by its value where the energy density of the synchrotron spectrum peaks i.e., at $\nu = \nu_s$ in the case of weak absorption and $\nu = \nu_{abs}$ in the case of strong absorption. In terms of the optical depth to synchrotron absorption at this point, $\tau_p \leq 1$, the equation becomes:

$$\frac{dU_0}{dt} + \frac{c}{R}\left(1 + \tau_p\right)U_0 \quad = \quad \langle j_\nu\rangle \tag{4.8}$$

The right-hand side of this expression can now be found by demanding it gives the correct steady solution at both large and small optical depth. The resulting equation is:

$$\frac{dU_0}{dt} + \frac{c}{R}\left(1 + \tau_p\right)\left[U_0(t) - U_s(\gamma)\right] \quad = \quad 0 \tag{4.9}$$

where U_s is the steady-state synchrotron radiation energy density, evaluated according to Eq. (4.3), with an appropriate value of the parameter ζ.

The corresponding equation for the particles that takes into account synchrotron absorption and emission as well as an acceleration term takes the form

$$N_e mc^2 \frac{d\gamma}{dt} \quad = \quad \frac{c}{R}\tau_p U_0 - \frac{c}{R}\left(1 + \tau_p\right)U_s + a\,eBcN_e \tag{4.10}$$

The first term on the right-hand side of Eq. (4.10) is the power taken from the radiation field by self-absorption and the second term is that returned to it — both of these appear in Eq. (4.9). The third term describes the energy input by particle acceleration. The particular scaling used follows that of Slysh [Sly92], and models a generic first-order Fermi process. For a independent of γ, the acceleration rate is proportional to the gyro

frequency, and for $a = 1$ it equals this value. The acceleration timescale equals the crossing time of the source when $a = \gamma mc^2/(eBR)$.

Multiple inverse Compton scatterings can be accounted for as follows: First we label the photons present in the source according to how many scattering events they have suffered after production by the synchrotron process. The energy density of these photons is denoted by U_i Thus, $i = 0$ corresponds to photons emitted by the synchrotron process which have not undergone a scattering, and the corresponding energy density is governed by Eq. (4.9). Assuming the source is optically thin to Thomson (or Compton) scattering, the dominant loss mechanism for the energy density of photons belonging to a given generation $i \geq 1$ is escape from the source, rather than conversion to the $i+1$'th generation. In this case, we can write for the time-dependence of U_i:

$$\frac{\mathrm{d}U_i}{\mathrm{d}t} + \frac{c}{R}U_i = Q_i \tag{4.11}$$

where Q_i is the rate per unit volume at which energy is transferred into photons of the i'th generation by inverse Compton scattering, for $i \geq 1$, or by synchrotron radiation for $i = 0$.

If the inverse scattering process proceeds in the Thomson regime a simple expression can be found for Q_i. However, as i increases, $h\nu_i$ also increases, eventually becoming comparable to the electron energy when viewed in its rest frame. When this happens, Klein-Nishina modifications to the Thomson cross section become important, reducing the value Q_i. We take approximate account of this effect by limiting the number of scatterings to N_{max}, and using the Thomson approximation to evaluate Q_i for $i \leq N_{\mathrm{max}}$. In this case, the average energy of a scattered photon of the i'th generation is $\nu_i = 4\gamma^2\nu_{i-1}/3$ and the rate of such scatterings in unit volume of the source is $N_{\mathrm{e}}\sigma_{\mathrm{T}}cU_{i-1}/(h\nu_{i-1})$. Therefore

$$Q_i = \begin{cases} \xi cU_{i-1}/R & \text{for } 1 \leq i \leq N_{\mathrm{max}} \\ \\ 0 & \text{for } i > N_{\mathrm{max}} \end{cases} \tag{4.12}$$

where the parameter ξ is defined as

$$\xi = \frac{4}{3}N_{\mathrm{e}}\sigma_{\mathrm{T}}R\gamma^2$$

$$= \frac{4\gamma^2 \tau_T}{3} \tag{4.13}$$

The appropriate value of N_{max} is chosen by requiring the average energy of the N_{max} generation of photons viewed in the electron rest frame $\gamma(4\gamma^2/3)^{N_{\text{max}}} h\nu_0$ to be less than the electron energy:

$$N_{\text{max}} = \text{floor} \left[\frac{\ln\left(mc^2/h\nu_0\right)}{2\ln\gamma} + \frac{1}{2} \right] \tag{4.14}$$

For synchrotron radiation, Eq. (4.9) implies

$$Q_0 = \frac{c\tau_p}{R}(U_s - U_0) + \frac{c}{R}U_s \tag{4.15}$$

In the stationary case, $U_0 = U_s$, therefore Eq. (4.15) reads $Q_0 = cU_0/R$. Eqs. (4.12) and (4.15) then give $Q_1/Q_0 = \xi$. However, assuming scattering in the Thomson regime, the ratio of the energy lost by synchrotron radiation to that by inverse Compton scattering in the steady state equals the ratio of the energy density of the magnetic field to that of the target photons, i.e. $Q_0/Q_i = B^2/(8\pi U_{i-1})$, which, for $i = 0$, implies

$$\frac{Q_1}{Q_0} = \xi = U_s \frac{8\pi}{B^2}$$
$$\Rightarrow U_s = \xi \left(\frac{B^2}{8\pi} \right) \tag{4.16}$$

Comparison with Eq. (4.5),

$$U_s = \left(\frac{4\gamma^2 \tau_T}{3} \right) \left(\frac{B^2}{8\pi} \right) \approx 2\gamma^2 \tau_T \zeta \left(\frac{B^2}{8\pi} \right) \tag{4.17}$$

confirms that the spatially averaged kinetic equations are consistent with the choice $\zeta = 2/3$ for the geometry dependent factor.

Finally, the electron equation (4.10) acquires the additional loss terms from inverse Compton scattering:

$$N_e mc^2 \frac{d\gamma}{dt} = -\sum_{i=0}^{N_{\text{max}}} Q_i + a\,eBcN_e \tag{4.18}$$

The set of equations (4.11) and (4.18) can be rewritten by introducing the total energy density of scattered radiation:

$$U_T = \sum_{i=1}^{N_{\text{max}}} U_i \tag{4.19}$$

Then, using dimensionless variables according to $\hat{U} = U\left(8\pi/B^2\right)$, $\hat{t} = tc/R$ and $\hat{Q}_i = 8\pi c Q_i/(RB^2)$ one finds

$$\frac{d\hat{U}_T}{d\hat{t}} + [1 - \xi]\,\hat{U}_T \;=\; \xi\left(\hat{U}_0 - \hat{U}_{N_{\max}}\right) \tag{4.20}$$

If $U_{N_{\max}}$ remains always negligibly small, then all significant scatterings occur in the Thomson regime, and the set of equations (4.11) (for $i = 0$), (4.18), and (4.20) can be conveniently formulated in terms of three characteristic values of the Lorentz factor:

$$\frac{d\hat{U}_T}{d\hat{t}} \;=\; -\left[1 - (\gamma/\gamma_{\mathrm{cat}})^2\right]\hat{U}_T + (\gamma/\gamma_{\mathrm{cat}})^2\,\hat{U}_0 \tag{4.21}$$

$$\frac{d\hat{U}_0}{d\hat{t}} \;=\; -\hat{U}_0 + \hat{Q}_0 \tag{4.22}$$

$$\frac{d\gamma}{d\hat{t}} \;=\; -\gamma_{\mathrm{eq}}\left[\hat{Q}_0 + (\gamma/\gamma_{\mathrm{cat}})^2\,\hat{U}_T\right] + \gamma_{\mathrm{tr}}a \tag{4.23}$$

where γ_{eq} is chosen so that there is equipartition between particle and magnetic energy densities for $\gamma = \gamma_{\mathrm{eq}}$:

$$\gamma_{\mathrm{eq}} \;=\; B^2/(8\pi N_e mc^2) \tag{4.24}$$

γ_{cat} is given by setting $\xi = 1$

$$\gamma_{\mathrm{cat}} \;=\; \sqrt{\frac{3}{4\tau_T}} \tag{4.25}$$

and γ_{tr} corresponds to the maximum Lorentz factor of a particle that can be confined in the source, i.e., whose gyro-radius is less than R:

$$\gamma_{\mathrm{tr}} \;=\; eBR/(mc^2) \tag{4.26}$$

The significance of γ_{cat} can be seen from the steady state solution of Eqs. (4.21) and (4.22): $U_T = U_s/\left(\gamma_{\mathrm{cat}}^2/\gamma^2 - 1\right)$. For values of γ that approach γ_{cat} from below, the energy density in the radiation field, and, hence, the luminosity diverge. Thus, under the assumption that all scatterings take place in the Thomson limit, no stationary solutions can be found for

$$\gamma \geq \gamma_{\mathrm{cat}} \tag{4.27}$$

This phenomenon is the nonrelativistic or "Thomson" manifestation of the Compton catastrophe described in the Chapter 2. In the weak absorption limit, $\hat{U}_s = \gamma^2/\gamma_{\mathrm{cat}}^2$,

confirming the well-known result that the Compton catastrophe sets in when the energy density in synchrotron photons exceeds the magnetic energy density. However, this result does not apply to the case of strong absorption, where we find $\hat{U}_s \sim \gamma_{\mathrm{cat}}^5/\gamma_{\mathrm{c}}^5 \ll 1$. In this regime, the synchrotron radiation energy density can be much smaller than the energy density in the magnetic field at the point where catastrophic cooling sets in. Physically, the scattered photons feed on each other to produce the catastrophe in this regime, and do not require a substantial synchrotron photon density. In a realistic model, the divergence of the luminosity is prevented by Klein-Nishina effects, that effectively truncate the series in Eq. (4.19). For example, if $T_{\mathrm{B,max}} = 10^{12}\,\mathrm{K}$, at an observing frequency of $1\,\mathrm{GHz}$, so that $\gamma \approx 200$, then, from Eq. (4.14), the number of terms contributing to the sum is $N_{\mathrm{max}} = 2$.

4.3 Stationary solutions

In this section we consider a self-absorbed synchrotron source in a stationary state. We first compute the maximum brightness temperature attainable by an intraday variable source before it reaches Compton catastrophe. Since an IDV source cannot be resolved, we derive the brightness temperature limit by expressing the intrinsic source parameters in terms of observable parameters. We then examine the intrinsic parameters of a resolved source, where the linear size of the source can be specified.

4.3.1 Intraday variable sources

Denoting the electron characteristic frequency in the source by $\nu_0 = 3eB/(4\pi mc)$ and the Thomson optical depth corresponding to the monenergetic electrons by τ_{T}, the optical depth to synchrotron absorption τ_{s} is

$$\tau_{\mathrm{s}} = \frac{\sqrt{3}\tau_{\mathrm{T}}mc^2 K_{5/3}(x)}{4\alpha_{\mathrm{f}}h\nu_0\gamma^5} \tag{4.28}$$

(see Eqs. (A.9) to (A.11)) where

$$x = \frac{\nu(1+z)}{\mathcal{D}\gamma^2\nu_0} \tag{4.29}$$

ν is the observing frequency, $\mathcal{D} = \sqrt{1-\beta^2}/(1-\beta\cos\phi)$ is the Doppler boosting factor for a source moving at speed $c\beta$ at an angle ϕ to the line of sight. The characteristic

synchrotron frequency $\nu_s = \gamma^2 \nu_0 \sin\theta$, θ is the angle between the line of sight and the magnetic field B, which, for simplicity, we assumed to be $\approx \pi/2$, such that $\sin\theta \approx 1$. Inspection of Eq. (4.28) shows that, since the modified Bessel function $K_{5/3}(x)$ always increases with decreasing x, for any given set of parameters, there will always be a frequency ν_{abs} low enough, and therefore $K_{5/3}(x_a)$ large enough, for τ_s to increase beyond unity.

The observed brightness temperature T_B, related to the the specific intensity of radiation I_ν by Eq. (1.1) can be expressed as,

$$\frac{k_B T_B}{mc^2} = \frac{\mathcal{D}}{1+z}\left(\frac{\gamma F(x)}{2x^2 K_{5/3}(x)}\right)\left(1 - e^{-\tau_s}\right) \qquad (4.30)$$

For comparison with observations of intra-day variable sources, it is convenient to formulate the expression for the specific intensity in Eq. (1.16) in terms of quantities accessible to observation. Substituting the parameter x from Eq. (4.30) with ν_0 and γ, and then eliminating ν_0 and γ in favour of the new parameters ξ and τ_s according to Eqs. (4.13) and (4.28), the brightness temperature can be written as

$$\frac{k_B T_B}{mc^2} = \left(\frac{3^{3/2}mc^3}{4^5\pi e^2\nu}\right)^{1/5}\left(\frac{\xi\mathcal{D}^6}{(1+z)^6}\right)^{1/5}\left(\frac{1-e^{-\tau_s}}{4\tau_s^{1/5}}\right)\left(\frac{F(x)}{x^{9/5}K_{5/3}^{4/5}(x)}\right) \qquad (4.31)$$

The first term in parentheses on the right-hand side of this equation is independent of the source parameters. The third term in parentheses reaches a maximum of the order of unity at $\tau_p \sim 1$. The fourth, however, diverges for small x as $x^{-2/15}$. Thus, even with $\xi < 1$ and $\mathcal{D} < 10$, it is possible to find source parameters for which this formula gives an arbitrarily high brightness temperature at any specified observing frequency. The restriction $\xi < 1$ applies if in order to avoid catastrophic cooling. The divergence of T_B at small x can be constrained by introducing a parameter ν_{max}, such that optically thin synchrotron emission with $I_\nu \propto \nu^{1/3}$ extends only up to the frequency $\nu = \nu_{\text{max}}$. Optical observations of PKS 1519 -273, PKS 0405 -385 and J1819 $+3845$ [HW96, and Wagner, priv. comm.] indicate that $\nu_{\text{max}} \lesssim 10^{14}$ Hz.

Expressing Eq. (4.31) in terms of the observed (at $z = 0$) quantities and replacing x in favour of $\nu_{\text{max},14}$, we find, in the case of weak absorption, and at low frequency ($\nu \ll \nu_s$)

$$T_B = 1.2 \times 10^{14}\left(\frac{\mathcal{D}_{10}^6\xi}{(1+z)^6}\right)^{1/5}\left(\frac{1-e^{-\tau_s}}{\tau_s^{1/5}}\right)\nu_{\text{max}14}^{2/15}\nu_{\text{GHz}}^{-1/3}\ \text{K} \qquad (4.32)$$

where $\mathcal{D} = 10\mathcal{D}_{10}$ is the Doppler boosting factor, z is the redshift of the host galaxy, τ_{s} is the optical depth of the source at the observing frequency $\nu = \nu_{\mathrm{GHz}}$ GHz, and the characteristic synchrotron frequency of the electrons is $\nu_{\mathrm{s}} = \nu_{\mathrm{max},14} \times 10^{14}$ Hz.

According to Eq. (4.32), brightness temperatures of $T_{\mathrm{B}} \approx 10^{13}$ K, such as observed in the sources PKS 1519 -273 and PKS 0405 -385 [MKRJ00, RKJ02] can be understood within a simplified homogeneous synchrotron model in which $\xi \lesssim 1$, implying a relatively modest inverse Compton luminosity, i.e., no catastrophe. Even the extremely compact source J 1819 $+3845$, which has $T_{\mathrm{B}} \gtrsim 2 \times 10^{14}$ K can be accommodated in a catastrophe-free model provided the Doppler factor is greater than about 15. In each case, a hard spectrum is predicted, extending to $\nu_{\mathrm{max},14} \times 10^{14}$ Hz. Although the dependence of the brightness temperature on this parameter is quite weak, simultaneous observations in the radio to IR and optical [OWG$^+$06] have the potential to rule out this explanation on a source by source basis, which we will show in the next chapter.

A particularly interesting source property is the degree of intrinsic circular polarisation r_{c}. Assuming a pure electron-proton plasma [Mel80],

$$r_{\mathrm{c}} = \frac{1}{3}\left(\frac{2}{x\gamma^3}\right)^{1/3} \cot\theta\,\Gamma(1/3) \tag{4.33}$$

$$= 1.9 \times \left(\frac{\tau_{\mathrm{p}}}{\mathcal{D}_{10}\xi}\right)^{1/5} \nu_{\mathrm{max},14}^{1/5} \cot\theta\,\% \tag{4.34}$$

In the case of a power-law electron distribution, r_{c} changes sign when the optically thick regime is entered [JO77]. We will address this issue in Chapter 6. To order of magnitude, one can estimate the peak value using this expression, which is remarkably insensitive to all source parameters other than the magnetic field direction. Several extra-galactic sources of extremely high brightness temperature display circular polarisation at the percent level [Mac03], in particular PKS 1519-273 and PKS 0405-385. In the absence of a low energy cut-off in the electron distribution, the degree of polarisation is far too small to explain the observations (see Eq. (1.11). However, Eq. (4.34) shows that for a monoenergetic electron distribution, the intrinsic emission can be polarised at the percent level or above, depending on the geometry of the magnetic field configuration.

The ratio of energy density in the energetic electrons to that in the magnetic field

η, the total energy content of the source E_{total} and the ratio of the synchrotron cooling time scale t_{cool} to the light crossing time R/c can also be expressed in terms of the two observable quantities, ν_{GHz} and $\nu_{\text{max},14}$, and the Comptonisation parameter ξ and the linear size of the source R (see Appendix A):

$$\eta \ = \ 2.9 \times \left(\frac{\mathcal{D}_{10}}{1+z} \right)^{13/5} \left(\frac{\xi^8}{\tau_{\text{s}}^3} \right)^{1/5} \sin^2 \theta \, R_{-2}^{-1} \, \nu_{\text{max},14}^{-8/5} \, \nu_{\text{GHz}}^{-1} \tag{4.35}$$

$$E_{\text{total}} \ = \ 4.6 \times 10^{47} \left(\frac{\mathcal{D}_{10}}{1+z} \right)^{-14/5} \left(\frac{\xi}{\tau_{\text{s}}} \right)^{-4/5} \sin^{-2}\theta \, R_{-2}^{3} \, \nu_{\text{max},14}^{22/15} \, \nu_{\text{GHz}}^{30/17} \ \text{ergs} \tag{4.36}$$

$$\frac{ct_{\text{cool}}}{R} \ = \ 2.9 \times \left(\frac{\mathcal{D}_{10}}{1+z} \right)^{13/5} \left(\frac{\xi}{\tau_{\text{s}}} \right)^{3/5} \sin^2 \theta \, R_{-2}^{-1} \, \nu_{\text{max},14}^{-8/5} \, \nu_{\text{GHz}}^{-1} \tag{4.37}$$

where we have written the source size as $R = R_{-2} \times 0.01 \, \text{pc}$.

Eq. (4.35) shows that the total energy content of a self-absorbed synchrotron source which contains monoenergetic electrons is approximately equally divided between the energetic particles and the magnetic field, but will be dominated by the energy density in the relativistic particles in strongly Doppler boosted sources. Due to the same strong dependence on the Doppler boosting factor in Eq. (4.36), the total energy content of the source should not exceed 10^{47} ergs. The ration shown in Eq. (4.37) is an important determining factor for the validity of the monoenergetic assumption. If the electrons, travelling at a speed $v \sim c$, leave the emission region (characterise by linear scale R) before loosing a significant portion of their energy to synchrotron emission, the electron population within the source is then able to sustain a monoenergetic distribution. On the other hand, in a strong magnetic field in which synchrotron cooling is fast such that the quantity in Eq. (4.37) becomes < 1, the monoenergetic electron spectrum would evolve into $n_{\text{e}} \propto \gamma^{-2}$.

4.3.2 Resolved sources

In a seminal paper, [Rea94] discussed the distribution in brightness temperature of a sample of powerful sources whose angular size could either be measured directly, or constrained by interplanetary scintillation. In discussing these objects several simplifications must be made, even within the context of a homogeneous synchrotron model.

Firstly, in the two low frequency samples (81.5 MHz and 430 MHz) considered by Readhead [Rea94], the emission is thought to be almost isotropic. Doppler boosting is
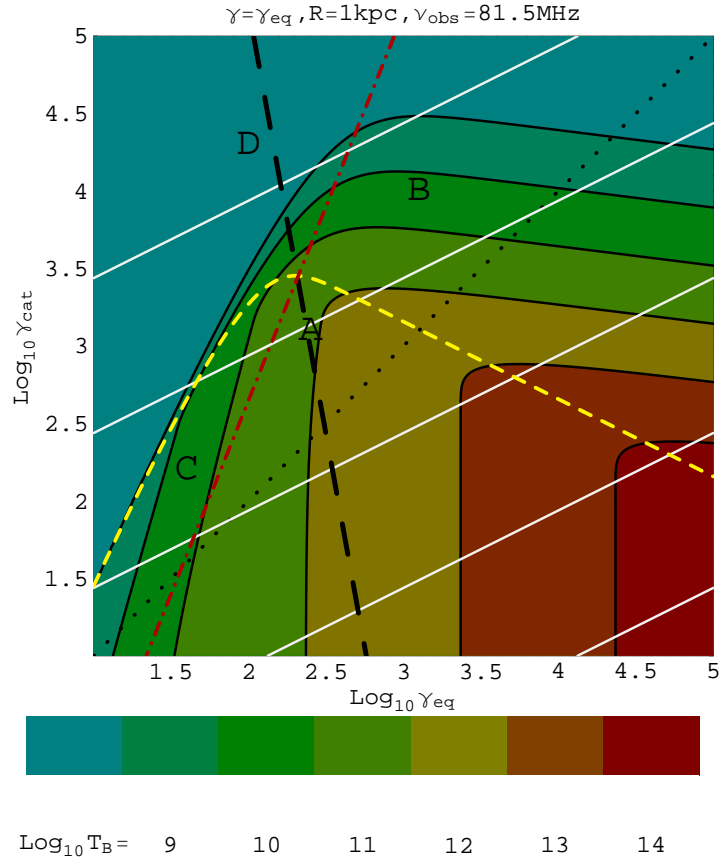
Figure 4.2: The brightness temperature as a function of γ_{eq} and γ_{cat} assuming equipartition between the magnetic and particle energy densities and a source size 1 kpc. Black contour lines indicate $\log_{10}(T/\text{Kelvin}) = 9, 10, 11, 12, 13$ and 14. The red dot-dashed line is the locus of points at which the characteristic synchrotron frequency of the emitting particles is 81.5 MHz, the yellow short dashed line shows where the source has an optical depth of unity at this frequency. The long dashed line divides regions of strong absorption (to the left) from those of weak absorption (to the right). The diagonal $\gamma_{eq} = \gamma_{cat}$ is shown as a dotted line. Contour lines of the magnetic field strength are shown in white, ranging from $\log_{10}(B/\text{Gauss}) = -4$ to 0 (in the bottom right-hand corner).

then unimportant and can be neglected. Secondly, these sources are not very compact; their extension on the sky is typically between 0.1 and 1 arcsec. Therefore, for our discussion we fix the linear extent R of the source to 1 kpc, corresponding to an angular size of approximately 0.2 arcsec at redshift $z = 1$. This leaves three parameters needed to specify the source model: the magnetic field strength B, the electron density N_e and the Lorentz factor γ of the electrons. In order to clarify the physics of a source,

we transform from the parameter set (B, N_e, γ) to the characteristic Lorentz factors γ_{eq} and γ_{cat} defined in Eqs. (4.24) and (4.25). Our basic parameter set is therefore $(\gamma_{eq}, \gamma_{cat}, \gamma)$. Finally, in order to display on a two-dimensional figure source properties such as brightness temperature and spectral slope at a particular frequency, we consider a slice through this three dimensional parameter space, selecting parameters such that the particle and magnetic energy densities are in equipartition: $\gamma = \gamma_{eq}$.

The properties of source models on this slice are shown in the γ_{eq}–γ_{cat} plane in Fig. 4.2. This plane can immediately be divided into regions of strong and weak absorption, as defined in Eq. (4.1). The boundary, drawn as a thick dashed line, represents the locus of the points at which $\gamma_c = \gamma_{eq}$. Weakly absorbed sources lie towards higher γ_{eq} and γ_{cat} (i.e., the upper-right side) and strongly absorbed sources towards lower γ_{eq} and γ_{cat} (i.e., the lower-left side). We also show (in white) contours of the magnetic field strength.

The remaining source properties depend upon the choice of observing frequency. In Fig. 4.2 we take this to be $81.5\,\mathrm{MHz}$, corresponding to the low frequency sample discussed by [Rea94]. In order to determine the spectral slope of a given source, we plot as a yellow short dashed line the locus of points where the observing frequency coincides with the frequency at which the optical depth to absorption is unity, ν_{abs}. Sources that lie above this line (on the side of larger γ_{cat}) are optically thin at the chosen observing frequency. In addition, the red dot-dashed line in Fig. 4.2 gives the locus of points where the observing frequency equals the characteristic frequency of synchrotron radiation ν_c. By definition, the intersection point of these lines lies also on the boundary between weak and strong absorption (the long dashed line). The observing frequency lies below ν_c on the lower-right side of the dot-dashed line. The (colour) shading gives the intrinsic brightness temperature at the chosen observing frequency.

The two lines (yellow short dashed and red dot-dashed) divide the γ_{eq}-γ_{cat}-plane in Fig. 4.2 into four regions with differing spectral properties: in region A, sources have a Rayleigh-Jeans spectrum $I_\nu \propto \nu^2$, in region B, the spectrum is that of low frequency, optically thin synchrotron radiation $I_\nu \propto \nu^{1/3}$, in region C, it is close to $I_\nu \propto \nu$ [see Sly92] and in region D it falls off exponentially $I_\nu \propto \nu^{-1/2} \exp(-\nu/\nu_c)$. Consequently,

flat spectrum sources reside in region B, preferentially close to the yellow short dashed line and in region C, preferentially close to the red dot-dashed line.

Sources that are in equipartition and lie below the threshold of the Compton catastrophe are to be found in the upper left half of Fig. 4.2, above the dotted line on which $\gamma_{\mathrm{eq}} = \gamma_{\mathrm{cat}}$. The maximum brightness temperature accessible to these sources occurs close to $\gamma_{\mathrm{eq}} = \gamma_{\mathrm{cat}} = 10^3$, and is approximately $10^{12.6}\,\mathrm{K}$, in rough agreement with the results of Kellermann and Pauliny-Toth [KP69], who, however, did not assume their sources to be in equipartition. The brightest sources are weakly absorbed, (they lie to the right of the long dashed line) and have a magnetic field strength of a few milliGauss. Their optical depth to synchrotron self-absorption lies close to unity at the observation frequency (they lie close to the yellow short dashed line).

Singal and Gopal-Krishna [SG85] first discussed the effects of the additional assumption of equipartition on bright sources and used it to estimate Doppler factors for rapidly variable sources. Later, Readhead [Rea94] introduced the concept of an "equipartition brightness temperature" to explain the observation that the temperature distribution of resolved sources appears to peak significantly below $10^{12}\,\mathrm{K}$. However, the crucial additional assumptions in his treatment is that the source flux is measured at the "synchrotron peak", and that the electron distribution is a power-law in energy. This implies that the opacity at a given frequency (e.g., at the synchrotron peak) is dominated by those electrons with a corresponding characteristic frequency. In our model, in which the electron distribution is approximated as monoenergetic, these assumptions are roughly equivalent to demanding that the source lies on the red dot-dashed line in Fig. 4.2 if it is weakly absorbed (i.e., on the boundary of regions B and D), and on the yellow short dashed line if it is strongly absorbed (i.e., on the boundary of regions C and D). This leads to a maximum brightness temperature of a few times $10^{10}\,\mathrm{K}$, as found by [Rea94]. Furthermore, as noted by Readhead [Rea94], such sources lie far from the threshold temperature, achieved along the dotted line in Fig. 4.2.

Replacing the assumption that the source flux is measured at the synchrotron peak, by the requirement that its spectrum be flat, i.e., that it lie in region B of Fig. 4.2, one sees that a wide range of brightness temperatures is available for sources

in equipartition, extending up to the threshold temperature found by Kellermann and Pauliny-Toth [KP69]. Thus, the observed temperature distribution is not explained by the assumption of equipartition.

4.4   Time dependence and acceleration

In order to explain the occurrence of brightness temperatures above 10^{12} K, Slysh [Sly92] formulated a model involving a monoenergetic electron distribution in a strongly absorbed source, in the sense that $\gamma < \gamma_c$, where γ_c is defined in Eqs. (4.1) and (4.2). He considered two scenarios, (i) a time-dependent one in which electrons were injected at arbitrarily high Lorentz factors and allowed to cool and (ii) one in which a strong continuous re-acceleration of the electrons led to a high brightness temperature equilibrium.

In each case, the assumption that the source is strongly absorbed leads to extreme values of the parameters. For example, in the first scenario in which high energy particles are injected into the source, [Sly92] finds that a brightness temperature of $T_B > 5 \times 10^{15}$ K can be sustained over 1 day at an observing frequency of 1 GHz. This is clearly in conflict with our analysis. The electron Lorentz factor required to achieve this temperature is $\gamma > 10^5$. However, the condition that the source is strongly absorbed, which is used in this model to estimate the cooling rate, combined with the condition $\nu_s \approx 1$ GHz required for a flat spectrum, leads to an extremely large Thomson optical depth, $\tau \approx 130$, as well as an implausibly low magnetic field $B \approx 2 \times 10^{-11}$ G. The parameter ξ that determines the inverse Compton luminosity is approximately 10^{12}, which implies an extremely large compactness of the inverse Compton radiation from the source. The resulting copious pair production invalidates the analysis and, ultimately, reduces the brightness temperature achievable in the radio range. The same criticism applies also to the second scenario described by [Sly92] in which acceleration balances inverse Compton losses to provide a brightness temperature of 10^{14} K at 1 GHz.

In the absence of Klein-Nishina effects on the scattering cross section, we find the time dependence of the particle and photon energies can be described by the three ordinary differential equations (4.21), (4.22) and (4.23). Inspection of these shows that if the threshold temperature is exceeded ($\gamma > \gamma_{cat}$), the inverse Compton luminosity

grows in a timescale of roughly the light-crossing time of the source. Thus, the threshold can only be substantially exceeded if the acceleration process in Eq. (4.23) operates on a shorter timescale. However, these equations employ a spatial average over the emission region. Although a rapid acceleration rate might be achieved locally in small regions of the source, once an average is taken, no timescale in the system can be shorter than the light-crossing time of the region over which the accelerated particles are distributed. In this case, the threshold temperature cannot be significantly exceeded.

At first sight, Klein-Nishina effects offer a possible escape from this conclusion. If even the first order scattering is suppressed, which requires extremely large Lorentz factors for the electrons ($\gamma > 10^{10}$ is needed for Klein-Nishina effects when scattering $10\,\mathrm{GHz}$ photons), the strong reduction in the rate of cooling by inverse Compton scattering suggests that higher brightness temperatures T_B might be possible.

This is, however, not the case, because the rate of production of electron-positron pairs by photon-photon interactions becomes important. The strength of this effect, which is not included in our model equations, is measured by the compactness parameter, ℓ, defined in Eq. (2.21). The luminosity of the γ-ray photons can be written as $L = U_{N_\mathrm{max}} c R^2$, such that

$$\ell = \frac{\sigma_T R U_{N_\mathrm{max}}}{h \nu_{N_\mathrm{max}}} \tag{4.38}$$

where U_{N_max} is defined in Eq. (4.11), N_max in Eq. (4.14), and ν_{N_max} is taken to be $(4\gamma^2/3)^{N_\mathrm{max}} \nu_0$. When $\ell > 1$, one expects the pair-production rate to be roughly equal to the light-crossing time of the source. This leads to a sharp rise in the Thomson optical depth, invalidating the assumption of scatter-free escape of synchrotron photons that is implicit in our model. The associated confinement of these photons reduces the brightness temperature.

We illustrate this in Fig. 4.3, where we compare two models with the same linear size R (and observing frequency), but different electron densities N_e and different values of B, chosen as follows: For any given set of parameters, R, B and N_e, and observing frequency ν_obs, the optical depth to synchrotron absorption τ_s, as defined in Eq. (4.28), has a single maximum as a function of γ, located close to the point where ν_obs equals the characteristic synchrotron frequency. If the source is optically thick to absorption

at this point, then $\gamma < \gamma_c$, as described in Sect. 4.1, and the brightness temperature is roughly $3\gamma mc^2/4k_B$. If, on the other hand, the source is optically thin at this point, then $\gamma > \gamma_c$, but the brightness temperature, given approximately by $\tau_s \times 3\gamma mc^2/4k_B$, decreases to higher γ, as can be seen from Eq. (4.28). Thus, assuming inverse Compton scattering does not intervene, the maximum brightness temperature is observed at a frequency such that $\tau_s \approx 1$, when $\gamma = \gamma_c$, which implies $x \approx 1$. These conditions are imposed on the parameters of the models presented in Fig. 4.3. In addition to the source size, chosen to be $R = 0.01\,\text{pc}$ and the observing frequency, set to $1\,\text{GHz}$, this leaves one free parameter, which we choose to be the optical depth to Thomson scattering τ_T.

The upper panel in Fig. 4.3 shows the time-dependence of the brightness temperature found by solving Eqs. (4.11) and (4.18) numerically for sources with $\tau_T = 0.01$ (dashed black line) and $\tau_T = 1$ (solid black line), without allowance for Doppler boosting ($\mathcal{D} = 1$). These sources have $\gamma_c = 10^{3.6}$ and $\gamma_c = 10^{4.3}$, respectively and, in the absence of inverse Compton cooling, they could potentially achieve brightness temperatures of $T_B \approx 10^{13.2}\,\text{K}$ and $T_B \approx 10^{13.9}\,\text{K}$. In order to do so, rapid acceleration is required, since for these source parameters, inverse Compton cooling leads to a time-asymptotic value of the Lorentz factor that is somewhat lower than γ_c for slow acceleration. The exact value of the asymptotic solution depends on the strength of the acceleration. For acceleration on the light-crossing timescale, it corresponds to $a \approx \gamma/\gamma_{tr}$ [see Eq. (4.23)]. In Fig. 4.3 we choose $a = 1.5\gamma/\gamma_{tr}$, which leads to an overshoot that slightly exceeds γ_c.

For $\tau_T = 0.01$, the compactness, shown as a function of time by the gray dashed line, remains well below unity, so that the effects of pair production can be neglected. However, this is not the case for $\tau_T = 1$. Here, the compactness (solid gray line) rises rapidly, reaching unity at $\hat{t} \approx 0.25$, where $T_B \approx 3.5 \times 10^{12}\,\text{K}$, well below its potential maximum. Thus, the attempt to gain higher brightness temperature by increasing τ_T, and, hence, γ_c, leads to a breakdown in the model assumptions due to pair production.

The lower panel of Fig. 4.3 shows the electron Lorentz factor and the optical depth to synchrotron self-absorption τ_s as functions of time for the case $\tau_T = 0.01$. The Lorentz factor (black dashed line) overshoots both its time-asymptotic value and
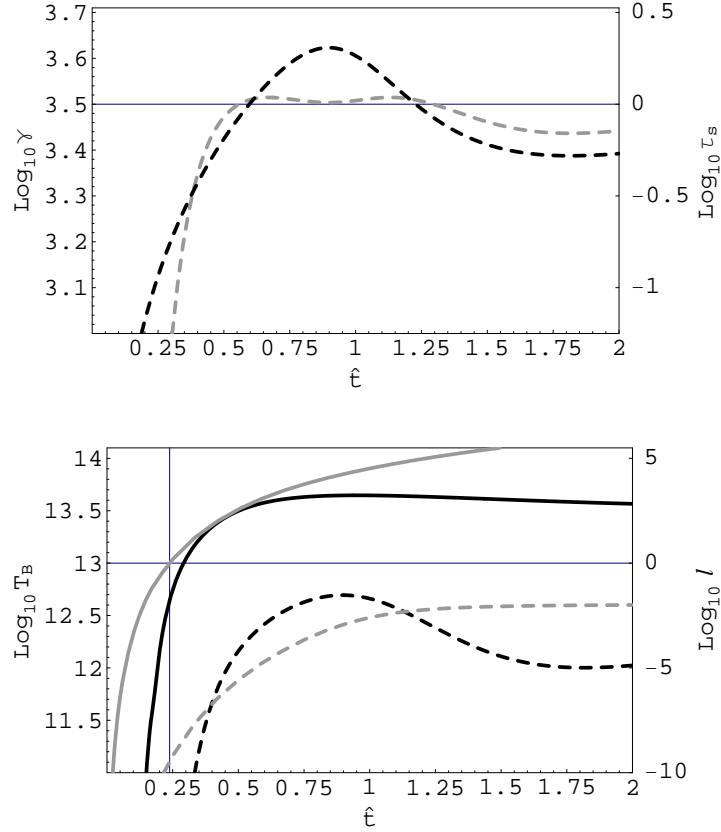
Figure 4.3: **Upper panel**: The brightness temperature T_B (black), and the compactness ℓ (gray) as functions of time, for two stationary, local sources ($\mathcal{D} = 1$, $z = 0$) with linear size $R = 0.01$ pc, observed at $1\,\mathrm{GHz}$. The Thomson optical depth is $\tau_T = 0.01$ (dashed lines) and $\tau_T = 1$ (solid lines) and the remaining parameters are chosen such that the optical depth to synchrotron self-absorption $\tau_s \approx 1$ at $\gamma = \gamma_c$ (see Eqs. (4.1) and (4.2)). A horizontal line is drawn to indicate $\ell = 1$. **Lower panel**: The electron Lorentz factor (black dashed) and the optical depth to synchrotron self-absorption τ_s (gray dashed) for the case $\tau_T = 0.01$. A horizontal line indicates $\tau_s = 1$.

γ_c. Correspondingly, the optical depth, (shown as the gray dashed line) which initially rises with γ, reaching unity at $\gamma = \gamma_c$ goes through a maximum very shortly afterwards. However, the overshoot is not sufficient to push τ_s back below unity, and the maximum brightness temperature, which coincides with the maximum Lorentz factor, remains at $T_B = 5 \times 10^{12}\,\mathrm{K}$, somewhat below the value of $T_B \approx 10^{13.2}\,\mathrm{K}$, estimated for large optical depth.

Chapter 5

Spectral Implications of Low Energy Electron Cut-Off

In Chapter 4, we discussed a synchrotron self-Compton model with monoenergetic electrons. The lack of low energy electrons enables more GHz photons to emerge from the source, allowing the source to sustain a higher brightness temperatures without initiating catastrophic cooling. We found that a temperature of up to $T_{\rm B} \sim 10^{14}$ K at GHz frequencies is possible with only a moderate Doppler boosting factor of ~ 10. In this chapter, we discuss in more details the spectral properties of synchrotron emission from an electron distribution with low energy cut-off, and show that, as well as being able to explain the high brightness temperature in IDV's, the characteristic synchrotron spectrum of $F_\nu \propto \nu^{1/3}$ can well explain the inverted radio spectra displayed by many compact radio sources.

In the following sections, we present our computation and analyse the properties of the synchrotron self-Compton spectra of the low energy electron cut-off model. First we present the model spectra computed using the approximation of monoenergetic electrons, as described in the previous chapter and Tsang and Kirk [TK06]. We then present a modification of the model, in which we adopt an electron distribution that combines two power-law spectra at a characteristic energy. The double power-law electron spectrum captures the low frequency spectral properties of synchrotron emission from monoenergetic electron, while at high frequency, the spectral behaviour is determined by the power-law electrons above the characteristic energy. In order to fulfil this "quasi-monoenergetic" criteria, the electron spectrum must rise faster than $\gamma^{-1/3}$ below the characteristic energy, such that the synchrotron opacity is dominated by electrons of the characteristic energy. Above the characteristic energy, the spec-

trum must fall faster than γ^{-1}, so that the distribution of electron number density, $N_e \propto \gamma^{1-s}$ (where electron phase space distribution $n_e \propto \gamma^{-s}$), congregates at energy towards the characteristic energy. For our discussion, we choose the low energy part to have the relativistic Maxwellian form ($\mathrm{d}N_e/\mathrm{d}\gamma \propto \gamma^2$), with the high energy part falls off as a power-law $\mathrm{d}N_e/\mathrm{d}\gamma \propto \gamma^{-s}$, where $s > 1$. Assuming that the electrons are being continuously accelerated while inside the source, the double power-law electron distribution described above is constantly injected into the source. The stationary electron spectrum is deduced by balancing the injection with losses from radiative cooling and the escape of the electrons from the source. Since we assume losses due to inverse Compton scattering is small, we do not consider non-linear SSC cooling.

In section 5.1, we briefly describe the monoenergetic model discussed in our previous paper, and then introduce the model in which a quasi-monoenergetic distribution of electrons, as described above, is injected. The stationary electron distribution is found in section 5.2, where we present the computation of the synchrotron and inverse Compton spectra. We first discuss the observation, then apply our model to the BL Lac object S5 0716+714, one of the best-studied IDV sources, in section 5.3, where we compare spectra predicted by our models with the observed data. This is the most suitable candidate for testing our model due to its extensive simultaneous observation spanning from radio to optical frequencies, as well as INTEGRAL observation at GeV $\gamma-$ray energies. The results are shown and discussed in section 5.3.

5.1   The Model

The homogeneous monoenergetic model discussed in the previous chapter can be completely characterised by the Doppler boosting factor $\mathcal{D}$, the red-shift of the host galaxy z, and four source parameters, the electron number density N_e, the magnetic field strength B, the linear size of the source R and the electron Lorentz factor γ. For the purpose of comparison with observations, these can be transformed into a different set of parameters, as shown in the Chapter 4 (see also [KT06]), in which N_e, B and γ are replaced by the characteristic frequency of the synchrotron spectrum, $\nu_s = \gamma^2 \nu_0$, where $\nu_0 = 3eB/(4\pi mc)$, the Comptonisation parameter, $\xi = 4\gamma^2 \tau_T/3$ (where $\tau_T = N_e R \sigma_T$ is the Thomson optical depth), which is the ratio of the luminosity

of each successive generation of inverse Compton scattered photons to the luminosity of the previous generation, and the self-absorption frequency ν_{abs}, specified by setting the synchrotron optical depth $\tau_{\mathrm{s}} = 1$. The size of the source is retained in the new set of parameter, which can be constrained, for example, by applying a causality argument to the variability time, Δt, of the source, such that the linear size of the source $R < c\Delta t \mathcal{D}/(1 + z)$.

As we show later in Section 5.3, the monoenergetic model cannot reproduce the multi-wavelength spectrum of S5 0716+714. Therefore, in the following, we outline the parameters that describe a model in which a double power-law electron distribution is injected that can be approximated as monoenergetic for the purpose of computing its low frequency synchrotron radiation, but at high frequency gives rise to a power-law spectrum.

5.1.1 Injection of relativistic electrons

The injection spectrum takes the form $Q(\gamma) \propto (\gamma/\gamma_{\mathrm{p}})^{-s}$, where the power law index s equals s_1 for $\gamma < \gamma_{\mathrm{p}}$, and s_2 for $\gamma > \gamma_{\mathrm{p}}$ (shown as solid lines in fig. 5.1). The number density of electrons with $\gamma < \gamma_{\mathrm{max}}$ at a given time is proportional to γ^{1-s} for $s \neq 1$ and $\propto \ln \gamma$ for $s = 1$. Therefore, in order to avoid a build up of electrons at high γ, we require that $s_2 > 1$ in the high energy branch. In the low energy branch $\gamma < \gamma_{\mathrm{p}}$, we first require $s_1 < 1$ such that electron number density congregates towards γ_{p} and synchrotron opacity is dominated by electrons with $\gamma = \gamma_{\mathrm{p}}$. We further require that the synchrotron opacity be dominated by electrons at γ_{p}, this is achieved by demanding $s_1 < 1/3$, so that at low frequency, the synchrotron spectrum is dominated by emission from electrons at $\gamma = \gamma_{\mathrm{p}}$. Assuming $s_1 < 1/3$ and $s_2 > 1$, the injection spectrum is well approximated by a monoenergetic electron distribution with Lorentz factor γ_{p}, and therefore considered quasi-monoenergetic.

The electron injection spectrum extends from γ_{min} to γ_{max}. The exact value of γ_{min} is relatively unimportant, since synchrotron emission and opacity are both dominated by electrons with $\gamma = \gamma_{\mathrm{p}}$ in the low energy part of the injection spectrum. γ_{max} determines the cut-off in the synchrotron spectrum, $\nu_{\mathrm{max}} = \gamma_{\mathrm{max}}^2 \nu_0$, and dictates the highest photon energy achievable through inverse Compton scattering which is

approximately $\gamma_{\mathrm{max}} mc^2$.

To summarise, the injection spectrum has the form

$$Q(\gamma) = Q_0 \begin{cases} \left(\frac{\gamma}{\gamma_{\mathrm{p}}}\right)^{-s_1}, & \gamma_{\mathrm{min}} \leq \gamma < \gamma_{\mathrm{p}} \\ \\ \left(\frac{\gamma}{\gamma_{\mathrm{p}}}\right)^{-s_2}, & \gamma_{\mathrm{p}} \leq \gamma < \gamma_{\mathrm{max}} \end{cases} \tag{5.1}$$

where Q_0 is the electron injection rate per unit volume per unit γ at $\gamma = \gamma_{\mathrm{p}}$, the Lorentz factor at which the break in the power law spectrum occur.

The electron spectrum in this model is a function of γ, therefore the Comptonisation parameter ξ is defined more generally as

$$\xi = \frac{4}{3} R \sigma_{\mathrm{T}} \int_0^\infty \gamma^2 \left(\frac{\mathrm{d}N_{\mathrm{e}}}{\mathrm{d}\gamma}\right) \mathrm{d}\gamma \tag{5.2}$$

replacing N_{e} with $N_{\mathrm{e}}\delta(\gamma - \gamma_{\mathrm{p}})$, we retrieve $\xi = 4\gamma_{\mathrm{p}}^2 N_{\mathrm{e}} R \sigma_{\mathrm{T}}/3$ for monoenergetic electrons. We determine the exact form of $(\mathrm{d}N_{\mathrm{e}}/\mathrm{d}\gamma)$ in the next section by balancing electron injection with losses due to radiation and the escape of electrons from the source.

The two Lorentz factors that are needed to completely specify the injection spectrum and the stationary electron distribution $- \gamma_{\mathrm{p}}$, the position of the break in the injection spectrum, and γ_{cool} determines at what electron energy radiative cooling dominates over losses due to particles escaping the emission region. γ_{cool} is defined as the Lorentz factor at which the radiative cooling time equals the light crossing time, where we assume the velocity of highly relativistic particles $v \sim c$,

$$\left.\frac{1}{t_{\mathrm{cool}}}\right|_{\gamma = \gamma_{\mathrm{cool}}} = \frac{4\sigma_T U_{\mathrm{B}}}{3mc}(1 + \xi)\gamma_{\mathrm{cool}} = \frac{1}{t_{\mathrm{esc}}}$$

$$\gamma_{\mathrm{cool}} = \frac{3}{4}\frac{mc}{\sigma_{\mathrm{T}}}\frac{1}{t_{\mathrm{esc}}U_{\mathrm{B}}(1 + \xi)} \tag{5.3}$$

where $t_{\mathrm{esc}} = R/c$ is the light crossing time of a source of linear size R, σ_{T} is the Thomson cross-section and $U_B = B^2/(8\pi)$ is the magnetic energy density. Although the factor $(1 + \xi)$ only accounts for the cooling effect of the first inverse Compton scattering, for $\xi \ll 1$, the effect of subsequent scattering ($\propto \xi^2$, ξ^3 etc.) is small. In the special cases when ξ is close to unity, Klein-Nishina effects reduces the cross-section of high order scattering, and the number of scatterings that occurs in the Thomson regime rarely reaches 2 [see Chapter 4 or TK07].
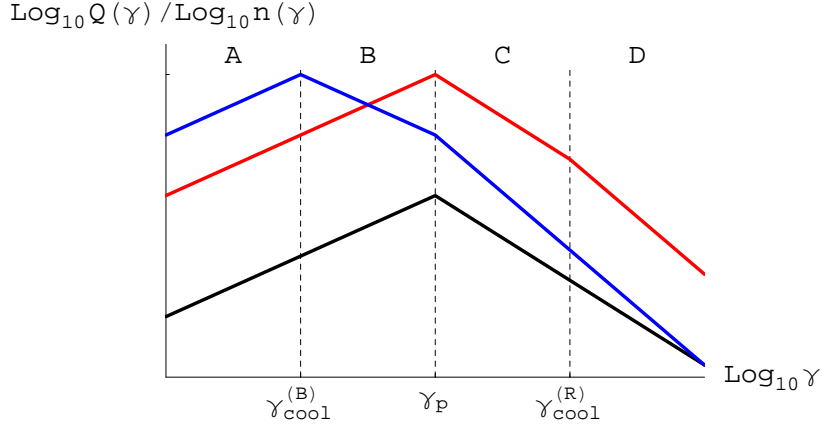
Figure 5.1: Schematic representation of the electron injection spectrum and the stationary differential number density as a function of γ. The height of the spectra have been adjusted for easy comparison and are not to scale. Black line shows the double power law injection spectrum with power law index s_1 for $\gamma < \gamma_{\rm p}$, and s_2 for $\gamma > \gamma_{\rm p}$. Red line shows the case where $\gamma_{\rm cool} = \gamma_{\rm cool}^{\rm (R)} > \gamma_{\rm p}$ and blue line shows the case where $\gamma_{\rm cool} = \gamma_{\rm cool}^{\rm (B)} < \gamma_0$.

5.2   Stationary solution

The spectral shape of the synchrotron spectrum is determined by the stationary electron energy distribution. Electrons are injected into the source according to Eq. (5.1), and are then subjected to radiative cooling while in the source, or evacuate this zone in a time-scale of the order of the light crossing time, $t_{\rm esc} \sim R/c$. The evolution of the energy distribution is governed by the kinetic equation [Kar62],

$$\frac{\partial n_{\rm e}}{\partial t} = Q_0 \left(\frac{\gamma}{\gamma_{\rm p}}\right)^{-s} - \frac{\partial}{\partial \gamma}\left(n_{\rm e}\dot{\gamma}\right) - \frac{n_{\rm e}}{t_{\rm esc}} \qquad (5.4)$$

where, for simplicity, we replace the differential electron number density with $n_{\rm e} = (\mathrm{d}N_{\rm e}/\mathrm{d}\gamma)$ from here on. The radiative cooling rate can be written as $\dot{\gamma} = \gamma^2/(\gamma_{\rm cool}t_{\rm esc})$. The second and third term on the right hand side of Eq. (5.4) are the loss rate due to radiative cooling and due to electrons leaving the emission region, respectively, and are roughly equal when $\gamma = \gamma_{\rm cool}$.

For $t_{\rm esc}$ independent of γ, the stationary solution of Eq. (5.4) is the general

solution

$$n_{\mathrm{e}}(\gamma) = \frac{1}{f_{\mathrm{I}}(\gamma)} \int^{\gamma} \frac{Q\left(\gamma''\right)}{\dot{\gamma}''} f_{\mathrm{I}}\left(\gamma'\right) \mathrm{d}\gamma'' \tag{5.5}$$

with the integrating factor

$$f_{\mathrm{I}}(\gamma) = \dot{\gamma} \exp\left[-\int^{\gamma} \left(\dot{\gamma}' t_{\mathrm{esc}}\right)^{-1} \mathrm{d}\gamma'\right] \tag{5.6}$$

However, we note that for the purpose of computation, the exact solution is unnecessary, since several assumptions have already been made at earlier stages. Instead we simplify Eq. (5.4) by dividing it into two regions. In the region where $\gamma \ll \gamma_{\mathrm{cool}}$, particles vacate the source before they cool. The effect of the second term on the right hand side of Eq. (5.4) is negligible and is therefore discarded. In the region where $\gamma \gg \gamma_{\mathrm{cool}}$, radiative cooling becomes significant and dominates over the effect of particle escaping the source. Therefore, in this region, we neglect the third term on the right hand side of Eq. (5.4). The stationary solution to Eq. (5.4) is then approximately,

$$n_{\mathrm{e}} = \begin{cases} t_{\mathrm{esc}} Q_0 \left(\frac{\gamma}{\gamma_{\mathrm{p}}}\right)^{-s}, & \gamma_{\mathrm{min}} \leq \gamma < \gamma_b \\ \\ \frac{1}{\dot{\gamma}} \int_{\gamma}^{\gamma_{\mathrm{max}}} Q_0 \left(\frac{\gamma'}{\gamma_{\mathrm{p}}}\right)^{-s} \mathrm{d}\gamma', & \gamma_b \leq \gamma < \gamma_{\mathrm{max}} \end{cases} \tag{5.7}$$

Since the equations in Eq. (5.7) are approximations to the exact solution at $\gamma \ll \gamma_{\mathrm{cool}}$ and $\gamma \gg \gamma_{\mathrm{cool}}$, the intersection is at $\gamma = \gamma_b \approx \gamma_{\mathrm{cool}}$ rather than at exactly $\gamma = \gamma_{\mathrm{cool}}$. Both γ_b, found by equating the two approximations, and γ_{p} give rise to breaks in n_{e} and therefore correspond to breaks in the synchrotron spectrum, at $\nu_{\mathrm{p}} = \gamma_{\mathrm{p}}^2 \nu_0$ and $\nu_{\mathrm{cool}} = \gamma_{\mathrm{cool}}^2 \nu_0$.

Integrating the expression of n_{e} for $\gamma_{\mathrm{cool}} \leq \gamma < \gamma_{\mathrm{max}}$, we obtain

$$n_{\mathrm{e}} = \frac{1}{\dot{\gamma}} \frac{Q_0}{\gamma_{\mathrm{p}}^s} \left(\gamma_{\mathrm{max}}^{(1-s)} - \gamma^{(1-s)}\right), \quad \gamma_b \leq \gamma < \gamma_{\mathrm{max}} \tag{5.8}$$

Notice that for $\gamma \ll \gamma_{\mathrm{max}}$, if $s < 1$ (as in the injection spectrum below γ_{p}), n_{e} is approximately proportional to $\dot{\gamma}^{-1} \propto \gamma^{-2}$. Whereas if $s > 1$ (as in the injection spectrum above γ_{p}), n_{e} is approximately $\propto \gamma^{-(s+1)}$.

Two types of stationary spectra result from Eq. (5.7), according to where the peak of the injection spectrum, γ_{p}, lies in relation to γ_{cool}. Fig. 5.1 shows the injection spectrum as a black line, the stationary spectra where $\gamma_{\mathrm{p}} > \gamma_{\mathrm{cool}}$ as a blue line and where

$\gamma_{\mathrm{p}} < \gamma_{\mathrm{cool}}$ as a red line. When the dominant loss mechanism is from electrons escaping the source ($t_{\mathrm{esc}} < t_{\mathrm{cool}}$), the spectrum retains its original shape, $N_{\mathrm{e}} \propto \gamma^{-s}$, since t_{esc} is independent of particle energy (region A in fig. 5.1 for the blue line, $\gamma_{\mathrm{cool}} < \gamma_{\mathrm{p}}$, and both regions A and B for the red line, $\gamma_{\mathrm{cool}} > \gamma_{\mathrm{p}}$). On the other hand, when only synchrotron losses are important, such that $t_{\mathrm{esc}} > t_{\mathrm{cool}}$, the stationary solution is $N_{\mathrm{e}} \propto \gamma^{-2}$ for $\gamma < \gamma_{\mathrm{p}}$ (region B for the dotted line), and $N_{\mathrm{e}} \propto \gamma^{-(s+1)}$ for $\gamma > \gamma_{\mathrm{p}}$ (regions C and D for the blue line and region D for the red line). For the computation of the low frequency synchrotron emission, the first case (blue line) can be approximated by a monoenergetic spectrum at γ_{cool} and the second case (red line) by a monoenergetic spectrum at γ_{p}.

5.2.1   Synchrotron and inverse Compton emission

The synchrotron specific intensity, following straight-forwardly from the radiative transport equation, is

$$I_{\nu}^{(\mathrm{S})} = S_{\nu} \left[1 - \exp(-\tau_{\mathrm{s}}) \right] \tag{5.9}$$

where the optical depth to synchrotron absorption is $\tau_{\mathrm{s}} = \alpha_{\nu} \cdot R$, and is defined in Eq. (1.12) as

$$\alpha_{\nu} = \frac{3\sqrt{3}}{16} \frac{\sigma_{\mathrm{T}}}{\alpha_{\mathrm{f}}} \frac{mc^2}{h\nu} \frac{\nu_{\mathrm{L}} \sin\phi}{\nu} \int_{\gamma_{\min}}^{\gamma_{\max}} \gamma^2 F(x) \frac{\mathrm{d}}{\mathrm{d}\gamma} \left(\frac{n_{\mathrm{e}}(\gamma)}{\gamma^2} \right) \mathrm{d}\gamma \tag{5.10}$$

The source function S_{ν} is

$$S_{\nu} = -2m\nu^2 \frac{\int_{\gamma_{\min}}^{\gamma_{\max}} F(x) n_{\mathrm{e}}(\gamma) \mathrm{d}\gamma}{\int_{\gamma_{\min}}^{\gamma_{\max}} \gamma^2 F(x) \frac{\mathrm{d}}{\mathrm{d}\gamma} \left(\frac{n_{\mathrm{e}}(\gamma)}{\gamma^2} \right) \mathrm{d}\gamma} \tag{5.11}$$

In the monoenergetic approximation, the source function simplifies to

$$S_{\nu} = m\nu_0 \frac{\gamma^5 F(x)}{K_{5/3}(x)} \tag{5.12}$$

(see Chapter 4)

The synchrotron photons, while inside the source, are being repeated scattered by the energetic electrons to higher energies. Appointing i as the number of times a photon is scattered, the rate of scattering of the $(i-1)^{th}$ generation of photons into the frequency interval $\mathrm{d}\nu_i$ by a single electron, as defined in Eq. (4) of [GKM01], is

$$\left(\frac{\mathrm{d}n_{\mathrm{ph}}}{\mathrm{d}t \mathrm{d}\nu_i} \right)_{\mathrm{sp}} = \frac{3\sigma_{\mathrm{T}} c}{4\nu_{i-1}\gamma^2} f(y) \tag{5.13}$$

for a radiation field of 1 photon per unit volume. Rybicki and Lightman (1979) [RL79, Chapter 7] assumed that scattering in the rest frame of the electron is isotropic, and obtained $f_{\mathrm{iso}}(y) = 2(1-y)/3$. Here, we include the Klein-Nishina effects and assumes that the target photons are coming from the direction opposite to the electron velocity [GKM01], in which case,

$$
\begin{aligned}
f(y) &= \left[2\,y\ln y + y + 1 - 2y^2 + \frac{(4\epsilon_{i-1}\gamma\,y)^2(1-y)}{2(1+4\epsilon_{i-1}\gamma\,y)} \right] P(1/4\gamma^2, 1, y), \quad (5.14) \\
y &= \frac{\epsilon_i}{4\epsilon_{i-1}\gamma^2(1-\epsilon_i/\gamma)} \quad (5.15)
\end{aligned}
$$

where ϵ_{i-1} and ϵ_i are the energy of the target photons and scattered photon in units of mc^2 respectively, and $P(1/4\gamma^2, 1, y) = 1$ for $1/4\gamma^2 \leq y \leq 1$ and zero otherwise.

Assuming spherical symmetry in the distribution of electrons, the rate of scattering of photons with energy $h\nu_{i-1}$ to energy $h\nu_i$, in the observer's frame, from a uniform distribution of electrons with differential number density n_{e} can be found by integrating over the electron energy distribution,

$$
\left(\frac{\mathrm{d}n_{\mathrm{ph}}}{\mathrm{d}t\mathrm{d}\nu_i} \right) = \frac{4\pi}{3} \left(\frac{R}{2} \right)^3 \int_0^\infty \mathrm{d}\gamma\, n_{\mathrm{e}} \left(\frac{\mathrm{d}n_{\mathrm{ph}}}{\mathrm{d}t\mathrm{d}\nu_i} \right)_{\mathrm{sp}} \quad (5.16)
$$

Note that we divide R (the linear size of the source) by 2 to obtain the source radius.

The specific intensity of the ith generation photons is then simply the scattering rate of the electron distribution for one photon in a unit volume in Eq. (5.16), integrated over the seed photon number density,

$$
\begin{aligned}
I_{\nu_i}^{(\mathrm{C})} &= \left(\frac{\mathrm{d}E}{\mathrm{d}t\mathrm{d}\nu_i\mathrm{d}r^2\mathrm{d}\Omega} \right) \\
&= \frac{4\pi}{c} \int_0^\infty \mathrm{d}\nu_{i-1} \frac{\zeta I_{\nu_{i-1}}}{h\nu_{i-1}} \left(\frac{\mathrm{d}n_{\mathrm{ph}}}{\mathrm{d}t\mathrm{d}\nu_i} \right) \frac{h\nu_i}{4\pi(R/2)^2} \quad (5.17)
\end{aligned}
$$

where ζ is a factor close to unity which arises from the geometry of the source (see Chapter 4), and $I_{\nu_{i-1}}$ is the specific intensity from the $i-1$ generation of photons — e.g. to compute the first generation of scattered photons $i = 1$, $I_{\nu_0} = I_\nu^{(\mathrm{S})}$.

For a roughly spherical source, the geometric factor $\zeta = 2/3$, as shown in Chapter 4 [TK06],

$$
I_{\nu_i}^{(\mathrm{C})} = \frac{4\pi}{3} R\sigma_{\mathrm{T}}\nu_i \int_0^\infty \frac{\mathrm{d}\gamma}{\gamma^2} n_{\mathrm{e}} \int_0^\infty \frac{\mathrm{d}\nu_{i-1}}{\nu_{i-1}^2} I_{\nu_{i-1}} f(y) \quad (5.18)
$$
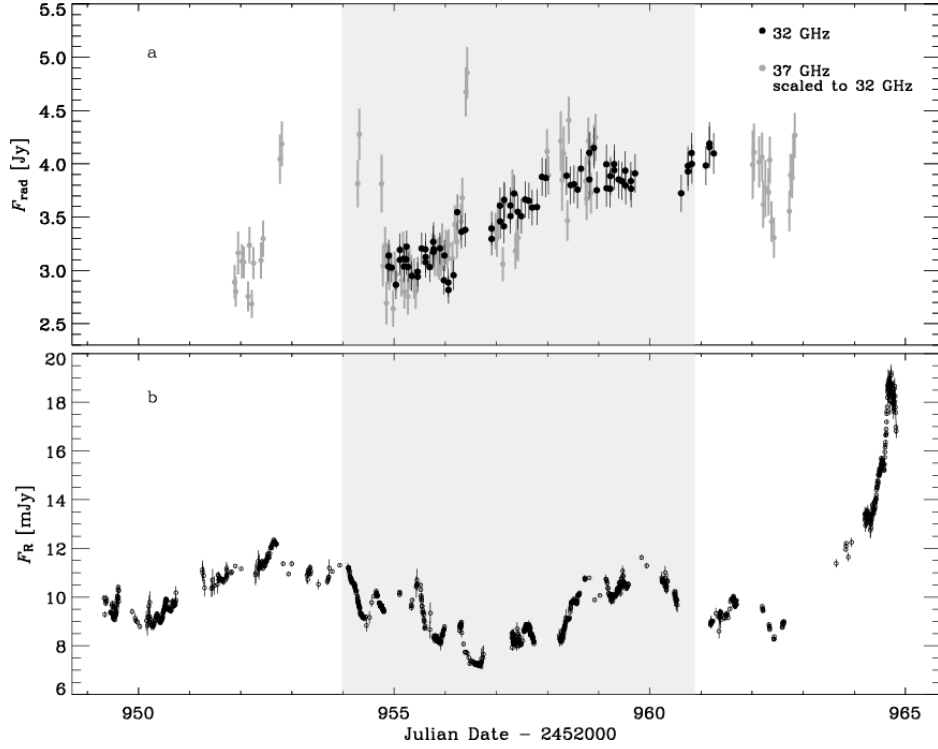
Figure 5.2: Radio and optical light curve of S5 0716+714 measured during the campaign of Ostorero et al. in November 2003. Panel a: 32 GHz radio light curve and 37 GHz radio light curve scaled by a factor $\langle F_{32\text{GHz}}/F_{37\text{GHz}} \rangle = 0.89$. Panel b: R-band optical light curve. Shaded region indicates the period of INTEGRAL pointing. [OWG⁺06]

For a monoenergetic electron distribution, this expression can be simplified to

$$I_{\nu_i}^{(C)} = \frac{4\pi}{3} \tau_{\text{T}} \frac{\nu_i}{\gamma^2} \int_0^\infty \frac{d\nu_{i-1}}{\nu_{i-1}^2} I_{\nu_{i-1}} f(y) \tag{5.19}$$

Eqs. (5.19) and (5.18) are integrated numerically for monoenergetic electrons and for an electron distribution given by Eqs. (5.7) and (5.8), respectively.

5.3 The BL Lac object S5 0716+714

Past observations of S5 0716+714 have shown that the source exhibits intra-day variability in the radio and optical bands [e.g. GVR⁺97, RVT⁺03]. Correlation between radio (at 5 GHz) and optical (at 650nm) variability suggest that scintillation, a process which is frequency dependent and not effective at optical frequencies, does not play a large part in the observed variability [WWH⁺96, Wag01, and Fig. 3.2 in Chapter 3]. More recent multi-frequency studies of S5 0716+714 by [OWG⁺06] have

obtained simultaneous measurements from radio to optical frequencies during the IN-
TEGRAL pointing period, and the non-detection of the source by INTEGRAL has
provided upper limits at X-ray frequencies. Shown in Fig. 5.2 is the light curve of
S5 0716+714 during the campaign of Ostorero et al. in November 2003. The 32 and 37
GHz measurements are shown in the upper panel, where the flux measured at 37 GHz is
normalised to the flux measured at 32 GHz. Flux variations are clearly displayed at 32
and 37 GHz, and the flux at the two radio frequency can be seen to rise to a maximum
over a period of $\Delta t \approx 4.1$ days. The lower panel shows the optical light curve in the
R-band during the same period, but unlike previous observation of the same source by
Wagner et al (1996) (see Fig. 3.2 in Chapter 3), it does not appear to be correlated
to the variations at the radio frequencies. Since inter stellar scintillation is inefficient
at 32 and 37 GHz, the observed variability was assumed to be intrinsic. Assuming
$H_0 = 70 \, \mathrm{km \, sec^{-1} \, Mpc^{-1}}$, with $\Omega_\lambda = 0.7$, $\Omega_M = 0.3$ and $\Omega_k = 0$, and a redshift $z > 0.3$
based on the non-detection of a host galaxy [e.g. QWW$^+$91, WWH$^+$96], a variability
brightness temperature of $T_{var} > (2.1 \pm 0.1) \times 10^{14}$ K was deduced.

Bach et al (2005) [BKR$^+$05] analysed the data set of VLBI images of 11 jet
components of S5 0716+714 at 4.9 GHz, 8.4 GHz, 15.3 GHz and 22.2 GHz, observed
between 1992 and 2001. Assuming that all the jet components move with the same
speed along the jet (i.e. all components have the same Lorentz factor), they proposed
that the observed large range (from $5.5c$ to $16.1c$) of apparent component speeds is due
to variations of the viewing angle, and limit the Lorentz factor and the viewing angle
of the VLBI jet to $\Gamma > 15$ and $\theta < 2°$, respectively. Under these conditions, the range
of Doppler factors would be $\mathcal{D} \approx 20 - 30$. Such high Doppler factors may be the key
to explain the observed high brightness temperature.

During the campaign of Ostorero et al (2006) [OWG$^+$06], observations of S5 0716+714
between 5 GHz and 32 GHz were best fitted with spectral indices α_{5-32} of $+0.3$ and
$+0.5$ at two different epochs. These observations are interpreted as optically thick syn-
chrotron emission from an inhomogeneous source, with the self absorption frequency
at $\nu_{abs} \approx 10^{13}$ Hz. In the near infrared to optical band, observations from $2001-2004$,
reported by Hagen-Thorn et al (2006) [HLE$^+$06], showed that the spectral energy dis-
tribution between the frequencies $\nu_K = 1.38 \times 10^{14}$ Hz and $\nu_B = 6.81 \times 10^{14}$ Hz can be

fitted by the power law $F_\nu \propto \nu^{-1.12}$.

We apply the model in which the radiating electrons are monoenergetic, and the model in which the radiating electrons are the stationary distribution results from the cooling of an injection of double power-law distribution, to S5 0716+714. We adopt the lower limit of the red-shift at $z = 0.3$, and a linear size inferred by the variability time scale of the source, $\Delta t = 4.1$ days, such that $R = c\Delta t\mathcal{D}/(1 + z)$. The values of the parameters can be found in Table 5.1, which include both parameters which value we specify, and parameters which values are computed from the specified parameters. The spectra predicted by the two models are shown in Fig. 5.3 and Fig. 5.4, which are discussed separately in the next two subsections.

One of the calculated quantity is an estimate of the jet power − the power that the host galaxy must provide in the jet in order to produce such compact radio sources as described by our models, at the observed frequency of occurrence. We estimate the jet power by first computing the total energy content of the source (the magnetic field and the particle energy densities integrated over the volume of the source), and then dividing this quantity by the average time lag between the occurrence of two consecutive radio blobs. In the co-moving frame of the source, for monoenergetic electrons, the total energy content is

$$E'_{\text{blob}} = \left(\frac{B^2}{8\pi} + N'_{\text{e}}\gamma mc^2 \right) R'^3 \tag{5.20}$$

and for power-law electrons,

$$E'_{\text{blob}} = \left(\frac{B^2}{8\pi} + \int_{\gamma_{\text{min}}}^{\gamma_{\text{max}}} n'_{\text{e}}(\gamma)\gamma mc^2 \mathrm{d}\gamma \right) R'^3 \tag{5.21}$$

For a source moving with a speed βc with respect to the host galaxy, the bulk Lorentz factor of the source is $\Gamma = \sqrt{1 - \beta^2}$, and the Doppler boosting factor as seen by a distant observer, at an angle ϕ with respect to the source velocity, is $\mathcal{D} = \sqrt{1 - \beta^2}/(1 - \beta\cos\phi)$.

Spatial volume element transform as $\mathrm{d}^3\mathbf{r} = \Gamma^{-1}\mathrm{d}^3\mathbf{r}'$, whereas momentum volume element transform as $\mathrm{d}^3\mathbf{p} = \Gamma\mathrm{d}^3\mathbf{p}'$. Therefore, an element of phase space $\mathrm{d}\mathcal{V}' = \mathrm{d}^3\mathbf{p}'\mathrm{d}^3\mathbf{r}'$ occupied by a number of particles, $\mathrm{d}N_{\text{total}}$, is a Lorentz invariant. Since the number of particles within a phase space volume is invariant, the phase space electron density is dimensionally $\mathrm{d}N_{\text{total}}/\mathrm{d}\mathcal{V}$, is also a Lorentz invariant, $n'_{\text{e}}(\gamma) = n_{\text{e}}(\gamma)$. In the

rest frame of the galaxy, the spatial transformation in the direction along the jet axis leads to $R^3 = \Gamma R'^3$, and $E_{\text{blob}} = \Gamma E'_{\text{blob}}$.

In the rest frame of the host galaxy, the jet power

$$P_{\text{jet}} = \frac{E_{\text{blob}}}{\Delta t_{\text{occ}}} \tag{5.22}$$

where Δt_{occ} is the average time lag between the occurrence of each blob. Linear fits of the change in position of the 11 jet components [BKR$^+$05] suggest that the time lag between the occurrence of a two components is between $0.1 - 1.8$ years. The estimate of E_{blob} is the lower limit of the total energy in the blob, since it is reasonable to assume that the source looses energy over time. We, therefore, adopt an upper limit of $\Delta t_{\text{occ}} = 1.8$ years to allows us to estimate the lower limits of the jet power of each model, which are listed in Table 5.1.

5.3.1   Monoenergetic electrons

In the monoenergetic model, the spectrum is specified by four parameters, ν_{abs}, ν_{p}, $\mathcal{D}$ and ξ, as well as z and Δt which are kept fixed for all models. ν_{abs} is determined by the first spectral break at ~ 4 GHz, and ν_{p} corresponds to the spectral cut-off. In Fig. 5.3, we compare two models in which one has a cut-off at $\sim 10^{11.5}$ Hz, and the other cuts off just before reaching the optical point. The Doppler factor $\mathcal{D}$ affects the level of the observed flux both by determining the linear size of the source in its rest frame and determining the amount of boosting the flux receives. ξ determines the ratio of the synchrotron flux to the inverse Compton flux, as well as the value of γ_{p}. Therefore, having ν_{abs} and ν_{p} determined, $\mathcal{D}$ and ξ must be adjusted to fit the observed flux, and to ensure the inverse Compton spectra do not exceed the INTEGRAL upper limits, while keeping $\mathcal{D}$ minimised.

Fig. 5.3 shows the simultaneous multi-frequency observation of S5 0716+714 from the study conducted by [OWG$^+$06]. Measurements are shown by black dots, variability range is shown by vertical bars between two points and upper limits are shown by downward arrows. Shown also are the spectra predicted by the model assuming electrons are monoenergetic. The Doppler boosting factor is $\mathcal{D} = 55$ in both models.

The solid lines show the synchrotron and inverse Compton spectra with the
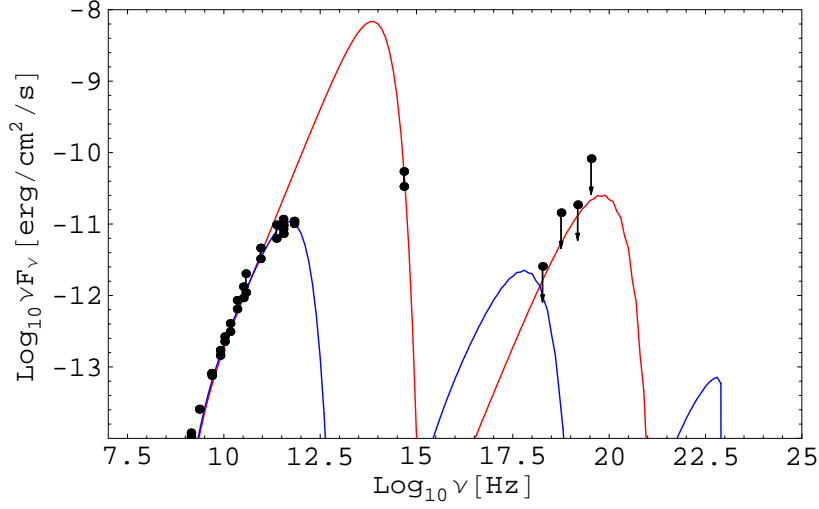
Figure 5.3: Spectral energy distribution of S5 0716 +714. Multi-frequency simultaneous data from Ostorero et al [OWG$^+$06] are shown as black symbols. Black dots show data points, variation ranges are shown by a vertical bar between two symbols, and downward arrows show upper limits. Values of the parameters are shown in Table 5.1. The model spectra are computed from a distribution of monoenergetic electrons, and are shown with red and blue line. The red line shows the model spectrum in which the parameters are chosen such that it goes through the data points at optical frequency, whereas the blue line shows the model spectrum in which the parameters are chosen to mimic the spectral break at $10^{11.5}$ Hz.The values of the parameters are shown in Table 5.1.

synchrotron self-absorbed frequency again set to $\nu_{\mathrm{abs}} = 3.9$ GHz and peaking at $\nu_{\mathrm{p}} = 300$ GHz, the values of other parameters are shown in Table 5.1. The brightness temperature at $\nu_{\mathrm{obs}} = 32$ GHz is $T_{\mathrm{B}} = 3.9 \times 10^{12}$ K ($T_{\mathrm{B}} = c^2 F_\nu/(2k_{\mathrm{B}}\nu^2\theta_{\mathrm{d}}^2)$, where k_{B} is the Boltmann constant and θ_{d} is the angular diameter of the source). The synchrotron spectrum shows good agreement with the data points at radio frequencies. The first order inverse Compton spectrum gives emission at the X-ray frequencies and the second order spectrum gives gamma-ray emission of up to ~ 40 MeV, emission from higher orders scattering is negligible due to the Klein-Nishina effect.

Dashed lines represent the synchrotron and inverse Compton spectra produced by monoenergetic electrons, with $\nu_{\mathrm{abs}} = 3.9$ GHz, $\nu_{\mathrm{p}} = 55 \times 10^{12}$ Hz, the values of other parameters can be found in Table 5.1. This gives a brightness temperature of $T_{\mathrm{B}} = 3.7 \times 10^{12}$ K at an observing frequency of $\nu_{\mathrm{obs}} = 32$ GHz. The synchrotron spectrum gives a reasonable fit at radio frequencies up to $\sim 10^{11.5}$ Hz and extends all

the way to the optical frequencies. The first order inverse Compton spectrum gives emission in hard X-ray, and the second order inverse Compton spectrum is greatly affected by the Klein-Nishina effect and therefore very little gamma ray emission is produced.

The spectral break at $10^{11.5}$ Hz is well fitted by the model shown by the solid line. We are unable to obtain a set of parameters which would allow the first inverse Compton spectrum to reproduce the optical data. However, simple qualitative analysis shows that to mimic the optical data points with the first inverse Compton spectrum is not possible. The level of flux the first inverse Compton spectrum will require in order to reach the optical data will be much higher than the synchrotron flux (i.e. $\xi \gg 1$), which is likely to require a large γ resulting in the spectrum extending to frequency far beyond the optical band. The first inverse Compton spectrum is therefore likely to contradict the INTEGRAL upper limits, and the very high X- and γ-ray flux is likely to give rise to high "compactness" ($\propto \gamma$-ray photon energy density) implying high rate of electron-positron pair production by photon-photon interaction.

Attempts to include the optical data into the synchrotron spectrum proved to be inconsistent with data and also contradictory to the key assumption of monoenergetic electrons, as shown by the dashed spectrum and Table 5.1. The predicted (dashed) spectrum fails to account for the spectral break at $\nu \sim 10^{11.5}$ Hz, and predicts a very high flux at $\nu \sim 10^{14}$ Hz. Although there are no simultaneous data available at this frequency, historical data suggests that variations rarely exceed 1 order of magnitude, it is unlikely that the flux at 10^{14} Hz would exceed the historical data by 3 orders of magnitude. Quantitative examination of the model parameters also reveal that the Lorentz factor of the dashed spectrum is higher than γ_{cool}, implying that the particles will lose a significant portion of their energy by synchrotron radiation before they vacate the source, and so the electron spectrum will evolve to one which is proportional to γ^{-2}. This set of parameters therefore violate the monoenergetic assumption, and the dashed spectrum is rejected. In order to reproduce the observed optical emission, we incorporate a power law component in the electron spectrum at $\gamma > \gamma_{\text{p}}$, which emits synchrotron radiation at frequency beyond ν_{p}.
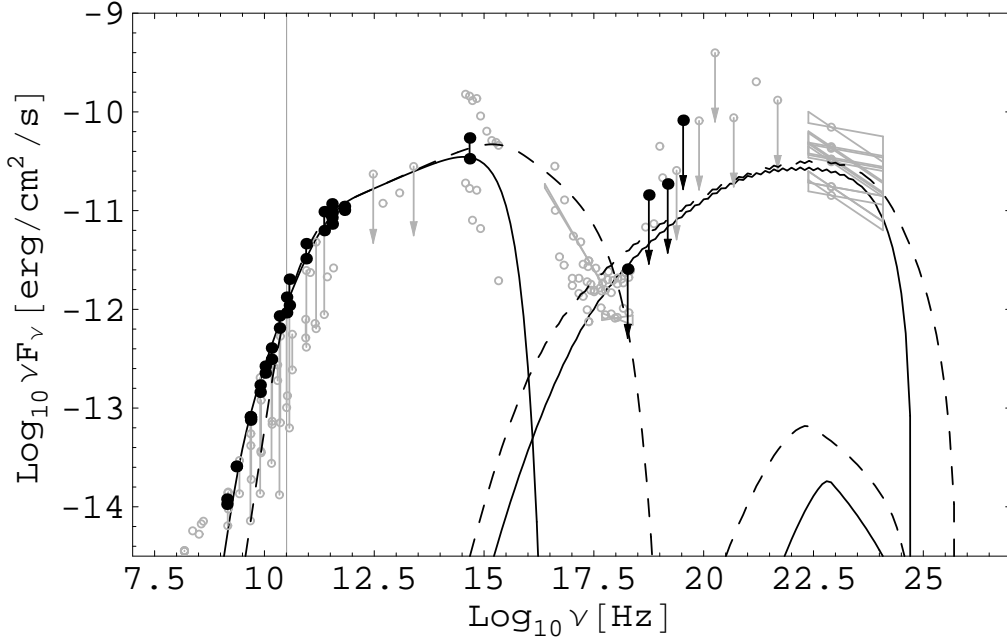
Figure 5.4: The spectral energy distribution of S5 0716 +714, as represented in Fig. 5.3. The model spectra, shown as solid and dashed lines, are computed from a quasi-monoenergetic electron distribution in the form of Eq. (5.7). The dashed line represents the model in which the Doppler boosting factor is minimised, whereas the solid line shows the model in which the values of the parameters are chosen to account for all radio and optical data points. Dashed gridline shows the position of 32 GHz. The values of the parameters are shown in Table 5.1. Historical data, shown as grey symbols, at the wavelengths of 1.38, 2.7, 3.9, 7.7, 13 and 31 cm are from RATAN-600; other radio to optical frequencies data from [KWPN81, WJS+81, EPW+82, Per82, PFJ82, LRL+85, SSN+87, KS90, MKC+90, HMWB91, KWG+93, GSH+94, HWRW95, DBB+96, RTd+97, ZZC+97, RWR99, CLC+02, RVT+03]; UV data from [PT93, GVR+97]; X-ray data from [BSP+92, CFGM97, KTM+98, GMC+99, TRG+03, PFB+05]; and γ-ray data from [MJJ+95, HBB+99, Col06].

5.3.2 Double power-law injection

Inspection of the blue line spectrum in Fig. 5.3 shows that emission in the frequency range where the INTEGRAL upper limits reside corresponds to first inverse Compton scattering of synchrotron photons at ν_p. Therefore, for the purpose of manipulating the level of flux at the INTEGRAL frequencies, we introduce a fictitious parameter r_p, which determines the ratio of the level of flux between ν_p and $\gamma^2 \nu_p$. The normalisation constant in the double power-law injection spectrum, Q_0 is eliminated
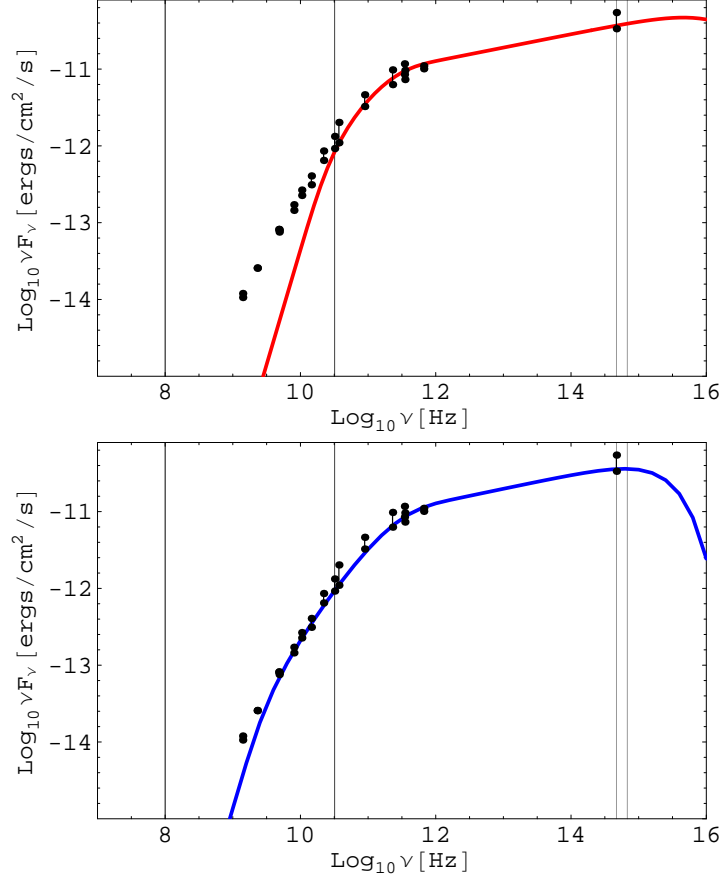
Figure 5.5: The spectral energy distribution of S5 0716 +714 and the model spectra, as represented in Fig. 5.3, in radio to optical band. Top panel shows the model in which the Doppler boosting factor is minimised. Bottom panel shows the model in which the values of the parameters are chosen to account for all radio and optical data points.

in favour of the parameter r_p

$$r_\mathrm{p} = \frac{4}{3}\gamma_\mathrm{p}^2 R\sigma_\mathrm{T} \int_0^\infty n_\mathrm{e}(\gamma)\mathrm{d}\gamma \qquad (5.23)$$

where the integral is evaluated according to Eqs. (5.7) and (5.8). In the monoenergetic limit, r_p is equivalent to ξ. We are, therefore, able to use the simpler monoenergetic model to estimate the required values of r_p, $\mathcal{D}$ and ν_cool by specifying ν_abs and ν_p, as described in the previous subsection.

In Figs. 5.4 and 5.5, shown as dashed line, we attempt to minimise the Doppler factor of the source. Since according to Wagner et al [WWH+96] and [OWG+06], the variability displayed by S5 0716+714 is intrinsic, and the variability time $\Delta t = 4.1$

days was measured at 32 GHz and 37 GHz, we require the model spectrum to be in agreement with the data at these two frequencies. We are unaware of variability measurement at lower frequencies of the simultaneous observation, therefore we allow the model spectrum to deviate from the data at frequencies below 32 GHz. At the expense of having a lower than the observed level of flux below 32 GHz, we find that the minimum Doppler factor required is $\mathcal{D} = 30$.

The power law indices of the injection spectrum used to generate spectrum shown by the dashed line are $s_1 = 2$ for the low energy part, such that electrons with $\gamma < \gamma_p$ do not contribute significantly to the synchrotron emission, and $s_2 = -2.60$, chosen purely for the construction of the spectral shape from the far infrared to optical band. The rest of the parameters are varied while keeping the Doppler boosting factor fixed. To find the limiting case, we have chosen the self absorption frequency to be $\nu_{abs} = 32$ GHz, and found that the minimum Doppler factor which can generate a high enough level of flux at 32 GHz and beyond to be $\mathcal{D} = 30$.

To meet the above criteria, the best fitting is found with $\gamma_p = 244$ and $\gamma_{cool} = 7.85 \times 10^4$, the values of the other parameters can be found in Table 5.1. At the observing frequency of 32 GHz, the brightness temperature in the frame of the observer is $T_B = 1.4 \times 10^{13}$ K. The frequency at which the synchrotron spectrum cuts off does not affect the spectral shape at low frequencies. However, $\nu_{max} = \mathcal{D}/(1 + z) \times \nu_0 \gamma_{max}^2$ is constrained by the optical data, which impose a lower limit on ν_{max}, and the non-detection by INTEGRAL, which impose an upper limit on ν_{max}. The maximum value is shown by the dashed line, where $\nu_{max} = 10^{18}$ Hz. This translates to $\gamma_{max} = 5.45 \times 10^5$ with $\mathcal{D} = 30$ and $z = 0.3$. It should be noted that the value of γ_{max} is a function of the Doppler factor, therefore, for the same value of ν_{max}, γ_{max} can be smaller for larger $\mathcal{D}$.

The model spectrum represented by the dashed line shows that it is possible to interpret the observed variability at 32 GHz and 37 GHz as coming from one of the jet components with the kinematics described by Bach et al [BKR$^+$05]. That would require the lower frequency emission to originates from a bigger source region than that inferred from the observed variability at $\nu \geq 32$ GHz.

The solid line in Figs. 5.4 and 5.5 shows the model spectrum in which we assume emissions at all frequencies originate from the same region, as suggested by the corre-

lation between the variability at 5 GHz and 650 nm [WWH$^+$96]. We achieve this by requiring the model spectrum to agree with all the data points from radio to optical frequency, assuming a source size inferred from variability measured at 32 GHz and 37 GHz.

The values of the parameters are chosen such that all radio points are fitted. The Comptonisation parameter ξ must be kept low enough such that the inverse Compton spectra are below the upper limits. This is achieved at the expense of having high Doppler factor, at $\mathcal{D} = 65$. The spectral indices of the injection spectrum are $s_1 = 2$, $s_2 = -2.61$, peaking at $\gamma_{\mathrm{p}} = 696$. Radiative cooling sets in at $\gamma_{\mathrm{cool}} = 6.19 \times 10^6$, and $\xi = 10^{-1.14}$. The brightness temperature at 32 GHz is $T_{\mathrm{B}} = 2.5 \times 10^{12}$ K. We also show here the minimum value of ν_{max} which is just high enough to reach the optical points, and this is found to be equal to $\nu_{\mathrm{max}} = 1.5 \times 10^{15}$ Hz ($\gamma_{\mathrm{max}} = 5.19 \times 10^4$).

In this case, we show that if the emission at all frequencies originates from the same source region, it must be beamed at a much higher Doppler factor than that proposed for the jet components by Bach et al [BKR$^+$05], suggesting that the source moves at a higher speed than the jet or closer to the line of sight. Alternatively, the jet components may not all have the same speed, and the large range of superluminal motion could be a result of variations in speed.

Parameters	Mono (red)	Mono (blue)	Power-law (dashed)	Power-law (solid)
z	0.3	0.3	0.3	0.3
Δt (days)	4.1	4.1	4.1	4.1
$\mathcal{D}$	55	55	30	65
$\nu_{\rm p}$ (Hz)	5.5×10^{13}	3.9×10^{11}	2.0×10^{11}	2.7×10^{11}
$\nu_{\rm cool}$ (Hz)	1.74×10^{12}	1.17×10^{19}	2.07×10^{16}	2.14×10^{19}
$\nu_{\rm max}$ (Hz)	$-$	$-$	1.0×10^{18}	1.5×10^{15}
ξ	$10^{-2.5}$	$10^{-0.75}$	0.93	0.86
R (pc)	0.15	0.15	0.08	0.17
$\theta_{\rm d}$ (μas)	32.5	32.5	17.7	38.4
$\gamma_{\rm p}$	691	800	244	696
$\gamma_{\rm cool}$	123	4.39×10^{6}	7.85×10^{4}	6.19×10^{6}
$\gamma_{\rm max}$	$-$	$-$	5.45×10^{5}	5.19×10^{4}
$N_{\rm e}$ (cm^{-3})	0.02	0.70	3.15	0.32
B (mG)	648	3.43	34.7	2.65
$U_{\rm B}/U_{\rm par}$	1.8×10^{3}	1.0×10^{-3}	0.04	8.4×10^{-4}
$T_{\rm B}$ (K)	3.7×10^{12}	3.9×10^{12}	1.4×10^{13}	2.5×10^{12}
$\tau_{\rm T}$	6×10^{-9}	2×10^{-7}	5×10^{-7}	1×10^{-7}
$P_{\rm jet}$ (ergs/s)	1×10^{45}	3×10^{43}	5×10^{42}	4×10^{43}

Table 5.1: Values of the parameters used in the monoenergetic model and the double power-law injection model, shown in Figs. 5.3 and 5.4. $\theta_{\rm d}$ is the angular diameter of the source at its rest frame, $U_{\rm par}$ is the energy density of the particles and $P_{\rm jet}$ is the jet power in the rest frame of the host galaxy, predicted by each model. From z to ξ (monoenergetic) or $\nu_{\rm max}$ (power-law) are parameters we specify for the computation of the spectra, which are constrained by observations. From ξ (power-law) or R (monoenergetic) to $P_{\rm jet}$ are secondary parameters calculated from the first set of parameters. The compactness of all four models are negligibly small and is therefore not included in the discussion.

Chapter 6

Circular Polarisation of Monoenergetic Electrons

In Chapter 4, we have examined the parameters of the monoenergetic model which determine the brightness temperature of a compact synchrotron source. We have found that synchrotron emission can be partially circularly polarised, although the degree of polarisation is small. Early studies of synchrotron absorption, e.g. Ginzburg and Syrovatskii (1965) [GS65], have not included polarisation dependent absorption processes, while Legg and Westfold (1968) [LW68] studied the polarised intensities of synchrotron emission but without considering the corresponding absorption processes. Sazonov (1968) first treated the radiative transport equation for synchrotron emission to include the relevant absorption processes as well as Faraday conversion and rotation, which he discussed qualitatively in [Saz69b].

The polarised dissipative absorption processes act to reduce the intensity of the corresponding polarised emission. Whereas the Faraday effects are non-dissipative, and act only to change the polarisation properties of the emission. Faraday rotation apply to elliptically polarised waves in a medium in which the natural modes are circularly polarised, where the polarisation plane of the linearly polarised component rotates as the waves propagates due to the difference in speed between which the two circularly polarised components propagate. Faraday conversion apply in a medium in which the natural modes are linearly polarised. Linear polarisation is converted into circular as the two linearly polarised components propagate at different speeds, which results in a phase shift.

More detailed theoretical studies of circular polarisation in synchrotron emission have been carried out by e.g. Pacholczyk and Swihart (1974) [PS74] and Jones and

O'Dell (1977)[JO77]. Following from the study by Jones and O'Dell (1977) in [JO77], in which they assumed a power-law distribution of electrons, and claimed that circular polarisation changes sign just below the self-absorption frequency in the presence of Faraday rotation and conversion, we examine and evaluate the polarisation properties of synchrotron emission from monoenergetic electrons in this chapter.

6.1   The polarised synchrotron emission and absorption

The electric field $\mathbf{E}$ from a charged particle can be decomposed into two components, perpendicular to each other, in the direction $\mathbf{e}^1$ and $\mathbf{e}^2$ [see e.g. Jac75], for example, in the form of

$$E_x = E_{0x} \cos\left[(kz - \omega t) + \delta_x\right] \tag{6.1}$$

$$E_y = E_{0y} \cos\left[(kz - \omega t) + \delta_y\right] \tag{6.2}$$

where we adopt $\mathbf{e}^1$ to be the x direction, $\mathbf{e}^2$ to be the y direction, with the wave propagates in the z direction, E_{0x} and E_{0y} are the normalisation constants of the electric field in the x and y direction, respectively, k is the wave number, ω is the frequency of oscillation, δ_x and δ_y are the phase shifts in the x and y direction, respectively.

The polarised intensity of the electric field $\mathbf{E}$ described by Eqs. (6.1) and (6.2) can be represented as the polarisation tensor $\mathbf{P}$,

$$\mathbf{P} = \begin{pmatrix} \langle E_{0x}^2 \rangle & \langle E_{0x}E_{0y}(\cos\delta - i\sin\delta) \rangle \\ \langle E_{0x}E_{0y}(\cos\delta + i\sin\delta) \rangle & \langle E_{0y}^2 \rangle \end{pmatrix} \tag{6.3}$$

where $\delta = \delta_y - \delta_x$, and $<>$ denotes an average over time.

Similarly, the synchrotron specific intensity can be described by the polarisation tensor, $P^{\alpha,\beta}$. Since synchrotron radiation is highly (linearly) polarised, it is commonly treated only in the two natural modes, P^{11} and P^{22}, where we consider the two natural modes to have polarisation vectors $\mathbf{e}^1$ and $\mathbf{e}^2$. When considering the polarisation properties of synchrotron emission, the cross-correlation functions, $P^{12} = (P^{21})^*$, which contain information about the relative phase of the components in the two modes, must also be taken into account.

For the computation of the transfer of radiation, we adopt the more practical Stokes parameters instead of the polarisation tensor. Choosing $\mathbf{e}^1$ and $\mathbf{e}^2$ to be real,

the Stokes parameters are defined as

$$P^{\alpha,\beta} = \frac{1}{2} \begin{pmatrix} I+Q & U-iV \\ U+iV & I-Q \end{pmatrix} \tag{6.4}$$

The polarisation properties are contained in the Stokes parameters, where the degree of linear polarisation r_{L} and the degree of circular polarisation r_{C} are

$$r_{\mathrm{L}} = \frac{(Q^2+U^2)^{1/2}}{I} \ , \quad r_{\mathrm{C}} = \frac{V}{I} \tag{6.5}$$

The Stokes parameters can be understood as I being the total (unpolarised) intensity, $\pm Q$ being the linearly polarised intensity in the $\mathbf{e}^{(1,2)}$ direction, $\pm U$ being the linearly polarised intensity in a direction at an angle $\pi/4$ to $\mathbf{e}^{(1,2)}$ and $\pm V$ being the left and right handed circular polarisation.

The four components of the synchrotron emissivity, corresponding to the four Stokes parameters, from a homogeneous distribution of monoenergetic electrons or Lorentz factor γ and number density N_{e}, embedded in a uniform magnetic field B, are given in Legg and Westfold (1968) [LW68], and can be written in our notation as

$$J_I = \frac{\sqrt{3}}{2}\alpha_{\mathrm{f}} N_{\mathrm{e}} h\nu_{\mathrm{L}} \sin\theta F(x) \tag{6.6}$$

$$J_Q = \frac{\sqrt{3}}{2}\alpha_{\mathrm{f}} N_{\mathrm{e}} h\nu_{\mathrm{L}} \sin\theta x K_{2/3}(x) \tag{6.7}$$

$$J_V = \frac{4}{\sqrt{3}}\alpha_{\mathrm{f}} N_{\mathrm{e}} \frac{\cot\theta}{\gamma} h\nu_{\mathrm{L}} \sin\theta \left\{ xK_{1/3}(x) + \frac{2}{x}\left[xK_{2/3}(x) - \frac{F(x)}{2} \right] \right\} \tag{6.8}$$

where α_{f} is the fine structure constant, θ is the angle between the magnetic field direction and the line of sight, $\nu_{\mathrm{L}} = eB/(2\pi m)$ is the Larmor frequency, $K_n(x)$ is a modified Bessel function, $F(x) = x \int_x^\infty K_{5/3}(t)\mathrm{d}t$, with $x = 2\nu/(3\nu_{\mathrm{L}}\gamma^2 \sin\theta)$. In a homogeneous medium, a suitable choice of coordinates allows all $U-$components of the emissivity, as well as absorption, conversion and rotation to be 0.

6.2 Absorption, conversion and rotation

The polarised absorption can be constructed from the polarised emission using Eq. (1.12) in the form

$$\alpha_{I,Q,U,V} = -\frac{c^2}{8\pi}\int_0^\infty \frac{J_{I,Q,U,V}}{N_{\mathrm{e}}mc^2}\gamma^2 \frac{\mathrm{d}}{\mathrm{d}\gamma}\left(\frac{n_{\mathrm{e}}(\gamma)}{\gamma^2} \right) \mathrm{d}\gamma, \tag{6.9}$$

where for monoenergetic electrons of Lorentz factor γ_p, $n_e(\gamma) = N_e \delta(\gamma - \gamma_p)$, the coefficient of the polarised absorption $\alpha_U = 0$. Substituting the emissivity J_A (A=I, Q, U, V) in Eq. (6.9) with Eqs. (6.6) (6.7) and (6.8), we obtain

$$\alpha_I = \frac{1}{2\sqrt{3}} \frac{\sigma_T}{\alpha_f} \frac{N_e mc^2}{h\nu_L} \frac{K_{5/3}(x)}{\gamma^5 \sin\theta} \tag{6.10}$$

$$\alpha_Q = \frac{1}{4\sqrt{3}} \frac{\sigma_T}{\alpha_f} \frac{N_e mc^2}{h\nu_L} \frac{\left(K_{1/3}(x) + K_{5/3}(x)\right)}{\gamma^5 \sin\theta} \tag{6.11}$$

$$\alpha_V = \frac{1}{3\sqrt{3}} \frac{\sigma_T}{\alpha_f} \frac{N_e mc^2}{h\nu_L} \frac{\cot\theta}{\gamma^6 \sin\theta} \frac{1}{x^2}$$
$$\times \left[x K_{1/3}(x) + \left(2 + x^2\right) K_{2/3}(x) + x^2 K_{4/3}(x) - \frac{F(x)}{x} \right] \tag{6.12}$$

The transfer coefficients corresponding to the transformation of polarisation as rotation of the polarisation ellipse (α_V^*) and as conversion between linear and circular polarisation ($\alpha_{(Q,U)}^*$) were discussed in [Saz69a]. In a homogeneous medium, rotation of the coordinates allow $\alpha_U^* = 0$. $\alpha_{(Q,V)}^*$ as derived by Sazonov [Saz69a] can be represented in our notations as

$$\alpha_Q^* = -\frac{3}{8} \frac{\sigma_T}{\alpha_f} \frac{mc^2}{h\nu} \frac{\nu_L \sin\theta}{\nu}$$
$$\times \int_0^\infty \left(\frac{3}{2}x\right)^{1/3} \gamma'^2 \frac{d}{d\gamma'} \left(\frac{n_e}{\gamma'^2}\right) d\gamma' \int_0^\infty z \cos\left[z \left(\frac{3x}{2}\right)^{2/3} + \frac{z^3}{3} \right] dz \tag{6.13}$$

$$\alpha_V^* = -\frac{3}{2} \frac{\sigma_T}{\alpha_f} \frac{mc^2}{h\nu} \frac{\nu_L \sin\theta}{\nu} \int_0^\infty \gamma' \ln\gamma' \left[\frac{\partial}{\partial\gamma'} + \frac{1}{2} \left(\frac{\partial^2}{\partial\gamma'\partial\theta} - \frac{1}{\gamma'} \frac{\partial}{\partial\theta} \right) \right] \left(\frac{n_e}{\gamma'^2}\right) d\gamma' \tag{6.14}$$

We approximate the integral over z in Eq. (6.13) as

$$\int_0^\infty z \cos\left(\frac{z^3}{3}\right) = \frac{\Gamma(2/3)}{24^{1/3}} = 0.469 \tag{6.15}$$

since for synchrotron radiation, emission and absorption decay very rapidly beyond $x = 1$, therefore, at any frequency (or equivalently x) $x \leq 1$, the first term in the square bracket of Eq. (6.13) is negligible compare to the second term. The second term in the square bracket on the right hand side of Eq. (6.14) equals zero in our case since, in the rest frame of the source, the electron distribution can be considered isotropic. For monoenergetic electrons where $n_e = N_e \delta(\gamma' - \gamma)$, Eqs. (6.13) and (6.14) become

$$\alpha_Q^* = \frac{9}{8} \frac{\Gamma(2/3)}{24^{1/3}} \frac{\sigma_T}{\alpha_f} \frac{N_e mc^2}{h\nu_L} \frac{1}{x^{5/3}\gamma^5 \sin\theta} \tag{6.16}$$

$$\alpha_V^* = \frac{2}{3} \frac{\sigma_T}{\alpha_f} \frac{N_e mc^2}{h\nu_L} \frac{\cot\theta}{\gamma^6 \sin\theta} \frac{(1 + \ln\gamma)}{x^2} \tag{6.17}$$

6.3 The transfer of radiation

The transfer equations for isotropic polarised synchrotron emission can be written in the form

$$\frac{\mathrm{d}}{\mathrm{d}r} S_\mathrm{A} = \frac{J_\mathrm{A}}{4\pi} - \mu_\mathrm{AB} S_\mathrm{B} + \mu^*_\mathrm{AB} S_\mathrm{B} \tag{6.18}$$

where r is the distance along the line of sight, J_A is the polarised emissivity as defined above, and $S_\mathrm{A,B}$ is the "Stokes vector", A,B $= 1,2,3,4$, with

$$S_1 = I_\nu, \ S_2 = Q_\nu, \ S_3 = U_\nu, \ S_4 = V_\nu \tag{6.19}$$

The matrices μ_AB and μ^*_AB describe the dissipative, which in this case is the polarised synchrotron self-absorption, and the non-dissipative, which includes Faraday conversion and rotation, transfer processes that affect the intensity and polarisation of the emission.

$$\mu_\mathrm{AB} = \begin{pmatrix} \alpha_I & \alpha_Q & \alpha_U & \alpha_V \\ \alpha_Q & \alpha_I & 0 & 0 \\ \alpha_U & 0 & \alpha_I & 0 \\ \alpha_V & 0 & 0 & \alpha_I \end{pmatrix}, \quad \mu^*_\mathrm{AB} = \begin{pmatrix} 0 & 0 & 0 & 0 \\ 0 & 0 & -\alpha^*_V & \alpha^*_U \\ 0 & \alpha^*_V & 0 & -\alpha^*_Q \\ 0 & -\alpha^*_U & \alpha^*_Q & 0 \end{pmatrix} \tag{6.20}$$

The Faraday effects can be understood as follow. Consider the non-dissipative transfer coefficient μ^*_AB in Eq. (6.20). The effects of the second row contributes to Q, third row to U and fourth row to V. Faraday rotation rotates the polarised intensity Q, and in doing so, transfer a fraction of α^*_V of Q into U. Faraday conversion convert a fraction of α^*_Q of the polarised intensity U into V, and a fraction of α^*_U of the polarised intensity V into Q.

Eq. (6.18) can be rewritten into a form which combines the two kinds of transfer processes, which can be normalised to a set of dimensionless coefficients,

$$\frac{\mathrm{d}}{\mathrm{d}\tau} \begin{pmatrix} I_\nu \\ Q_\nu \\ U_\nu \\ V_\nu \end{pmatrix} = \begin{pmatrix} 1 \\ \epsilon_Q \\ 0 \\ \epsilon_V \end{pmatrix} S_I - \begin{pmatrix} 1 & \xi_Q & 0 & \xi_V \\ \xi_Q & 1 & \xi^*_V & 0 \\ 0 & -\xi^*_V & 1 & \xi^*_Q \\ \xi_V & 0 & -\xi^*_Q & 1 \end{pmatrix} \begin{pmatrix} 1 \\ \pi_Q \\ \pi_U \\ \pi_V \end{pmatrix} I_\nu \tag{6.21}$$

where $\tau = \alpha_I r$, $\xi_{Q,V} = \alpha_{Q,V}/\alpha_I$, $\xi_{Q,V}^* = \alpha_{Q,V}^*/\alpha_I$, $\pi_{Q,U,V} = (Q,U,V)/I$, $\epsilon_{Q,V} = J_{Q,V}/J_I$ and $S_I = J_I/\alpha_I$.

The normalised coefficients not only simplify the computation of the transfer equation, but also provide direct comparisons of the relative strength between absorption, conversion and rotation . The parameters which are for our discussion include $(\pi_Q^2 + \pi_U^2)^{1/2} = \pi_L$, the degree of linear polarisation, $-\pi_V = \pi_C$, the degree of circular polarisation, and ξ_V^*, which determine the importance of Faraday rotation. In the strong-rotativity limit, $|\xi_V^*|\tau \gg 1$, Faraday rotation becomes an important absorption mechanisms. The normalised emission and transfer coefficients are

$$
\begin{aligned}
\epsilon_Q &= \frac{xK_{2/3}(x)}{F(x)} \\[2mm]
\epsilon_V &= \frac{8}{3}\frac{\cot\theta}{\gamma}\frac{-F(x) + x\left[2K_{2/3}(x) + xK_{1/3}(x)\right]}{xF(x)} \\[2mm]
\xi_Q &= \frac{1}{2}\left(\frac{K_{1/3}(x)}{K_{5/3}(x)} + 1\right) \\[2mm]
\xi_V &= \frac{2}{3}\frac{\cot\theta}{\gamma}\frac{x^2\left[K_{1/3}(x) + xK_{4/3}(x)\right] + xK_{2/3}(x)(2+x^2) - F(x)}{x^3K_{5/3}(x)} \\[2mm]
\xi_Q^* &= \frac{9\sqrt{3}}{4}\frac{0.469}{x^{5/3}K_{5/3}(x)} \\[2mm]
\xi_V^* &= \frac{4}{\sqrt{3}}\frac{1+\ln\gamma}{\gamma}\frac{\cot\theta}{x^2K_{5/3}(x)}
\end{aligned}
\tag{6.22}
$$

We approximate the normalised coefficients in two limiting cases − one where $x \ll 1$ and one where $x \gg 1$, to construct a hierarchy of the coefficients (with the exception of ξ_V^*),

$$
\xi_Q^* \rightarrow
\begin{cases}
1.28 + 0.48x^2 & ,x \ll 1 \\[1mm]
1.45x^{-7/6}e^x & ,x \gg 1
\end{cases}
$$

$$
\epsilon_Q \rightarrow
\begin{cases}
0.50 + 0.42x^{2/3} & ,x \ll 1 \\[1mm]
1.00 - 0.67x^{-1} + 1.44x^{-2} & ,x \gg 1
\end{cases}
$$

$$
\xi_Q \rightarrow
\begin{cases}
0.50 + 0.59x^{4/3} & ,x \ll 1 \\[1mm]
1.00 - 0.67x^{-1} + 0.78x^{-2} & ,x \gg 1
\end{cases}
$$

$$
\epsilon_V \rightarrow
\begin{cases}
2.09\cot\theta\gamma^{-1}x^{1/3} & ,x \ll 1 \\[1mm]
2.66\cot\theta\gamma^{-1}\left(1 + x^{-1}\right) & ,x \gg 1
\end{cases}
$$

$$\xi_V \rightarrow \begin{cases} 1.31 \cot\theta\gamma^{-1}x^{1/3} & , x \ll 1 \\ 1.33 \cot\theta\gamma^{-1}\left(1 + 0.50x^{-1}\right) & , x \gg 1 \end{cases}$$

$$\xi_V^* \rightarrow \begin{cases} 1.61 \cot\theta(1 + \ln\gamma)\gamma^{-1}x^{-1/3} & , x \ll 1 \\ 1.84 \cot\theta(1 + \ln\gamma)\gamma^{-1}x^{-3/2}\mathrm{e}^x & , x \gg 1 \end{cases} \quad (6.23)$$

For monoenergetic electrons with $\gamma \gg 1$ and assuming $\cot\theta = 1$, the hierarchy $\xi_Q^* > 1 > \epsilon_Q > \xi_Q \gg \epsilon_V > \xi_V$ holds for a wide range of frequency. ξ_V^* is an exception, which, for most values of x, $\xi_V^* \ll 1$. At $x \gg 1$, ξ_V^* increases very rapidly, but for $\gamma > 1$, ξ_V^* never exceeds ξ_Q^*, at very high frequencies, we have $\xi_Q^* > \xi_V^* \gg 1$. However, the corresponding absorption depth $\tau_\mathrm{s} \ll 1$ at very high frrequencies, therefore the rotation depth $\xi_V^*\tau_\mathrm{s}$ is negligible. At $x \ll 1$, $\xi_V^* \gg \xi_Q^* > 1$, Faraday rotation can dominate as absorption depth increases towards low frequency.

The order of the hierarchy of the transfer coefficients are somewhat different from that of power-law electrons, which, according to Jones and O'Dell[JO77], is $\xi_Q^* \gtrsim 1 > \xi_Q > \epsilon_Q \gg \xi_V > \epsilon_V$. The key difference is that the emission coefficients of monoenergetic electrons are slightly higher than the corresponding absorption coefficients. Whereas when there are lower energy electrons present, absorption is dominated by these low energy electrons. For the $V-$components, it is obvious that if a higher value γ is responsible for ϵ_V than for ξ_V, ξ_V can easily become larger than ϵ_V. Although it is not immediately obvious how γ affects the $Q-$components, realising that $x \propto \gamma^{-2}$, the same can be said for ξ_Q and ϵ_Q.

6.4 Degree of polarisation

Since the transfer coefficients are independent of distant r, Eq. (6.21) can be solved analytically. A discussion on methods for solving the transfer equation explicitly can be found in Chapter 6 of [Mel80]. For a given set of parameters $(\gamma, N_\mathrm{e}, B)$, the solution to Eq. (6.21) at a distant $r = R$, the surface of the source, is in the form

$$\begin{pmatrix} I_\nu \\ Q_\nu \\ U_\nu \\ V_\nu \end{pmatrix} = \begin{pmatrix} I_\nu^\infty \\ Q_\nu^\infty \\ U_\nu^\infty \\ V_\nu^\infty \end{pmatrix} - \mathrm{e}^{-\tau_\mathrm{s}} \begin{pmatrix} g_I(x) \\ g_Q(x) \\ g_U(x) \\ g_V(x) \end{pmatrix} \begin{pmatrix} I_\nu^\infty \\ Q_\nu^\infty \\ U_\nu^\infty \\ V_\nu^\infty \end{pmatrix} \quad (6.24)$$

where the functions $g_A(x)$ are functions of $\xi_{(Q,V)}$ and $\xi_{(Q,V)}^*$, and with (γ, N_e, B) fixed, they are functions of frequency, or x, only. The exact form of $g_A(x)$ can be found in Appendix B of Jones and O'Dell [JO77]. The superscript ∞ denotes solutions to Eq. (6.21) which dominates as $\tau_s \to \infty$.

The exact solutions are rather long and complicated, and do not give much insight into the behaviour of the polarised intensities. Therefore, for the purpose of analysing the behaviour of the linear and circular polarisation, we approximate the solutions to Eq. (6.21) in the optically thick region, and in the optically thin region. In the optically thick limit where $\tau_s \gg 1$, the second term on the right hand side of Eq. (6.24) vanishes as τ_s approaches ∞. In the optically thin limit, Eq. (6.21) is solved without the contribution from the absorption coefficients, which are negligible at $\tau_s \ll 1$.

Taking the hierarchy of the transfer coefficients into consideration, the solutions can be divided into two cases. In one case, where $(\xi_V^*/\xi_Q^*) \ll 1$ at moderate x, Faraday rotation is weak, and the other case in the strong rotativity limit at $x \ll 1$, $(\xi_V^*/\xi_Q^*) \gg 1$. In the strong rotativity limit $(\xi_V^*/\xi_Q^*) \gg 1$, for large absorption depth, $\tau_s \gg 1$,

$$
\begin{aligned}
r_L &\approx |\pi_U| \to \left| \frac{\epsilon_Q - \xi_Q}{\xi_V^*} \right| \\
r_C &\to -\left[(\epsilon_V - \xi_V) + \frac{\xi_Q^*}{\xi_V^*} (\epsilon_Q - \xi_Q) \right]
\end{aligned}
\tag{6.25}
$$

and for small absorption depth $\tau_s \ll 1$ with $|\xi_V^* \tau_s| \gg 1$,

$$
\begin{aligned}
r_L &\approx |\pi_U| \to \frac{\epsilon_Q}{|\xi_V^*| \tau_s} \\
r_C &\to -\left[\epsilon_V + \left(\frac{\xi_Q^*}{\xi_V^*} \right) \epsilon_Q \right]
\end{aligned}
\tag{6.26}
$$

Whereas in the weak rotation limit $(\xi_V^*/\xi_Q^*) \ll 1$, for strong absorption $\tau_s \gg 1$,

$$
\begin{aligned}
r_L &\approx |\pi_Q| \to |\epsilon_Q - \xi_Q| \\
r_C &\to -\left(\frac{\epsilon_V - \xi_V}{1 + \xi_Q^{*2}} \right)
\end{aligned}
\tag{6.27}
$$

and for small absorption depth $\tau_s \ll 1$,

$$
\begin{aligned}
r_L &\approx |\pi_Q| \to \epsilon_Q \\
r_C &\to -\epsilon_V
\end{aligned}
\tag{6.28}
$$
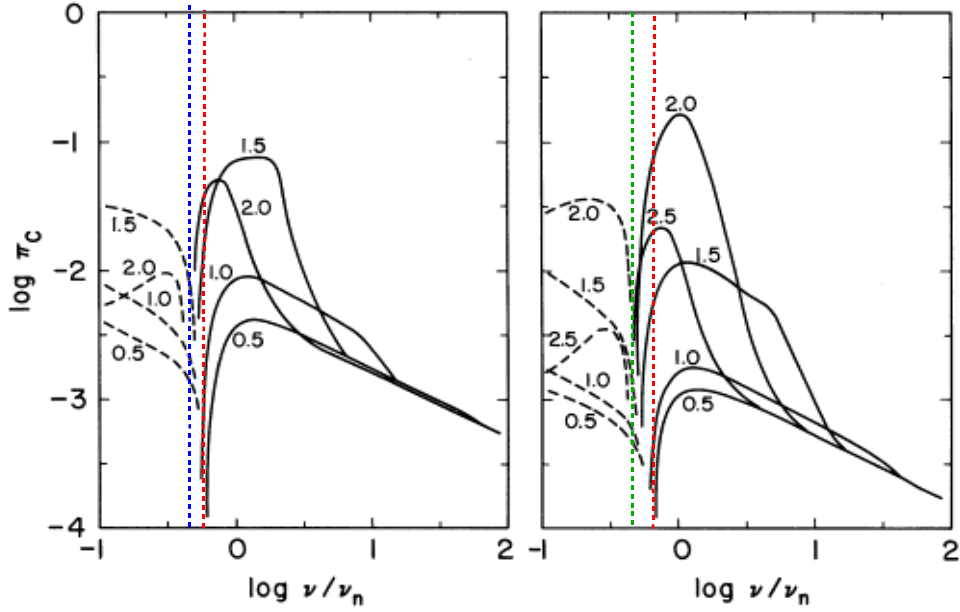
Figure 6.1: Degree of circular polarisation of a homogeneous, self-absorbed synchrotron source against $\nu/\nu_n = x$ (ν_n is equivalent to ν_{abs} in our notation). The calculation assume an angle $\theta = \pi/4$ and spectral index $\alpha = 0.5$. The characteristic Lorentz factor at the self-absorption frequency ν_n are $\gamma = 10^{2.5}$ (left) and $\gamma = 10^{3.0}$ (right). The numbers labelling each line represent the low energy cut-off as $\log_{10} \gamma_{min}$. The (black) dashed line indicates negative helicity. The red, blue and green dashed lines show the positions of sign reversal for $\gamma_{min} = 10^{0.5}$, $10^{2.0}$ and $10^{2.5}$ respectively. [JO77]

The approximations shown in Eqs. (6.25), (6.26), (6.27) and (6.28) are model independent. In a source with monoenergetic electrons where $\epsilon_Q > \xi_Q$ and $\epsilon_V > \xi_V$, the sign of the circular polarisation remains unchanged. If low energy electrons are present, such that $\xi_Q > \epsilon_Q$ and $\xi_V > \epsilon_V$, the sign of π_C changes at a frequency between the optically thick and the optically thin region, as shown in Fig. 6.1, at a frequency close to $x = 1$, as was suggested by Jones and O'Dell [JO77].

As we have shown in Chapter 4, the frequency x_{abs} at which the synchrotron optical depth $\tau_s = 1$, for a specified set of (N_e, B, R), depends on γ, in particular, x_{abs} decreases as γ increases. The frequency division, x_{rot}, between strong and weak

rotation is also strongly dependent on γ, where

$$\frac{\xi_V^*}{\xi_Q^*} = \frac{1.278}{x^{1/3}} \left(\frac{1 + \ln\gamma}{\gamma} \right) \tag{6.29}$$

Strong rotativity limit apply at frequencies

$$x < x_{\mathrm{rot}} \approx \left(\frac{1 + \ln\gamma}{\gamma} \right)^3 \tag{6.30}$$

For a power-law electron distribution which extends to $\gamma = 1$, $x_{\mathrm{rot}} \approx 1$, whereas for monoenergetic electrons with $\gamma \gg 1$, or in the presence of a low energy cut-off in the power-law spectrum, Faraday rotation dominates at much lower x. For example, monoenergetic electrons with energy $\gamma = 10^3$ or a cut-off in the power-law spectrum at this energy, $x_{\mathrm{rot}} \approx 5 \times 10^{-7}$.

6.5   Weak and strong absorption limit

The results summarised by Eqs. (6.25), (6.26), (6.27) and (6.28) can be used to study the two scenarios of the monoenergetic model, one with strong absorption and the other weak absorption, as described in Chapter 4. For a given set of (N_{e}, B, R), a large γ results in a weakly absorbing source, whereas a small γ results in a strongly absorbing source. We therefore consider two hypothetical cases, one of very high γ and one of very low γ, for a qualitative comparison, where we approximate Eqs. (6.25), (6.26), (6.27) and (6.28) according to the given criteria.

In a weakly absorbing source where $\gamma \gg 1$, we expect (1) the frequency at which the synchrotron optical depth $\tau_{\mathrm{s}} = 1$ $x_{\mathrm{abs}} \ll 1$ and (2) the frequency below which Faraday rotation dominates, $x_{\mathrm{rot}} \ll 1$. Therefore, the range of frequency can be divided into four regions:

Region $1 - x \ll 1$, $\tau_{\mathrm{s}} \gg 1$, $(\xi_V^*/\xi_Q^*) \gg 1$ [Eq. (6.25)]

$$r_{\mathrm{C}} \to - \left[\frac{0.785 x^{1/3}}{\gamma} - \frac{0.5x}{\gamma} - 0.368 \frac{\gamma}{(1 + \ln\gamma)} x^{5/3} \right] \tag{6.31}$$

Region $2 - x \ll 1$, $\tau_{\mathrm{s}} \gg 1$, $(\xi_V^*/\xi_Q^*) < 1$ [Eq. (6.27)]

$$r_{\mathrm{C}} \to - \left(\frac{0.390 x^{1/3} - 0.248x}{\gamma} \right) \tag{6.32}$$

Region 3 $- x \ll 1$, $\tau_\mathrm{s} \ll 1$, $(\xi_V^*/\xi_Q^*) \ll 1$ [Eq. (6.28)]

$$r_\mathrm{C} \to -\left(\frac{2.094}{\gamma}x^{1/3}\right) \tag{6.33}$$

Region 4 $- x \gg 1$, $\tau_\mathrm{s} \ll 1$, $(\xi_V^*/\xi_Q^*) \ll 1$ [Eq. (6.28)]

$$r_\mathrm{C} \to -\left(\frac{2.667}{\gamma}\frac{1+x}{x}\right) \tag{6.34}$$

In a strongly absorbing source, we consider $1 \le \gamma \le 10$. We expect (1) the frequency at which the synchrotron optical depth $\tau_\mathrm{s} = 1$ $x_\mathrm{abs} \gg 1$ and (2) the frequency below which Faraday rotation dominates, $x_\mathrm{rot} \lesssim 1$. The range of frequency in this case is divided into three regions:

Region 1 $- x \ll 1$, $\tau_\mathrm{s} \gg 1$, $(\xi_V^*/\xi_Q^*) \gg 1$ [Eq. (6.25)]

$$r_\mathrm{C} \to -\left[\frac{0.785x^{1/3}}{\gamma} - \frac{0.5x}{\gamma} - 0.368\frac{\gamma}{(1+\ln\gamma)}x^{5/3}\right] \tag{6.35}$$

Region 2 $- x \ll 1$, $\tau_\mathrm{s} > 1$, $(\xi_V^*/\xi_Q^*) < 1$ [Eq. (6.27)]

$$r_\mathrm{C} \to -\left(\frac{0.390x^{1/3} - 0.248x}{\gamma}\right) \tag{6.36}$$

Region 3 $- x \gg 1$, $\tau_\mathrm{s} \gg 1$, $(\xi_V^*/\xi_Q^*) \ll 1$ [Eq. (6.27)]

$$r_\mathrm{C} \to -\left[\frac{33.5x^{7/3}}{\gamma\left(33.3\mathrm{e}^{2x} + 25.1x^{7/3}\right)}\right] \tag{6.37}$$

The approximations of the degree of circular polarisation are plotted in Fig. 6.2, in which the weak (with $\gamma = 10^3$ on the right and $\gamma = 10^{2.5}$ on the left) and strong (with $\gamma = 10^{0.5}$ on the left and $\gamma = 1$ on the right) absorption cases are shown in the upper and lower panel, respectively. In both cases, lower value of γ generates higher degree of circular polarisation. Whereas in weakly absorbed sources, the maxima lie close to $x = 1$, in strongly absorbed sources, the maxima shift towards lower value of x as γ increases. Although in the right hand figure of the lower panel, in which $\gamma = 1$, the degree of circular polarisation is exceptionally high, this is not likely to be realistic since the electrons in this case are non-relativistic, and therefore synchrotron emission is not possible.

When the electron spectrum is a power-law, the higher energy electrons emit synchrotron radiation, which can then be circularly polarised by the low energy electrons
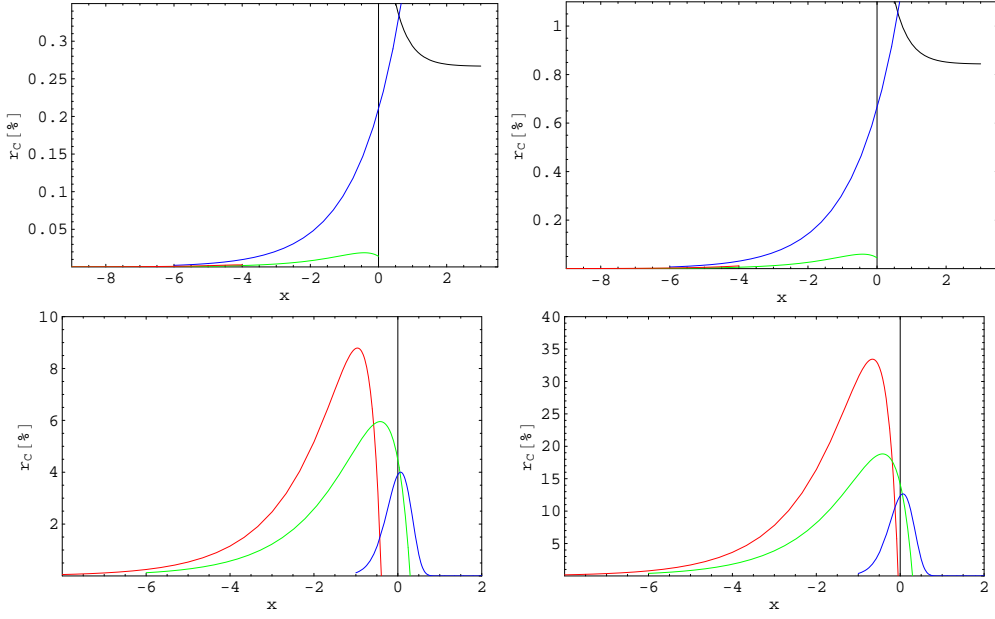
Figure 6.2: Approximation of degree of circular polarisation. Region 1 is shown in red, region 2 in green, region 3 in blue and region 4 in black. The degree of circular polarisation for all the approximations are multiplied with -1. Upper panel: Weak absorption with $\gamma = 10^3$ (left) and $\gamma = 10^{2.5}$ (right). Lower panel: Strong absorption with $\gamma = 10^{0.5}$ (left) and $\gamma = 1$ (right).

by Faraday conversion (and rotation in the limit of strong rotativity). Depending on the low energy cut-off in the electron spectrum, the maxima of the degree of circular polarisation can lie at or near $x = 1$, as shown by the lower panel of Fig. 6.2. Due to the stronger absorption by the lower energy electrons, there will also be a change of sign in the circular polarisation, as shown in Fig. 6.1 [JO77] in the previous section. The frequency at which the helicity of the circular polarisation changes from positive to negative shows similarly behaviour as the maxima of the degree of circular polarisation, as demonstrated by Fig. 6.1. The red dashed line shows (approximately) the position of $r_C = 0$ for $\gamma_{\min} = 10^{0.5}$. Comparing the position of the red dashed line to the position of the blue dashed line in the left hand figure, which shows the position of $r_C = 0$ for $\gamma_{\min} = 10^{2.0}$ and the green dashed line in the right hand figure that shows the position of $r_C = 0$ for $\gamma_{\min} = 10^{2.5}$, there is a slight shift towards lower value of x as $\gamma_{\min}$ increases.

Chapter 7

Discussion

7.1   Brightness temperature

The well-known upper limit on the brightness temperature of a synchrotron source $T_{\mathrm{B}} \lesssim 10^{12}\,\mathrm{K}$ imposed by the inverse Compton catastrophe, has been reassessed. We examine the brightness temperature limit by applying synchrotron theory to an electron distribution which has a cut-off or a deficit at low energies.

In Chapter 4, we show that in weakly absorbed sources (see Eq. (4.1)), the monoenergetic distribution mimics the situation in which the conventional power-law is truncated to lower energies at a Lorentz factor γ_{min}. Using the standard theory of synchrotron emission and self-absorption, we find that, for such sources, the brightness temperature at a frequency of a few GHz can reach approximately $10^{14}\,\mathrm{K}$, the precise limit being given in Eq. (4.32). Physically, this increased limit reflects the absence of cool electrons in monoenergetic distributions and in those that are truncated or hard below a certain Lorentz factor. As a consequence, intra-day variable sources can in principle be understood without recourse to other mechanisms such as unusually large Doppler factors [Ree67], coherent emission [e.g., LP92, BER05] or proton synchrotron radiation [Kar00].

The possibility of exceeding the new limit in a time-dependent solution by balancing losses against a strong acceleration term has been investigated using a set of spatially averaged equations. Provided the acceleration process remains causal i.e., the acceleration time averaged over the source remains longer than the light-crossing time, we find a modest overshoot is possible, but the maximum temperature is still restricted by Eq. (4.32). In strongly absorbed sources, such as those considered by [Sly92], high

brightness temperatures cannot be attained in a self-consistent model of the kind we discuss. As the synchrotron photons build up and are then repeatedly scattered to higher energies by the relativistic electrons, the resulting γ-ray photons interact with the synchrotron photons to produce electron-positron pairs. The synchrotron flux and therefore the brightness temperature is reduced as a result.

We have examined in detail the parameter space available to homogeneous synchrotron sources of fixed size. In the case of flat spectrum sources, we find that the imposition of the condition of equipartition between the particle and magnetic field energy densities does not result in a lower limit on the brightness temperature than that given by the inverse Compton catastrophe. Suggestions to the contrary [Rea94] are based on the more restrictive twin assumptions that the power-law electron distribution is not truncated within the relevant range, and that the temperature is measured at the point where the optical depth of the source is approximately unity. Consequently, the observed temperature distribution does not support the equipartition hypothesis. We also find that flat spectrum sources close to equipartition can approach the threshold temperature of the inverse Compton catastrophe, in contrast with the finding based on the more restrictive assumptions in Readhead [Rea94].

7.2   Spectral properties

In Chapter 5, we computed the synchrotron and inverse Compton spectra from monoenergetic electrons and from electron distributions which are truncated or hard below a certain Lorentz factor. We apply the two models to the BL Lac object S5 0716+714, and compared them to the observed spectral energy distribution (SED) of the source.

The SED of four models − two of monoenergetic electrons at $\gamma = \gamma_{\mathrm{p}}$, two of power-law electron distributions that is hard below γ_{p} − were shown in Figs. 5.3 and 5.4, all of which have brightness temperatures well above the conventional Compton limit of $\sim 10^{12}$ K [KP69] at 32 GHz. Although all of the models have brightness temperature exceeded 10^{12} K, they are in fact well below the threshold of Compton catastrophe ($\xi < 1$).

The inverted radio spectrum ($\alpha \sim -0.3$, $F_\nu \propto \nu^{-\alpha}$) in the observed SED was

interpreted as the result of a superposition of optically thick synchrotron spectra arise from an inhomogeneous source. The spectral turn over at $\sim 10^{11.5}$ Hz was interpreted as the result of the change in opacity of the source by Ostorero et al (2006) [OWG$^+$06]. In our interpretation, the inverted radio spectrum arises naturally from an electron distribution truncated below a certain energy, and the spectral turning is a result of a spectral break in the electron spectrum − on either side of this turning point, the spectrum remains optically thin. The self-absorption frequency ν_{abs} lies at a much lower frequency ($\sim$ 4 GHz). Our interpretation, therefore, does not require specific gradients in the magnetic field strength and particle number density, and implies a weaker magnetic field and/or a lower electron density.

One might suspect that at brightness temperature much exceeding 10^9 K, the effect of induced Compton scattering would become significant [Syu71]. Qualitative argument reveal that this process is insignificant in the scenario of our model, since the photon occupation number ($\propto F_\nu/\nu^3$) at frequencies that permits coupling of photon to electrons at γ_{p} is negligibly small. If we examine this point more explicitly, order of magnitude estimate limits the brightness temperature of a self-absorbed synchrotron source, imposed by relativistic induced Compton scattering, to $(k_{\text{B}}T_{\text{B}}/mc^2)\tau_{\text{T}} < 1$. In order to account for a substantial X−ray and γ−ray emission by conventional synchrotron theory, in which the electron spectrum ($\propto \gamma^{-p}$) extends to $\gamma_{\text{min}} = 1$, high τ_{T} is required since $\xi \propto \tau_{\text{T}}\gamma_{\text{p}}^{1-p} \approx \tau_{\text{T}}$, where $\gamma_{\text{p}} = \gamma_{\text{min}} = 1$. In S5 0716+714, if we assume that the γ−ray emission is roughly 1 order of magnitude lower ($\tau_{\text{T}} \approx \xi \sim 0.1$), this gives a limit of $T_{\text{B}} < 6 \times 10^{10}$ K. In our models, however, a high τ_{T} is not necessary due to the low energy cut-off in the electron spectrum, such that ξ can be large even with small τ_{T}. For the models shown in Figs. 5.3 and 5.4, the limit imposed by induced Compton scattering equates to $T_{\text{B}} < 6 \times 10^{16}\tau_{\text{T},-7}$ K, where $\tau_{\text{T},-7}$ is τ_{T} in unit of 10^{-7}.

Observations of S5 0716+714 from infrared to optical frequencies suggest that the spectral energy distribution between the frequencies $\nu_{\text{K}} = 1.38 \times 10^{14}$ Hz and $\nu_{\text{B}} = 6.81 \times 10^{14}$ Hz can be well fitted by the power law $F_\nu \propto \nu^{-1.12}$ [HLE$^+$06]. Clearly, the top panel in Fig. 5.5 is much too hard at these frequencies. However, the spectrum can be softened by simply lowering the cut-off frequency of the synchrotron spectrum ν_{max} (i.e., lowering γ_{max}, bottom panel in Fig. 5.5). By decreasing ν_{max} to

approximately ν_{K}, the spectrum begins an exponential drop at or just before reaching the relevant frequency range, and as a result, softens the spectrum. This does not alter the level of flux or the spectral shape at frequencies $\ll \nu_{\mathrm{max}}$.

The figure in the bottom panel of Fig. 5.5 demonstrates that if the variability of S5 0716+714 is intrinsic, the Doppler boosting factor of the emission region has a lower limit of $\mathcal{D} = 65$, which is $2 - 3$ times higher than the range suggested by Bach et al (2005) [BKR$^+$05], in which they interpret the range of apparent superluminal motion in the jet components by adopting a small ($2°$) viewing angle and large bulk Lorentz factor ($\Gamma \approx 15$), which leads to $\mathcal{D} \sim 20-30$. To explain this result requires the jet components to be moving much faster during the observations of Ostorero et al (2006) than during the VLBA observations studied by Bach et al (2005). Alternatively, the observed SED can be explained by assuming that emission at frequency below 32 GHz has a different origin that is larger than the region responsible for the emission and variability at 32 GHz. This allows the Doppler factor to be reduced to a value $\lesssim 30$ by increasing the self-absorption frequency ν_{abs} to 32 GHz, as shown in the top panel of Fig. 5.5. We find that to remain below the INTEGRAL upper limits, a minimum Doppler factor of $\mathcal{D} = 30$ is required for a maximum self-absorption frequency of $\nu_{\mathrm{abs}} = 32$ GHz.

The models shown in Chapter 4 are away from equipartition of magnetic field and particle energy, and in all of the examples (with the exception of the rejected model, which will not be discussed here), the energy content is dominated by that in the energetic electrons. This requires a larger amount of energy compared to the equipartition energy (approximately the minimum energy requirement, see Chapter 2 and [e.g. Lon92, Chapter 19]), which in turn imposes a high energy demand from the host galaxy. In a typical galaxy of $\sim 10^{11} M_{\odot}$, the total energy available from accretion of $\sim 10\%$ efficiency is $\sim 10^{64}$ ergs. If the age of the universe is $\approx 10^{10}$ years, it implies that the jet power cannot exceed 10^{47} ergss^{-1}. From VLBI observations of the proper motion of 11 jet components of S5 0716+714, we estimated the jet power required for each of the models in order to account for the time scale of approximately 1 year [BKR$^+$05] between the occurrence of two jet components. As shown in Table 5.1, the values of the estimated jet power are within the plausible range.

The example of S5 0716+714 has demonstrated several important spectral prop-

erties, derived from an electron distribution that has a deficit below a certain energy, as described in Chapter 4. The most noticeable feature is the hard, inverted optically thin synchrotron spectrum, spanning a wide frequency range as $F_\nu \propto \nu^{1/3}$. This is a useful feature when applying to compact radio sources, which often show this type of behaviour at radio frequencies [e.g., GSH$^+$94, KJW$^+$01]. Other features are the spectral breaks which arise from the corresponding spectral break in the stationary electron spectrum, at $\nu_{\rm p} = \gamma_{\rm p}^2 \nu_0$, $\nu_{\rm cool} = \gamma_{\rm cool}^2 \nu_0$, and the exponential cut-off at $\nu_{\rm max} = \gamma_{\rm max}^2 \nu_0$.

As explained in Section 5.2 of Chapter 4, whether $\gamma_{\rm p}$ lies below or above $\gamma_{\rm cool}$ determines the final electron energy distribution, which in term affects the spectral index of the high energy "tail" of the synchrotron spectrum at frequencies beyond the first spectral break. If the number of electrons leaving the energy bin $\gamma_{\rm p} mc^2$ is dominated by radiative cooling, the synchrotron spectrum continues from $F_\nu \propto \nu^{1/3}$ between $\nu_{\rm abs}$ and $\nu_{\rm cool}$, to $F_\nu \propto \nu^{-1/2}$ between $\nu_{\rm cool}$ and $\nu_{\rm p}$, then $F_\nu \propto \nu^{s_2/2}$ between $\nu_{\rm p}$ and $\nu_{\rm max}$, and cut-off exponentially beyond $\nu_{\rm max}$. In this case, the low frequency part of the synchrotron spectrum below $\nu_{\rm cool}$ resembles that from a monoenergetic electron distribution of energy $\gamma_{\rm cool} mc^2$. If, on the other hand, the loss is dominated by electrons evacuating the emission zone over a time-scale of $t_{\rm esc} = R/c$, the synchrotron spectrum continues from $F_\nu \propto \nu^{1/3}$ between $\nu_{\rm abs}$ and $\nu_{\rm p}$, to $F_\nu \propto \nu^{(s_2+1)/2}$ between $\nu_{\rm p}$ and $\nu_{\rm cool}$, then $F_\nu \propto \nu^{s_2/2}$ between $\nu_{\rm cool}$ and $\nu_{\rm max}$, and again cut-off exponentially beyond $\nu_{\rm max}$. The spectrum of this distribution at frequency below $\gamma_{\rm p}$ is the same as that of the synchrotron spectrum from a monoenergetic distribution of electron of energy $\gamma_{\rm p} mc^2$.

7.3 Circular polarisation

In Chapter 6, we computed the coefficients of both the dissipative (due to self-absorption) and non-dissipative (due to Faraday conversion and rotation) radiation transfer processes. The polarised emission and transfer coefficients were normalised by the unpolarised counterparts. By approximating the solutions to the radiation transfer equation in the optically thick and optically thin limits, and then comparing the magnitude of the normalised coefficients, we found that, in contrast to electrons with a power law energy distribution, the sign of the circular polarisation of the synchrotron emission from monoenergetic electrons does not reverse at any frequency over the whole

range of frequency of the synchrotron spectrum.

The difference arises from the fact that self-absorption is dominated by the lowest energy electrons in a power-law distribution (which has a higher number density), whereas emission is dominated by the highest energy electrons (which has a lower number density). Eq. (6.22) of Chapter 6 which shows the expression of the normalised transfer coefficients, demonstrates that when the polarised absorption in the source exceeds the polarised emission, Eqs. (6.25), (6.26), (6.27) and (6.28) imply a sign reversal of the circular polarisation as an optically thin source becomes optically thick to synchrotron emission. In a source which contains monoenergetic electrons, the normalised emission coefficients exceed their absorption counterparts, which, according to Eqs. (6.25), (6.26), (6.27) and (6.28), imply the sign of circular polarisation of the synchrotron emission does not change. The result is unaffected by the dominance of Faraday rotation over other processes as the main effect that alter the circular polarisation at very low frequency, or of Faraday conversion at higher frequency.

The maximum degree of circular polarisation in a source with monoenergetic electrons is observed at the synchrotron self-absorption frequency in the case of strong absorption and near $x = 1$ for weak absorption. In the common form of power-law electron distribution, in which the lowest energy electrons are assumed to have $\gamma = 1$, the maximum degree of circular polarisation r_c is observed at $x \approx 1$ (see Fig. 6.2). We also expect the sign reversal to occur at $x \approx 1$ in this case since, for a power law energy distribution that extends to $\gamma = 1$, the self-absorption frequency is also at $x_a \approx 1$. Whereas in a power-law spectrum that has a low energy cut-off at $\gamma_{\min}$, the maximum r_c and the sign change is observed at the corresponding self-absorption frequency, which shift towards lower value of x as $\gamma_{\min}$ increases.

Chapter 8

Conclusions

Since intraday variability was first observed in the optical band in 3C 279 by Oke (1967) [Oke67], this phenomenon is frequently observed in many blazars throughout the whole electromagnetic spectrum from the radio band to γ-ray energies, with the first observation of radio intraday variability in OJ 287 reported by Kinman and Conklin (1971) [see EFK$^+$72, and references therein]. Much effort has been put into the development of theoretical models to explain radio IDV, including the interpretation of IDV as a result of propagation effects that causes rapid fluctuations, and mechanisms that are intrinsic to the source which can generate high fluxes in a compact region. However, no single mechanism can conclusively account for the observed IDV in all the sources so far. Whereas it is widely accepted in many cases that the very rapid flux variations are due to interstellar scintillation, the extremely high intrinsic brightness temperature of the source, which appears to contradict with the limit imposed by the onset of Compton catastrophe in a self-absorbed synchrotron source, still requires explanations.

This work intend to develop a comprehensive model that aims to reproduce the observed high brightness temperature. The central idea of the model is an electron distribution which cuts off at low energy. The approximation of such a distribution as monoenergetic has been examined by Crusius-Waetzel (1991) [Cru91], Slysh (1992) [Sly92] and Protheroe (2003) [Pro03] (see Chapter 3 for brief discussions on these work), and observational evidence of a low energy cut off in the electron distribution has been found, for example, by Gopal-Krishna et al (2004) [GBW04] and Blundell et al (2006) [BFC$^+$06] (see Chapter 4).

We first computed the maximum brightness temperature of monoenergetic electrons limited by the onset of catastrophic cooling of the energetic electrons. The lack of low energy electrons gives rise to weaker absorption in the source, allowing more GHz photons to emerge, and hence brightness temperature higher than 10^{12} K can be observed. From our analysis of the intrinsic source parameters, we find that equipartition of energy in the source does not prevent it from catastrophic Compton cooling, as was suggested by Readhead (1994) [Rea94, and discussion in Chapter 2]. The prevention of Compton catastrophe in a source where there is equipartition of energy only apply to monoenergetic sources which self absorption frequency coincides with the characteristic frequency ($x_{\mathrm{a}} = 1$) or if one is restricted to observe at the synchrotron peak (at $\tau_{\mathrm{s}} = 1$) in a source with an electron distribution which is a power law in energy. Reproducing brightness temperature much in excess of 10^{12} K by an injection of highly relativistic electrons, or by continuous fast acceleration within the source to counteract the effect of radiative cooling [Sly92, and Chapter 2], is proven unfeasible. The underlying reason is that extremely compact sources would be required, in which copious pair-production must be taken into account. These results are presented in Chapter 4.

In the next stage, we computed the synchrotron and self-Compton spectra of monoenergetic electrons, and apply this model to the simultaneous multi-frequency spectrum of S5 0716+714. The $\nu^{1/3}$ dependence at the radio frequencies is well fitted by synchrotron spectrum of monoenergetic electrons. However, this simple approximation is insufficient to account for the emission at optical frequencies. We therefore revert to our original scenario of an electron distribution with a low energy cut off. We assume a continuous injection of electron with a double power law energy distribution, which has a hard low energy spectrum that does not contribute significantly to the absorption of synchrotron photons. Computing the synchrotron self-Compton spectrum of the stationary distribution resulted from balancing the continuous injection with losses due to radiation and electrons leaving the emission region, the SED of S5 0716+714 can be fitted by two limiting cases. In one case, the jet components responsible for the emission is moving much faster than during the VLBI observations analysed by Bach et al (2005), or emission below 32 GHz originates from a bigger region than emission above this frequency.

To complete the analysis of the monoenergetic electrons model, we examine the circular polarisation properties of its synchrotron emission. Computing the polarised emission, absorption and the Faraday effects, and examining the solutions to the radiative transfer equations in the limits of very small and very large synchrotron optical depth, we concluded that the sign of circular polarisation does not reverse at any frequency throughout the entire synchrotron spectrum, if the radiating particles are monoenergetic electrons. This does not contradict with the results of Jones and O'Dell (1977) [JO77], in which they claim that circular polarisation changes sign as the source becomes optically thick, this is consistent with our findings since in a power law energy distribution of electrons, the polarised absorption is dominated by low energy electrons, whereas emission is dominated by high energy electrons. The computation and discussion of these results are presented in Chapter 6.

The model presented here can account for the high brightness temperature inferred from the rapid flux variations observed in many extra-galactic radio sources. The brightness temperature is not restricted by equipartition of energy in the source, and the model does not require special geometrical effect for a high synchrotron flux to be observed. Due to the variable nature of IDV sources, the energy distribution of the electrons must be constrained by simultaneous observations from radio to X- or γ-ray energies. Without these observations, the source parameters can only be estimated using the monoenergetic approximation.

Appendix A

Synchrotron Formulae for Monoenergetic Electrons

We consider a region of homogeneous magnetic field B, linear dimension R, (and volume R^3) containing monoenergetic electrons/positron of number density N_e and Lorentz factor γ. We begin with replacing the power-law electron phase space distribution $n_e(\gamma) \propto \gamma^{-s}$ by $n_e(\gamma') = N_e\delta(\gamma' - \gamma)$ in the standard synchrotron theory defined in Chapter 1 in Eqs. (1.4), (1.7) and (1.12). The unpolarised synchrotron volume emissivity, absorption coefficient and source function are

$$
\begin{aligned}
J_\nu &= \frac{\sqrt{3}}{4\pi}\alpha_f N_e h\nu_L \sin\theta F(x) \\
\alpha_\nu &= \frac{1}{2\sqrt{3}}\frac{N_e\sigma_T}{\alpha_f \hat{B}\sin\theta}\frac{K_{5/3}(x)}{\gamma^5} \\
S_\nu &= \frac{J_\nu}{\alpha_\nu} = \left(\frac{\nu_s}{c}\right)^2 \gamma mc^2 \frac{F(x)}{K_{5/3}(x)}
\end{aligned}
\tag{A.1}
$$

in the rest frame of the source, where σ_T is the Thomson cross section, α_f is the fine structure constant, and $\hat{B} = B/B_c$, B_c is the critical magnetic field defined by $\hbar(eB_c/mc) = mc^2$, $B_c = 4.414 \times 10^{13}\,\mathrm{G}$, and

$$
\begin{aligned}
x &= \nu/\nu_s \tag{A.2} \\
\nu_s(\gamma,\theta) &= \frac{3}{2}\nu_L \sin\theta\gamma^2 \\
&= \nu_0\gamma^2 \qquad [\nu_0 = 3\nu_L \sin\theta/2] \tag{A.3} \\
F(x) &= x\int_x^\infty \mathrm{d}t K_{5/3}(t) \tag{A.4}
\end{aligned}
$$

$\nu_L = eB/(2\pi mc)$ the Larmor frequency and θ the angle between the magnetic field and the direction of the emitted radiation. For small and large x, the limiting forms of the modified Bessel function $K_{5/3}(x)$ are:

$$
K_{5/3}(x) \approx \frac{2^{2/3}\Gamma(5/3)}{x^{5/3}} \quad \text{for } x \ll 1 \tag{A.5}
$$

$$K_{5/3}(x) \;\rightarrow\; \sqrt{\frac{\pi}{2x}}e^{-x} \quad \text{for } x \rightarrow \infty \tag{A.6}$$

and the limiting forms of $F(x)$ are

$$F(x) \;\approx\; \frac{4\pi}{\sqrt{3}\Gamma(1/3)}\left(\frac{x}{2}\right)^{1/3} \quad \text{for } x \ll 1 \tag{A.7}$$

$$F(x) \;\rightarrow\; \sqrt{\frac{\pi x}{2}}e^{-x} \quad \text{for } x \rightarrow \infty \tag{A.8}$$

Because α_ν is a monotonically decreasing function of x, we can define a unique $x_{\mathrm{a}}(\hat{B}, \gamma)$ where the optical depth $\tau_{\mathrm{s}} = R\alpha_\nu$ for synchrotron absorption along a path of length R is unity:

$$\alpha_\nu R\,(x_{\mathrm{a}}) \;=\; 1 \tag{A.9}$$

If $x_{\mathrm{a}} \ll 1$, we have **weak absorption** and for $x_{\mathrm{a}} \gg 1$ **strong absorption**. The transition between the two regimes occurs near Lorentz factor γ_{c}, defined as

$$\gamma_{\mathrm{c}} \;=\; \left(\frac{\tau_{\mathrm{T}}}{2\sqrt{3}\alpha_{\mathrm{f}}\hat{B}\sin\theta}\right)^{1/5} \tag{A.10}$$

so that

$$\begin{aligned} \tau_{\mathrm{s}} \;&=\; \hat{\gamma}^{-5}K_{5/3}(x) \\ &=\; \frac{\sqrt{3}\tau_{\mathrm{T}}mc^3 K_{5/3}(x)}{8\pi e^2 \nu_{\mathrm{c}}\gamma^3} \end{aligned} \tag{A.11}$$

where $\hat{\gamma} = \gamma/\gamma_{\mathrm{c}}$, and the Thomson optical depth τ_{T} is defined as

$$\tau_{\mathrm{T}} \;=\; N_{\mathrm{e}}R\sigma_{\mathrm{T}} \tag{A.12}$$

In the case of weak absorption,

$$x_{\mathrm{a}} \;\approx\; 2^{2/5}\left[\Gamma(5/3)\right]^{3/5}/\hat{\gamma}^3 \quad \text{for } \hat{\gamma} \gg 1 \tag{A.13}$$

whereas in the strong absorption regime

$$x_{\mathrm{a}} \;\sim\; -5\ln\hat{\gamma} \quad \text{for } \hat{\gamma} \ll 1 \tag{A.14}$$

The source function in Eq. (A.1) can be rewritten as

$$S_\nu \;=\; \left(\frac{B^2}{8\pi}\right)\left(\frac{9e^2\gamma_{\mathrm{c}}^5}{2\pi mc^2}\right)\sin^2\theta\,S(\hat{\gamma}, x) \tag{A.15}$$

with

$$S(\hat{\gamma}, x) = \frac{\hat{\gamma}^5 F(x)}{K_{5/3}(x)} \tag{A.16}$$

$$\rightarrow \begin{cases} \frac{2\pi}{\sqrt{3}\Gamma(1/3)\Gamma(5/3)}\hat{\gamma}^5 x^2 & \text{as } x \rightarrow 0 \\ \hat{\gamma}^5 x & \text{as } x \rightarrow \infty \end{cases} \tag{A.17}$$

and the optical depth to synchrotron absorption $\tau_{\rm s}$ is a function of $\hat{\gamma}$ and x.

A.1   Energy density

To find the energy density $U_{\rm s}$ in synchrotron photons in a given source, I_ν must be integrated over angles and over frequency, where $I_\nu = S_\nu[1 - \exp(-\tau_{\rm s})]$, as defined in Eq. (1.16). The result depends on the geometry and optical depth as well as the position within the source. However, an average value can be estimated by introducing a geometry dependent factor $\zeta \approx 1$:

$$U_{\rm s} \approx \frac{4\pi\zeta}{c} \int_0^\infty d\nu \, \langle I_\nu \rangle \tag{A.18}$$

and denoting by $\langle I_\nu \rangle$ the specific intensity evaluated at $\theta = \pi/2$. Then

$$U_{\rm s} = \zeta \left(\frac{B^2}{8\pi} \right) \left(\frac{27\alpha_{\rm f}}{2\pi} \right) \hat{B}\gamma_{\rm c}^7 U(\hat{\gamma}) \tag{A.19}$$

with

$$U(\hat{\gamma}) = \hat{\gamma}^2 \int_0^\infty dx S(\hat{\gamma}, x) \{1 - \exp[-\tau_{\rm s}(\hat{\gamma}, x)]\} \tag{A.20}$$

This integral is dominated by the region $x \gg x_{\rm a}$ in the weak absorption regime:

$$\begin{aligned} U(\hat{\gamma}) &\approx \int_0^\infty dx \, S\tau_{\rm s} \\ &= \int_0^\infty dx \, F(x) \\ &= \frac{8\pi\hat{\gamma}^2}{9\sqrt{3}} \quad \text{for } \hat{\gamma} \gg 1 \end{aligned} \tag{A.21}$$

and by the region around $x = x_{\rm a}$ in the strong absorption regime:

$$\begin{aligned} U(\hat{\gamma}) &\approx \int_0^{x_{\rm a}} dx \, S \\ &\approx 12.5\hat{\gamma}^7 (\ln \hat{\gamma})^2 \quad \text{for } \hat{\gamma} \ll 1 \end{aligned} \tag{A.22}$$

which suggests the simple approximation

$$U(\hat{\gamma}) \approx \frac{12.5\hat{\gamma}^7}{\left[0.183 + (\ln\hat{\gamma})^2\right]^{-1} + 7.75\hat{\gamma}^5} \tag{A.23}$$

where the constant 0.183 was chosen such that the approximation passes through the point $U(1) = 0.945$ found by numerical integration.

A.2 Brightness temperature

Denoting quantities in the co-moving frame of the source with prime, the brightness temperature is defined as

$$T_B' = \frac{c^2}{2\nu'^2 k_B} I_\nu'$$

which transformed to the rest frame of the observer as

$$T_B = \left(\frac{\mathcal{D}}{(1+z)}\right) \frac{c^2}{2\nu k_B} I_\nu$$

The dimensionless form of the brightness temperature can then be written, in the co-moving frame of the source, as

$$\frac{k_B T_B'}{mc^2} = \frac{I_\nu'}{2m\nu'^2} = \frac{S_\nu'(1 - e^{-\tau_s})}{2m\nu'^2} \tag{A.24}$$

where S_ν' is as defined in Eq. (A.1).

$$\frac{k_B T_B'}{mc^2} = \left(\frac{\nu_s}{c}\right)^2 \frac{\gamma mc^2}{2m\nu'^2} \frac{F(x)}{K_{5/3}(x)}(1 - e^{-\tau_s})$$

Replacing ν_s/ν' by $1/x$, and transforming to the rest frame of the observer,

$$\frac{k_B T_B}{mc^2} = \left(\frac{\mathcal{D}}{1+z}\right)\left(\frac{\gamma F(x)}{2x^2 K_{5/3}(x)}\right)(1 - e^{-\tau_s}) \tag{A.25}$$

Introducing the Comptonisation parameter ξ, defined as the ratio of inverse Compton luminosity to synchrotron luminosity, and rewriting x in the rest frame of the observer,

$$\xi = \frac{4\gamma^2 \tau_T}{3}$$

$$x = \frac{\nu}{\nu_s}\frac{(1+z)}{\mathcal{D}} = \frac{\nu}{\nu_{max}} \tag{A.26}$$

where $\mathcal{D}$ is the Doppler factor, z is the red-shift of the host galaxy and ν_{max} is the frequency at which the observed synchrotron spectrum cuts off exponentially. γ can be replaced in favour of τ_{s} and ξ and x, such that

$$\gamma = \left(\frac{3^{3/2} m c^3 K_{5/3}(x) \mathcal{D} x \xi}{32 \pi e^2 \tau_{\text{s}} \nu (1 + z)} \right)^{1/5} \tag{A.27}$$

Eq. 4.30 can be rewritten in terms of τ_{s}, ξ and x,

$$\frac{k_{\text{B}} T_{\text{B}}}{m c^2} = \left(\frac{3^{3/2} m c^3}{4^5 \pi e^2 \nu} \right)^{1/5} \left[\xi \left(\frac{\mathcal{D}}{1 + z} \right)^6 \right]^{1/5} \left(\frac{1 - e^{-\tau_{\text{s}}}}{\tau_{\text{s}}^{1/5}} \right) \left(\frac{F(x)}{x^{9/5} K_{5/3}^{4/5}(x)} \right) \tag{A.28}$$

In the limit of $x \ll 1$, $F(x)$ and $K_{5/3}(x)$ in Eq. (A.28) can be replaced by the approximations given in Eqs. (A.7) and (A.5), the brightness temperature T_B can be expressed in convenient units as

$$T_{\text{B}} = 1.2 \times 10^{14} \left(\frac{\mathcal{D}_{10}^6 \xi}{(1 + z)^6} \right)^{1/5} \left(\frac{1 - e^{-\tau_{\text{s}}}}{\tau_{\text{s}}^{1/5}} \right) \nu_{\text{max},14}^{2/15} \nu_{\text{GHz}}^{-1/3} \text{ K} \tag{A.29}$$

where $\mathcal{D}_{10} = \mathcal{D}/10$ and $\nu_{\text{GHz}} = \nu/10^9$ and $\nu_{\text{max},14} = \nu_{\text{max}}/10^{14}$ Hz.

We define η as the ratio of the energy density in relativistic electrons to that in the magnetic field, such that

$$\eta = \frac{N_{\text{e}} \gamma m c^2}{(B^2/8\pi)}$$

B and n can be substituted using the expressions for the Thomson optical depth τ_{T} and the synchrotron characteristic frequency, given in Eq. (A.12), and ξ in Eq. (A.26),

$$B = \frac{4\pi}{3} \frac{m c \nu_{\text{s}}}{e \sin \theta \gamma^2}$$

$$N_{\text{e}} = \frac{\tau_{\text{T}}}{R \sigma_{\text{T}}} = \frac{3}{4} \frac{\xi}{\gamma^2 R \sigma_{\text{T}}} \tag{A.30}$$

η then becomes

$$\eta = 8\pi \gamma m c^2 \left(\frac{3}{4} \frac{\xi}{\gamma^2 R \sigma_{\text{T}}} \right) \left(\frac{3}{4\pi} \frac{e \sin \theta \gamma^2}{m c \nu_{\text{s}}} \right)^2$$

Replacing γ by Eq. A.27,

$$\eta = \left(\frac{3^{39/2} c^9 e^4 K_{5/3}(x)^3}{64^5 m^2 \pi^8 \sigma_{\text{T}}^5} \right)^{1/5} \frac{\sin^2 \theta}{R} \left(\frac{\mathcal{D}^{13} \xi^8}{\tau_{\text{s}}^3 \nu_{\text{max}}^{13} (1 + z)^{13}} \right)^{1/5}$$

In the limit $x \ll 1$, $K_{5/3}(x)$ is approximated as in Eq. (A.5), replacing x with $\nu/\nu_{\max}$,

$$
\eta = \left(\frac{3^{39/2} c^9 e^4}{32^5 m^2 \pi^8 \sigma_{\mathrm{T}}^5} \right)^{1/5} \frac{\sin^2 \theta}{R} \left(\frac{\mathcal{D}^{13} \xi^8}{\tau_{\mathrm{s}}^3 \nu_{\max}^8 (1+z)^{13}} \right)^{1/5} \nu^{-1}
$$

again, we can express η in terms of $(\xi, \nu_{\mathrm{GHz}}, \nu_{\max,14}, \tau_{\mathrm{s}})$

$$
\eta = 2.9 \times \left(\frac{\mathcal{D}_{10}}{1+z} \right)^{13/5} \left(\frac{\xi^8}{\tau_{\mathrm{s}}^3} \right)^{1/5} \sin^2 \theta \, R_{-2}^{-1} \, \nu_{\max,14}^{-8/5} \, \nu_{\mathrm{GHz}}^{-1}
$$

where, again, $\mathcal{D}_{10} = \mathcal{D}/10$, $\nu_{\max,14} = \nu_{\max}/10^{14}$ Hz, $\nu_{\mathrm{GHz}} = \nu/10^9$ Hz and $R_{-2} = 100R$ pc. Analogously, the total energy content, E_{total}, and the synchrotron cooling time t_{cool}, where

$$
E_{\mathrm{total}} = (N_{\mathrm{e}} \gamma m c^2 + \frac{B^2}{8\pi}) R^3
$$

$$
t_{\mathrm{cool}} = \gamma/\dot{\gamma}
$$

$$
\dot{\gamma} = \frac{4}{3} \frac{\sigma_{\mathrm{T}}}{mc} \left(\frac{B^2}{8\pi} \right)
$$

can also be rewritten as

$$
E_{\mathrm{total}} = 4.6 \times 10^{47} \left(\frac{\mathcal{D}_{10}}{1+z} \right)^{-14/5} \left(\frac{\xi}{\tau_{\mathrm{s}}} \right)^{-4/5} \sin^{-2}\theta \, R_{-2}^3 \, \nu_{\max,14}^{22/15} \, \nu_{\mathrm{GHz}}^{30/17} \text{ ergs}
$$

$$
\frac{ct_{\mathrm{cool}}}{R} = 2.9 \times \left(\frac{\mathcal{D}_{10}}{1+z} \right)^{13/5} \left(\frac{\xi}{\tau_{\mathrm{s}}} \right)^{3/5} \sin^2 \theta \, R_{-2}^{-1} \, \nu_{\max,14}^{-8/5} \, \nu_{\mathrm{GHz}}^{-1}
$$

Bibliography

[BER05] M. C. Begelman, R. E. Ergun, and M. J. Rees. Cyclotron Maser Emission from Blazar Jets? ApJ, 625:51–59, May 2005.

[BFC+06] K. Blundell, A. Fabian, C. Crawford, M. Erlund, and A. Celotti. Discovery of the low-energy cutoff in a powerful giant radio galaxy. ArXiv Astrophysics e-prints, May 2006.

[BKR+05] U. Bach, T. P. Krichbaum, E. Ros, S. Britzen, W. W. Tian, A. Kraus, A. Witzel, and J. A. Zensus. Kinematic study of the blazar ¡ASTROBJ¿S5 0716+714¡/ASTROBJ¿. A&A, 433:815–825, April 2005.

[BL98] G. Benford and H. Lesch. Coherent emission and the escape of high brightness temperature radiation in active galactic nuclei. MNRAS, 301:414–418, December 1998.

[BMJ+06] H. E. Bignall, J.-P. Macquart, D. L. Jauncey, J. E. J. Lovell, A. K. Tzioumis, and L. Kedziora-Chudczer. Rapid Interstellar Scintillation of PKS 1257-326: Two-Station Pattern Time Delays and Constraints on Scattering and Microarcsecond Source Structure. ApJ, 652:1050–1058, December 2006.

[Bre90] J. N. Bregman. Continuum radiation from active galactic nuclei. A&A Rev., 2:125–166, 1990.

[BSP+92] P. L. Biermann, R. Schaaf, W. Pietsch, T. Schmutzler, A. Witzel, and H. Kuehr. X-ray observations of flat spectrum radio sources with the HEAO-A, Einstein and EXOSAT observatories. A&AS, 96:339–349, December 1992.

[CCC02] M. Chiaberge, A. Capetti, and A. Celotti. Optical synchrotron emission from the nuclei of FR I radio galaxies. New Astronomy Review, 46:339–341, May 2002.

[CFGM97] A. Comastri, G. Fossati, G. Ghisellini, and S. Molendi. On the Soft X-Ray Spectra of gamma -loud Blazars. ApJ, 480:534–+, May 1997.

[CLC+02] A. S. Cohen, W. M. Lane, W. D. Cotton, R. A. Perley, N. E. Kassim, T. J. W. Lazio, J. J. Condon, and W. C. Erickson. The 4-meter All-Sky Survey (4MASS): Initial Results. In Bulletin of the American Astronomical Society, pages 1274–+, December 2002.

[Col06] W. Collmar. New Blazar Detections at MeV Energies by COMPTEL. In H. R. Miller, K. Marshall, J. R. Webb, and M. F. Aller, editors, ASP Conf. Ser. 350: Blazar Variability Workshop II: Entering the GLAST Era, pages 120–+, July 2006.

[CR79] K. Chang and S. Refsdal. Flux variations of QSO 0957+561 A, B and image splitting by stars near the light path. Nature, 282:561–564, December 1979.

[CRH+03] M. H. Cohen, M. A. Russo, D. C. Homan, K. I. Kellermann, M. L. Lister, R. C. Vermeulen, E. Ros, and J. A. Zensus. Variability and Velocity of Superluminal Sources. In ASP Conf. Ser. 300: Radio Astronomy at the Fringe, page 177, 2003.

[Cru91] A. R. Crusius-Waetzel. High radiation brightness temperatures in active galactic nuclei. A&A, 251:L5, November 1991.

[DBB+96] J. N. Douglas, F. N. Bash, F. A. Bozyan, G. W. Torrence, and C. Wolfe. The Texas Survey of Radio Sources Covering -35.5 degrees declination 71.5 degrees at 365 MHz. AJ, 111:1945–+, May 1996.

[EFK+72] E. E. Epstein, W. G. Fogarty, K. R. Kackney, R. L. Hackney, R. J. Leacock, R. B. Pomphrey, R. L. Scott, A. G. Smith, R. W. Hawkins, R. C. Roeder, B. L. Gary, M. V. Penston, K. P. Tritton, C. Bertaud, M. P. Véron, G. Wlérick, A. Bernard, J. H. Bigay, P. Merlin, A. Durand, G. Sause, E. E. Becklin, G. Neugebauer, and C. G. Wynn-Williams. 3C 120, BL Lacertae, and OJ 287: Coordinated Optical, Infrared, and Radio Observations of Intraday Variability. ApJ, 178:L51+, December 1972.

[EPW+82] A. Eckart, I. I. K. Pauliny-Toth, A. Witzel, P. Hill, K. J. Johnston, and J. H. Spencer. VLBI observations of 12 compact radio sources north of declination 70 deg. A&A, 108:157–160, April 1982.

[FMC+98] G. Fossati, L. Maraschi, A. Celotti, A. Comastri, and G. Ghisellini. A unifying view of the spectral energy distributions of blazars. MNRAS, 299:433–448, September 1998.

[GBW04] Gopal-Krishna, P. L. Biermann, and P. J. Wiita. Brightness Suppression of Relativistic Radio Jets of Quasars: The Role of the Lower Electron Energy Cutoff. ApJ, 603:L9–L12, March 2004.

[GKM01] M. Georganopoulos, J. G. Kirk, and A. Mastichiadis. The Beaming Pattern and Spectrum of Radiation from Inverse Compton Scattering in Blazars. ApJ, 561:111–117, November 2001.

[GMC+99] P. Giommi, E. Massaro, L. Chiappetti, E. C. Ferrara, G. Ghisellini, M. Jang, M. Maesano, H. R. Miller, F. Montagni, R. Nesci, P. Padovani, E. Perlman, C. M. Raiteri, S. Sclavi, G. Tagliaferri, G. Tosti, and M. Villata. Synchrotron and inverse Compton variability in the BL Lacertae object S5 0716+714. A&A, 351:59–64, November 1999.

[Gou79]   R. J. Gould. Compton and synchrotron processes in spherically-symmetric non-thermal sources. A&A, 76:306–311, July 1979.

[GS65]   V. L. Ginzburg and S. I. Syrovatskii. Cosmic Magnetobremsstrahlung (synchrotron Radiation). ARA&A, 3:297–+, 1965.

[GSH⁺94] W. K. Gear, J. A. Stevens, D. H. Hughes, S. J. Litchfield, E. I. Robson, H. Terasranta, E. Valtaoja, H. Steppe, M. F. Aller, and H. D. Aller. A Comparison of the Radio / Submillimetre Spectra of Bl-Lacertae Objects and Flat Spectrum Radio Quasars. MNRAS, 267:167–+, March 1994.

[GSS⁺06] M. Guainazzi, A. Siemiginowska, C. Stanghellini, P. Grandi, E. Piconcelli, and C. Azubike Ugwoke. A hard X-ray view of giga-hertz peaked spectrum radio galaxies. A&A, 446:87–96, January 2006.

[GVR⁺97] G. Ghisellini, M. Villata, C. M. Raiteri, S. Bosio, G. de Francesco, G. Latini, M. Maesano, E. Massaro, F. Montagni, R. Nesci, G. Tosti, M. Fiorucci, E. Pian, L. Maraschi, A. Treves, A. Comastri, and M. Mignoli. Optical-IUE observations of the gamma-ray loud BL Lacertae object S5 0716+714: data and interpretation. A&A, 327:61–71, November 1997.

[HBB⁺99] R. C. Hartman, D. L. Bertsch, S. D. Bloom, A. W. Chen, P. Deines-Jones, J. A. Esposito, C. E. Fichtel, D. P. Friedlander, S. D. Hunter, L. M. McDonald, P. Sreekumar, D. J. Thompson, B. B. Jones, Y. C. Lin, P. F. Michelson, P. L. Nolan, W. F. Tompkins, G. Kanbach, H. A. Mayer-Hasselwander, A. Mücke, M. Pohl, O. Reimer, D. A. Kniffen, E. J. Schneid, C. von Montigny, R. Mukherjee, and B. L. Dingus. The Third EGRET Catalog of High-Energy Gamma-Ray Sources. ApJS, 123:79–202, July 1999.

[HBS66]   F. Hoyle, G. R. Burbidge, and W. L. W. Sargent. On the Nature of Quasi-Stellar Sources. Nature, 209:751–+, February 1966.

[HLE⁺06] V. A. Hagen-Thorn, V. M. Larionov, N. V. Efimova, E. I. Hagen-Thorn, A. A. Arkharov, A. di Paola, M. Dolci, L. O. Takalo, A. Sillanpää, and L. Ostorero. Optical and IR monitoring of the BL Lac object S5 0716+714 from 2001 2004. Astronomy Reports, 50:458–467, June 2006.

[HMWB91] S. E. G. Hales, C. J. Mayer, P. J. Warner, and J. E. Baldwin. The 6C survey of radio sources. IV - The zone delta from 67 to 82 deg, alpha from 0 to 24 H. MNRAS, 251:46–53, July 1991.

[HW96]   J. Heidt and S. J. Wagner. Statistics of optical intraday variability in a complete sample of radio-selected BL Lacertae objects. A&A, 305:42–+, January 1996.

[HWRW95] S. E. G. Hales, E. M. Waldram, N. Rees, and P. J. Warner. A revised machine-readable source list for the Rees 38-MHz survey. MNRAS, 274:447–451, May 1995.

[Jac75] J. D. Jackson. <u>Classical electrodynamics</u>. 92/12/31, New York: Wiley, 1975, 2nd ed., 1975.

[JB73] T. W. Jones and G. R. Burbidge. On the Problem of Explaining Decimeter Flux Variations in 3c 454.3 and Other Extragalactic Sources. <u>ApJ</u>, 186:791–800, December 1973.

[JJB$^+$03] D. L. Jauncey, H. M. Johnston, H. E. Bignall, J. E. J. Lovell, L. Kedziora-Chudczer, A. K. Tzioumis, and J.-P. Macquart. Interstellar Scintillation and Annual Cycles in the BL Lac Source PKS 1519-273. <u>Ap&SS</u>, 288:63–68, March 2003.

[JO77] T. W. Jones and S. L. Odell. Physical conditions in polarized compact radio sources. <u>A&A</u>, 61:291–293, October 1977.

[Kar62] N. S. Kardashev. Nonstationarity of Spectra of Young Sources of Nonthermal Radio Emission. <u>Soviet Astronomy</u>, 6:317–+, December 1962.

[Kar00] N. S. Kardashev. Radio Synchrotron Emission by Protons and Electrons in Pulsars and the Nuclei of Quasars. <u>Astronomy Reports</u>, 44:719–724, November 2000.

[KJW$^+$97] L. Kedziora-Chudczer, D. L. Jauncey, M. H. Wieringa, M. A. Walker, G. D. Nicolson, J. E. Reynolds, and A. K. Tzioumis. PKS 0405-385: The Smallest Radio Quasar? <u>ApJ</u>, 490:L9+, November 1997.

[KJW$^+$01] L. L. Kedziora-Chudczer, D. L. Jauncey, M. H. Wieringa, A. K. Tzioumis, and J. E. Reynolds. The ATCA intraday variability survey of extragalactic radio sources. <u>MNRAS</u>, 325:1411–1430, August 2001.

[KKW$^+$03] A. Kraus, T. P. Krichbaum, R. Wegner, A. Witzel, G. Cimò, A. Quirrenbach, S. Britzen, L. Fuhrmann, A. P. Lobanov, C. E. Naundorf, K. Otterbein, B. Peng, M. Risse, E. Ros, and J. A. Zensus. Intraday variability in compact extragalactic radio sources. II. Observations with the Effelsberg 100 m radio telescope. <u>A&A</u>, 401:161–172, April 2003.

[KP69] K. I. Kellermann and I. I. K. Pauliny-Toth. The Spectra of Opaque Radio Sources. <u>ApJ</u>, 155:L71, February 1969.

[Kra04] H. Krawczynski. TeV blazars - observations and models. <u>New Astronomy Review</u>, 48:367–373, April 2004.

[KS90] H. Kuehr and G. D. Schmidt. Complete samples of radio-selected BL Lac objects. <u>AJ</u>, 99:1–6, January 1990.

[KT06] J. G. Kirk and O. Tsang. High brightness temperatures and circular polarisation in extra-galactic radio sources. <u>A&A</u>, 447:L13–L16, February 2006.

[KTM$^+$98] H. Kubo, T. Takahashi, G. Madejski, M. Tashiro, F. Makino, S. Inoue, and F. Takahara. ASCA Observations of Blazars and Multiband Analysis. <u>ApJ</u>, 504:693–+, September 1998.

[KWG+93] T. P. Krichbaum, A. Witzel, D. A. Graham, K. J. Standke, R. Schwartz, O. Lochner, C. J. Schalinski, A. Greve, H. Steppe, W. Brunswig, G. Butin, H. Hein, S. Navarro, J. Penalver, M. Grewing, R. S. Booth, F. Colomer, and B. O. Ronnang. First 43-GHZ VLBI Observations with the 30-METER Radio Telescope at Pico-Veleta. A&A, 275:375–+, August 1993.

[KWPN81] H. Kuehr, A. Witzel, I. I. K. Pauliny-Toth, and U. Nauber. A catalogue of extragalactic radio sources having flux densities greater than 1 Jy at 5 GHz. A&AS, 45:367–430, September 1981.

[LJB+03] J. E. J. Lovell, D. L. Jauncey, H. E. Bignall, L. Kedziora-Chudczer, J.-P. Macquart, B. J. Rickett, and A. K. Tzioumis. First Results from MA-SIV: The Microarcsecond Scintillation-induced Variability Survey. AJ, 126:1699–1706, October 2003.

[Lon92] M. S. Longair. High energy astrophysics. Vol.1,2: Particles, photons and their detection. Cambridge: Cambridge University Press, 1992, 2nd ed., 1992.

[LP92] H. Lesch and M. Pohl. A Possible Explanation for Intraday Variability in Active Galactic Nuclei - Magnetic Reconnection and Coherent Plasma Emission. A&A, 254:29–+, February 1992.

[LRL+85] C. R. Lawrence, A. C. S. Readhead, R. P. Linfield, D. G. Payne, R. A. Preston, R. T. Schilizzi, R. W. Porcas, R. S. Booth, and B. F. Burke. Strong source VLBI observations at 22 GHz. ApJ, 296:458–460, September 1985.

[LW68] M. P. C. Legg and K. C. Westfold. Elliptic Polarization of Synchrotron Radiation. ApJ, 154:499–+, November 1968.

[LZ87] A. P. Lightman and A. A. Zdziarski. Pair production and Compton scattering in compact sources and comparison to observations of active galactic nuclei. ApJ, 319:643–661, August 1987.

[Mac03] J.-P. Macquart. Circular polarization in relativistic jets. New Astronomy Review, 47:609–612, October 2003.

[Mar80] A. Marscher. Flat-Spectrum Radio Sources - Victim of a Conspiracy - VLBI Observations. Nature, 288:12–+, 1980.

[Md05] J.-P. Macquart and G. de Bruyn. Diffractive Interstellar Scintillation of the Quasar J1819+3845 at 21cm. ArXiv Astrophysics e-prints, October 2005.

[Mel80] D. B. Melrose. Plasma astrophysics: Nonthermal processes in diffuse magnetized plasmas. Vol. New York, Gordon and Breach Science Publishers, 1980. 276 p., 1980.

[Mel94] D. B. Melrose. Low Frequency Variability of Extragalactic Radio Sources. In G. V. Bicknell, M. A. Dopita, and P. J. Quinn, editors, The Physics of Active Galaxies, volume 54 of Astronomical Society of the Pacific Conference Series, pages 91–+, 1994.

[Mel02] D. B. Melrose. Coherent Emission in AGN: A Critique. <u>Publications of the Astronomical Society of Australia</u>, 19:34–38, 2002.

[MJJ⁺95] K. McNaron-Brown, W. N. Johnson, G. V. Jung, R. L. Kinzer, J. D. Kurfess, M. S. Strickman, C. D. Dermer, D. A. Grabelsky, W. R. Purcell, M. P. Ulmer, M. Kafatos, P. A. Becker, R. Staubert, and M. Maisack. OSSE Observations of Blazars. <u>ApJ</u>, 451:575–+, October 1995.

[MK95] A. Mastichiadis and J. G. Kirk. Self-consistent particle acceleration in active galactic nuclei. <u>A&A</u>, 295:613–+, March 1995.

[MKC⁺90] M. Moshir, G. Kopan, T. Conrow, H. McCallon, P. Hacking, D. Gregorich, G. Rohrbach, M. Melnyk, W. Rice, L. Fullmer, J. White, and T. Chester. The IRAS Faint Source Catalog, Version 2. In <u>Bulletin of the American Astronomical Society</u>, pages 1325–+, September 1990.

[MKRJ00] J.-P. Macquart, L. Kedziora-Chudczer, D. P. Rayner, and D. L. Jauncey. Strong, Variable Circular Polarization in PKS 1519-273. <u>ApJ</u>, 538:623–627, August 2000.

[Oke67] J. B. Oke. Spectrophotometric Observations of Rapid Variability in 3c 279 and 3c 446. <u>ApJ</u>, 147:901–+, March 1967.

[OV90] J. P. Ostriker and M. Vietri. Are some BL Lacs artefacts of gravitational lensing? <u>Nature</u>, 344:45–47, March 1990.

[OWG⁺06] L. Ostorero, S. J. Wagner, J. Gracia, E. Ferrero, T. P. Krichbaum, S. Britzen, A. Witzel, K. Nilsson, M. Villata, U. Bach, D. Barnaby, S. Bernhart, M. T. Carini, C. W. Chen, W. P. Chen, S. Ciprini, S. Crapanzano, V. Doroshenko, N. V. Efimova, D. Emmanoulopoulos, L. Fuhrmann, K. Gabanyi, A. Giltinan, V. Hagen-Thorn, M. Hauser, J. Heidt, A. S. Hojaev, T. Hovatta, F. Hroch, M. Ibrahimov, V. Impellizzeri, R. Z. Ivanidze, D. Kachel, A. Kraus, O. Kurtanidze, A. Lähteenmäki, L. Lanteri, V. M. Larionov, Z. Y. Lin, E. Lindfors, F. Munz, M. G. Nikolashvili, G. Nucciarelli, A. O'Connor, J. Ohlert, M. Pasanen, C. Pullen, C. M. Raiteri, T. A. Rector, R. Robb, L. A. Sigua, A. Sillanpää, L. Sixtova, N. Smith, P. Strub, S. Takahashi, L. O. Takalo, C. Tapken, J. Tartar, M. Tornikoski, G. Tosti, M. Tröller, R. Walters, B. A. Wilking, W. Wills, I. Agudo, H. D. Aller, M. F. Aller, E. Angelakis, J. Klare, E. Körding, R. G. Strom, H. Teräsranta, H. Ungerechts, and B. Vila-Vilaró. Testing the inverse-Compton catastrophe scenario in the intra-day variable blazar objectS5 0716+71/object. <u>A&A</u>, 451:797–807, June 2006.

[PCG⁺04] P. Padovani, L. Costamante, P. Giommi, G. Ghisellini, A. Celotti, and A. Wolter. BeppoSAX observations of 1-Jy BL Lacertae objects - II. <u>MNRAS</u>, 347:1282–1293, February 2004.

[Per82] R. A. Perley. The positions, structures, and polarizations of 404 compact radio sources. <u>AJ</u>, 87:859–880, June 1982.

[PFB⁺05] E. Pian, L. Foschini, V. Beckmann, A. Sillanpää, S. Soldi, G. Tagliaferri, L. Takalo, P. Barr, G. Ghisellini, G. Malaguti, L. Maraschi, G. G. C. Palumbo, A. Treves, T. J.-L. Courvoisier, G. Di Cocco, N. Gehrels, P. Giommi, R. Hudec, E. Lindfors, A. Marcowith, K. Nilsson, M. Pasanen, T. Pursimo, C. M. Raiteri, T. Savolainen, M. Sikora, M. Tornikoski, G. Tosti, M. Türler, E. Valtaoja, M. Villata, and R. Walter. INTEGRAL observations of the field of the BL Lacertae object S5 0716+714. A&A, 429:427–431, January 2005.

[PFJ82] R. A. Perley, E. B. Fomalont, and K. J. Johnston. The extended radio structure of compact extragalactic sources. ApJ, 255:L93–L97, April 1982.

[Pro02] R. J. Protheroe. Factors Determining Variability Time in Active Galactic Nucleus Jets. Publications of the Astronomical Society of Australia, 19:486–498, 2002.

[Pro03] R. J. Protheroe. The brightness temperature problem in extreme intra-day variable quasars: a model for PKS 0405-385. MNRAS, 341:230–238, May 2003.

[PS74] A. G. Pacholczyk and T. L. Swihart. Polarization of radio sources. V - Absorption effects on circular repolarization in compact sources. ApJ, 192:591–595, September 1974.

[PT93] E. Pian and A. Treves. The Ultraviolet Continua of Blazars: A Reconsideration of IUE Archives. ApJ, 416:130–+, October 1993.

[QWW⁺91] A. Quirrenbach, A. Witzel, S. Wagner, F. Sanchez-Pons, T. P. Krichbaum, R. Wegner, K. Anton, U. Erkens, M. Haehnelt, J. A. Zensus, and K. J. Johnston. Correlated radio and optical variability in the BL Lacertae object 0716 + 714. ApJ, 372:L71–L74, May 1991.

[Rea94] A. C. S. Readhead. Equipartition brightness temperature and the inverse Compton catastrophe. ApJ, 426:51–59, May 1994.

[Ree66] M. J. Rees. Appearance of Relativistically Expanding Radio Sources. Nature, 211:468–+, 1966.

[Ree67] M. J. Rees. Studies in radio source structure-I. A relativistically expanding model for variable quasi-stellar radio sources. MNRAS, 135:345–+, 1967.

[Ric90] B. J. Rickett. Radio propagation through the turbulent interstellar plasma. ARA&A, 28:561–605, 1990.

[RKJ02] B. J. Rickett, L. Kedziora-Chudczer, and D. L. Jauncey. Interstellar Scintillation of the Polarized Flux Density in Quasar PKS 0405-385. ApJ, 581:103–126, December 2002.

[RL79] G. B. Rybicki and A. P. Lightman. Radiative processes in astrophysics. New York, Wiley-Interscience, 1979. 393 p., 1979.

[RLG06] B. J. Rickett, T. J. W. Lazio, and F. D. Ghigo. Interstellar Scintillation Observations of 146 Extragalactic Radio Sources. ApJS, 165:439–460, August 2006.

[RTd$^+$97] R. B. Rengelink, Y. Tang, A. G. de Bruyn, G. K. Miley, M. N. Bremer, H. J. A. Roettgering, and M. A. R. Bremer. The Westerbork Northern Sky Survey (WENSS), I. A 570 square degree Mini-Survey around the North Ecliptic Pole. A&AS, 124:259–280, August 1997.

[RVT$^+$03] C. M. Raiteri, M. Villata, G. Tosti, R. Nesci, E. Massaro, M. F. Aller, H. D. Aller, H. Teräsranta, O. M. Kurtanidze, M. G. Nikolashvili, M. A. Ibrahimov, I. E. Papadakis, T. P. Krichbaum, A. Kraus, A. Witzel, H. Ungerechts, U. Lisenfeld, U. Bach, G. Cimò, S. Ciprini, L. Fuhrmann, G. N. Kimeridze, L. Lanteri, M. Maesano, F. Montagni, G. Nucciarelli, and L. Ostorero. Optical and radio behaviour of the BL Lacertae object ¡ASTROBJ¿0716+714¡/ASTROBJ¿. A&A, 402:151–169, April 2003.

[RWR99] J. M. W. Riley, E. M. Waldram, and J. M. Riley. The 7C survey of radio sources at 151 MHz: 33 regions in the range 7h RA 17h, 30 deg Dec. 58 deg. MNRAS, 306:31–34, June 1999.

[Saz69a] V. N. Sazonov. Generation and Transfer of Polarized Synchrotron Radiation. Soviet Astronomy, 13:396–+, December 1969.

[Saz69b] V. N. Sazonov. Polarisation of Normal Waves and Synchrotron Radiation Transfer in a Relativistic Plasma. Soviet Physics JETP, 13:578, September 1969.

[SCU00] R. M. Sambruna, L. L. Chou, and C. M. Urry. Testing the Blazar Paradigm: ASCA Observations of Flat-Spectrum Radio Quasars with Steep Soft X-Ray Spectra. ApJ, 533:650–657, April 2000.

[SG85] K. A. Singal and Gopal-Krishna. Ultra-relativistic bulk motion and radio flux variability of active galactic nuclei. MNRAS, 215:383–393, August 1985.

[SK94] M. W. Sincell and J. H. Krolik. Relativistic induced Compton scattering in synchrotron self-absorbed sources. ApJ, 430:550–567, August 1994.

[Sly92] V. I. Slysh. The synchro-Compton limit of the brightness temperature of nonstationary radio sources. ApJ, 391:453–455, June 1992.

[SSN$^+$87] D. J. Saikia, C. J. Salter, S. G. Neff, A. C. Gower, R. P. Sinha, and G. Swarup. Radio observations of a few selected blazars. MNRAS, 228:203–216, September 1987.

[Syu71] R. A. Syunyaev. Induced Compton Scattering by Thermal Electrons and the Low-Frequency Spectrum of Radio Sources. Soviet Astronomy, 15:190–+, October 1971.

[TK06]   O. Tsang and J. G. Kirk.   The inverse Compton catastrophe and high brightness temperature radio sources. ArXiv Astrophysics e-prints, November 2006.

[TK07]   O. Tsang and J. G. Kirk.   The inverse Compton catastrophe and high brightness temperature radio sources. A&A, 463:145–152, February 2007.

[TMG$^+$02]   F. Tavecchio, L. Maraschi, G. Ghisellini, A. Celotti, L. Chiappetti, A. Comastri, G. Fossati, P. Grandi, E. Pian, G. Tagliaferri, A. Treves, and R. Sambruna.   Spectral Energy Distributions of Flat-Spectrum Radio Quasars Observed with BeppoSAX. ApJ, 575:137–144, August 2002.

[TRG$^+$03]   G. Tagliaferri, M. Ravasio, G. Ghisellini, P. Giommi, E. Massaro, R. Nesci, G. Tosti, M. F. Aller, H. D. Aller, A. Celotti, L. Maraschi, F. Tavecchio, and A. Wolter. The BL Lacertae objects OQ 530 and S5 0716+714. Simultaneous observations in the X-rays, radio, optical and TeV bands. A&A, 400:477–486, March 2003.

[UP95]   C. M. Urry and P. Padovani.   Unified Schemes for Radio-Loud Active Galactic Nuclei. PASP, 107:803–+, September 1995.

[Wag01]   S. J. Wagner.   Multi-Frequency Studies of Intrinsic Intraday Variability. Ap&SS, 278:105–111, 2001.

[War77]   J. F. C. Wardle.   Upper limits on the Faraday rotation in variable radio sources. Nature, 269:563–566, October 1977.

[WJS$^+$81]   E. Waltman, K. J. Johnston, J. H. Spencer, I. Pauliny-Toth, J. Schraml, and A. Witzel. Compact radio sources at declinations greater than 67 deg. A&A, 101:49–51, August 1981.

[WW95]   S. J. Wagner and A. Witzel. Intraday Variability In Quasars and BL Lac Objects. ARA&A, 33:163–198, 1995.

[WWH$^+$96]   S. J. Wagner, A. Witzel, J. Heidt, T. P. Krichbaum, S. J. Qian, A. Quirrenbach, R. Wegner, H. Aller, M. Aller, K. Anton, I. Appenzeller, A. Eckart, A. Kraus, C. Naundorf, R. Kneer, W. Steffen, and A. Zensusj. Rapid Variability in S5 0716+714 Across the Electromagnetic Spectrum. AJ, 111:2187–+, June 1996.

[ZZC$^+$97]   X. Zhang, Y. Zheng, H. Chen, S. Wang, A. Cao, B. Peng, and R. Nan. The Miyun 232 MHz survey. A&AS, 121:59–63, January 1997.